Investigation of the Stimulated Brillouin Scattering (SBS) Gain Enhancement in Silicon Nano-Waveguides and Applications

Von der Fakultät für Elektrotechnik, Informationstechnik, Physik
der Technischen Universität Carolo-Wilhelmina zu Braunschweig

zur Erlangung des Grades eines Doktors
der Ingenieurwissenschaften (Dr.-Ing.)

genehmigte Dissertation

von Hassanain Majeed Al-Taiy

(Irak, Bagdad, University of Information Technology and Communications)

aus Irak, Bagdad

eingereicht am: 06.10.2016

mündliche Prüfung am: 17.01.2017

1. Referent: Prof. Dr. rer. nat. Thomas Schneider
2. Referent: Jun.-Prof. Dr. Kambiz Jamshidi

Druckjahr: 2017

This work was carried out under the supervision of Prof. Dr. rer. nat. Thomas Schneider, Faculty of Elektrotechnik Engineering, Technischen Universität Carolo-Wilhelmina zu Braunschweig

Acknowledgment

First of all I want thank my God for saving me and offering me the chance to study in Germany. Great thanks go to my parents in Baghdad for their praying and encouragement. Special thanks go to my family, Shaima'a, Mohammed, Faris and Nora for their support, understanding and encouragement.

Deeply heart thanks go to my supervisor Prof. Thomas Schneider for his continuous support and encouragement. I am grateful to Mr. Stefan Preußler for his support through the practical and the writing parts of the study.

Great thanks for Mr. Kambiz Jamshidi for helping me during the organization of Ph.D. letter of acceptance with the supervisor and traveling process from Baghdad to Leipzig.

Special thanks to Mr. Jens Klinger and Norman Wenzel from the Hochschule für Telekommunikation Leipzig for their support.

I want to acknowledge the Iraqi government: University of Information Technology and Communications for their financial support and encouragement.

Thanks for Mr. Kevin Leavey for reading my thesis and giving his comments and suggestions.

Last but not least I want to present this work to the soul of my sister Suad Majeed Al-Taiy for her previous support and encouragement during my B.Sc. and M.Sc. in Baghdad.

Contents

List of Figures

Glossary

BSBS backward stimulated Brillouin scattering

BV bias voltage

C circulator

Cb conductive band

Comp computer software

DFB distributed feedback laser

DS dip search

EDFA Erbium doped fiber amplifier

EFS Eigen frequency study

ES electrostriction

ESA electrical spectrum analyzer

EWM elastic wave module

FBG fiber Bragg gratings

FC frequency counter

FCA free carrier absorption

FCI free carrier index

FP floquet periodicity

FPGA field programmable gate array

FSBS forward stimulated Brillouin scattering

FWM four wave mixing

IM intensity modulator

LUT laser under test

MLFL mode-locked fiber laser

MLL mode locked laser

mm-wave millimeter wave

MST Maxwells stress tensor

OSA optical spectrum analyzer

PBS polarization beam sipliter

PC polarization controller

PD photo diode

PLL phase locked loop

PN phase noise

PPA-SBS polarization pulling assisted stimulated Brillouin scattering

Q quality factor

QLS quasi light storage

RF radio frequency

RFG radio frequency generator

RP radiation pressure

SBS stimulated Brillouin scattering

SOI silicon on insulator

SOP state of polarization

SOS silicon on sapphire

SPM self phase modulation

SSMF standard single mode fiber

TOF tuneable optical filter

TPA two-photon absorption

URS ultrahigh-resolution spectroscopy

Vb valence band

VCO voltage controled oscillator

WDM wavelength-division multiplexing

WS wave shaper

XPM cross phase modulation

Abstract

Stimulated Brillouin scattering is a third order non-linear effect with the lowest power threshold in standard single mode optical fiber, by which an interaction between optical and acoustic modes takes place. During the Brillouin scattering process, part of the pump wave power will be transferred to a counter propagating wave (Stokes), with a frequency shift of about 11 GHz for a telecommunication wavelength of 1550 nm in a standard single mode fiber. The frequency shift effective parameters had been studied as well as the governed equations for the pump and Stokes waves had been given. The Brillouin scattering gain linewidth for a standard single mode fiber was about 35 MHz. Therefore, and due to the increasing demands for ultra-high resolution spectroscopy, integrated photonics and other interesting applications, the effect and utilization of the stimulated Brillouin scattering were studied. It's effect in silicon-on-insulator waveguides was investigated as well.

The effect of stimulated Brillouin scattering in silicon-on-insulator was studied in strip and rip-waveguides, each with two cases: air and silica cladding. The gain coefficient was simulated for each kind and case. It is found that the rib air cladding waveguide has the highest non-linearity with a gain coefficient of 1.32×10^4 $(\mathrm{m}*\mathrm{W})^{-1}$ which is in the order of magnitudes higher than in optical fibers ($2e^{-11}$ m/W). Therefore, an SOI-waveguide with a length of 100 μm corresponds to a 1 km optical fiber.

Furthermore, the stimulated Brillouin scattering was utilized as a narrow band optical filter and amplifier in standard single mode fibers for various applications. First, stimulated Brillouin scattering assisted with polarization pulling was utilized to extract one high quality, narrow linewidth and tunable spectral line out of a frequency comb generated by a mode locked fiber laser. This spectral line had a linewidth of 1 kHz and acted as tunable laser source. The laser was stabilized by measuring the temperature dependent repetition rate drift of the mode locked fiber laser and a subsequent modulation. A residual drift for the extracted spectral line of $\pm$ 160 mHz was achieved. Second, two spectral lines were extracted out of the frequency comb by the same manner and mixed in a photo diode to generate a high quality milli-meter wave. It was stabilized via two methods: software and analog circuit. The RF signal showed a linewidth $<$ 1 Hz and a phase noise of -134 dBc/Hz at 10 kHz frequency offset and a stability of 50 Hz in about 40 minutes duration time for the software approach. For the analog circuit approach a phase noise of -58 dBc/Hz at 10 kHz and a stability of 1 Hz over 40 minutes could be achieved.

Kurzfassung

Die stimulierte Brillouin-Streuung, ein nichtlinearer Effekt der dritten Ordnung, besitzt den niedrigsten Schwellwert in optischen Fasern und beruht auf der Wechselwirkung zwischen optischen und akustischen Wellen. Während des Streuprozesses wird ein Teil der Energie der Pumpwelle auf eine sich gegenläufig ausbreitende Stokeswelle übertragen, wobei der Frequenzversatz in Standard-Einmodenfasern bei einer Pumpwellenlänge von 1550 nm ungefähr 11 GHz beträgt. Die Parameter hinsichtlich der Frequenzverschiebung als auch die Gleichungssysteme für die Pump- und Stokeswelle wurden betrachtet. Die Linienbreite der stimulierten Brillouin Streuung in einer Standard-Einmodenfaser beträgt etwa 35 MHz. Deshalb und aufgrund der zunehmenden Anforderungen für ultrahochauflösende Spektroskopie, integrierte Photonik und andere interessante Anwendungen, wurde der Effekt und die Verwendung der stimulierten Brillouin Streuung untersucht. Zusätzlich wurde der Effekt der stimulierten Brillouin Streuung auch in silicon-on-insulator Wellenleitern untersucht.
Dabei wurden speziell Streifenwellenleiter und rip-waveguides untersucht und dabei das Mantelmaterial variiert. Der Verstärkungskoeffizient wurde für jede Art und geden Fall simuliert. Dabei ergaben sich die höchsten Nichtlinearitäten für den rip-waveguide mit einem Verstärkungskoeffizienten von 1.32×10^4 $(\mathrm{m}*\mathrm{W})^{-1}$, welcher im Vergleich zu Standard-Einmodenfasern ($2e^{-11}$ m/W) um Größenordnungen höher ist. Daher entspricht die Nicht-Linearität in einem 100 μm SOI-waveguide der von 1 km Faser.
Weiterhin wurde die stimulierte Brillouin Streuung als schmalbandiger optischer Filter und Verstärker in Standard-Einmodenfasern für verschiedene Anwendungen eingesetzt. Zuerst wurde die polarisationsabhängige Verstärkung der Brillouin Streuung für die Extraktion einer einzelnen, schmalen und durchstimmbaren Mode aus einem Frequenzkamm, erzeugt von einem modengekoppelten Faserlaser, verwendet. Die Linienbreite dieser Mode ergab sich zu 1 kHz und wurde als durchstimmbarer Laser genutzt. Der Laser wurde durch eine Messung der temperaturabhängigen Drift der Wiederholrate und anschließender Modulation der extrahierten Mode stabilisiert. Dabei wurde ein Restdrift des Lasers von $\pm$ 160 mHz erreicht. Zweitens wurden auf die gleiche Weise zwei Spektrallinien aus dem Frequenzkamm extrahiert und in einer Fotodiode gemischt. Dies ermöglichte die Erzeugung von qualitativ hochwertigen Millimeterwellen, welche anhand von zwei unterschiedlichen Methoden stabilisiert wurden. Die erste Methode erfolgte durch eine Software wodurch das Hochfrequenzsignal eine Linienbreite <1 Hz, ein Phasenrauschen von -134 dBc/Hz bei einem Frequenzoffset von 10 kHz und einer Stabilität von 50 Hz für eine Dauer von 40 Minuten hatte. Für die zweite Methode zur

Stabilisierung wurde eine analoge Schaltung verwendet, womit ein Phasenrauschen von -58 dBc/Hz bei 10 kHz Offset und eine Stabilität von 1 Hz über 40 Minuten erreicht werden konnten.

Chapter 1

Introduction

1.1 Overview and Motivation

In general, light scattering can be defined as the deviation of a part of the incident light into any possible direction. In principle, when the light particles, i.e. photons (quanta of the electromagnetic field) are forced to deviate from their straight trajectory into one or more paths via an obstacle or non-homogeneity i.e. scattering particles of the transfer medium, then light scattering takes place. The scattered light was first observed spectroscopically by which a beam of light irradiates at a sample like a solid, liquid or gas [1].

There are many types of light scattering like: Rayleigh, Mie, Tyndall, Raman and Brillouin scattering [1, 2, 3]. All these phenomena are caused by inhomogeneities of the optical properties in the light transfer medium, such as the variation in the refractive index, molecules or the polarization [4, 5]. For example, Rayleigh scattering is caused by the deviation of the incident light by the density variation of the molecules and particulate matter which have size much smaller than the wavelength of the incident light. Rayleigh scattering process occurs when light penetrates gaseous, liquid, or solid phases when they were liquids before such as optical fibers after glass melting of matter. In principle, no frequency shift occurs within the Rayleigh effect, since it is due to the light scattering from non-propagating arbitrary refractive index fluctuations which is caused by a random density distribution. It is called elastic scattering, since the light that is scattered by the particle is emitted at the same frequency of the incident light. Therefore, Rayleigh scattering is playing an important role in the determining of the usable optical window in the optical fibers, i.e. it is the main cause of signal loss in optical fibers [6].

The intensity of Rayleigh scattering has a very strong dependence on the size of the medium particles within the range of the wavelength, since it is proportional to the third power of their diameter. Additionally, it is inversely proportional to the fourth power of the wavelength of the incident light such as ($I_S \approx \frac{1}{\lambda^4}$). This means that the shorter wavelengths in the visible white light (blue and violet) are scattered stronger than the

longer wavelengths toward the red end of the visible spectrum. Therefore, it is responsible for the blue color of the sky during the day and the orange colors during sunrise and sunset [7].

Mie scattering is a broad type of light scattering caused by spherical particles of diameters in the order of the magnitude of the wavelength. The scattering intensity in general is not strongly dependent on the wavelength i.e. within the wavelength band all frequencies act in the same way, however it is sensitive to the particle size. The intensity of Mie scattering for large particles is proportional to the square of the particle diameter within the range of the wavelength. The appearance of the common materials like milk, latex paint, water drops or fog and biological tissue can be understood via Mie scattering, for instance. On the other hand, Tyndall scattering is just like Mie scattering without the restriction to the spherical geometry of the particles. It is particularly applicable to colloidal mixtures and suspensions like milk.

Raman scattering was first discovered by the Indian physicist Sir Chandrasekhara Raman in 1928. First he noticed the blue color of the sea (which is caused by Rayleigh scattering), and therefore he predicted the scattering origin of the sun light at the water molecules. Additionally, he found in addition to the original wavelength, that in the scattered field other frequencies with shifted wavelengths could be found, i.e higher and lower as the incident frequency. In principle, Raman scattering is inelastic light scattering, since the incident light interacts with the optical phonons (quanta of medium excitation), which are predominantly intra-molecular vibrations and rotations with energies larger than that of acoustic phonons.

Generally, Raman scattering can be spontaneous or stimulated. In the spontaneous case the interaction between the photons and phonons results from the transfer of a part of the incident light with a specific wavelength to a new wave (scattered wave) with up or down shifted wavelength. The vibrational modes of the medium are responsible for determining the wavelength shift of the scattered wave. Therefore, the Stokes and anti-Stokes frequency shifts are in the THz range. On the other hand, in the stimulated case (which was first observed in 1971 [8]) high power transformation takes place between the incident light and the scattered wave with a new frequency. Raman scattering is very useful for several applications, since it occurs regardless of the incident frequency [9]. For example, Raman spectroscopy is used for distributed temperature sensing along optical fibers. Therefore, the Raman-backscattered wave from laser pulses is utilized to determine the temperature along optical fibers.

The Scattering of light at acoustic waves was first investigated by the french physicist Léon Brillouin in the 1920s [10, 7]. Later this effect was named after him. Brillouin scattering occurs as a result of the interaction between the incident light (photons) and the vibrational quanta of lattice vibrations (acoustic phonons) in solids or with elastic waves in liquids. In other words, sound waves represent alternating regions of compressed material and expanded material. Therefore, the refractive index increases with the density of electrons and thus with compression. Hence, scattering will be induced by index

discontinuities. The main difference between Brillouin and Raman scattering is that, in Brillouin scattering the acoustic phonon is responsible for the scattering process while in Raman the optical phonon generates the scattering.

Just like Raman scattering, there are two cases of Brillouin scattering: spontaneous and stimulated. At normal light power levels (low photon density) the amount of Brillouin scattering is rather low, which is called spontaneous Brillouin Scattering. In principle, spontaneous Brillouin scattering is caused by the arbitrary traveling of acoustic waves originated from the thermal motions of the molecules in the medium [7]. On the other hand, with high intensity coherent laser light, the amount of Brillouin scattering can become enormous, and therefore the Brillouin scattered light takes the exponential growth form [11]. Hence, the acoustic phonons generated by the medium density fluctuations (which result from the intensity modulation by electrostriction) that propagates with the velocity of sound, are in turn generating a refractive index modulation. Therefore, the incident light will be scattered, which in turn increase the density modulation and so on. This phenomenon is known as stimulated Brillouin scattering (SBS).

In principle and according to the quantum mechanics explanation, during the Brillouin scattering process the incident photon will be annihilated, whereas a new photon as well as a new phonon will be created. Therefore, and with the creation or annihilation of a phonon (which will be added to the acoustic wave within the medium) during the Brillouin scattering process, a radiation i.e. scattered photons will be generated which are known as Stokes or anti-Stokes waves, respectively [12]. Hence, the Brillouin scattering process is considered to be an inelastic process, i.e. it is shifted in energy from the input pump frequency by an amount that corresponds to the energy of the elastic wave or phonon. Therefore, it occurs on the higher and lower energy side of the pump frequency, which may be associated with the creation and annihilation of a phonon [13]. The Stokes wave is downshifted from the incident wave frequency, while the anti-Stokes wave is upshifted. These frequency shifts are in the GHz range, since the relative velocity between pump and acoustic wave which is responsible for determining the frequency shift, is much smaller than the optical frequency and therefore smaller than in the Raman case. For the stimulated process, the Stokes wave requires a launching wave at a specific frequency and position within the medium. There are two generation possibilities for that launching wave: either generated from the spontaneous scattering, i.e. the noise ground of the optical medium or from a separate counter propagating wave. Additionally, the Stokes wave intensity depends on the incident light wave, the attenuation of the incident wave within the transmission medium and the Brillouin gain which refers to the medium. Like the Raman process, a part of the incident wave power will be transferred to the Stokes within the Brillouin process.

In many fields like telecommunication, determining the power of the input and output wave is very important. Therefore, the effective mode area factor is used to govern the relation between the power and intensity. In principle, within optical fibers the wave is guided in the core area, where the standard single mode fiber has an effective mode area of 80 μm^2 [14]. For a non-guiding medium SBS requires a high power, therefore

an optical fiber is used to achieve SBS. Nevertheless, the required high power could be reduced via reducing the interaction cross section area (effective mode area), increasing the interaction length (effective length) of the incident light beam or increasing the medium non-linearity [15]. Hence, the selection of the non-linear material and interaction medium is very important for SBS applications. Additionally, since the SBS; as a non-linear process, causes optical power transfer between modes in both backward and forward directions, SBS generates optical gain with a frequency shift. This optical gain is very useful for different applications, therefore a lot of attempts had been done to enhance the SBS gain and reduce the interaction optical length such as the utilization of integrated photonics devices, for instance.

In optical telecommunication applications, mainly fiber based SBS is utilized. Since SBS is particularly generated by electrostriction, kilometers of fibers are required to initiate a rather low SBS effect via electrostriction, while with the nano-scale this pattern collapses [16]. Due to the small modal area of the silicon waveguides which is about 100 times smaller than the conventional optical fibers, an increased optical intensity within the silicon waveguides could be achieved easily. Hence, it is possible to produce chip-scale Brillouin devices. In principle, the non-linearities within silicon are caused by the interaction of the incident waves optical fields (electric field) with electrons and phonons. Therefore, the incident electric field resonates with the outer shells electrons and then polarization will take place. Hence, silicon provides massiveness of non-linear optical effects mainly for Brillouin and Raman scattering, therefore it can be used to achieve and process optical signals in low-cost ultra compact chips with speeds above those of today's electronic devices [17].

It is shown that in Silicon on Insulator (SOI) waveguides in addition to the electrostriction, the radiation pressure takes place to enhance the SBS gain by several orders of magnitude [18]. Hence, a new form of SBS non-linearity can be achieved. SOI indicates to the technology by which a layered silicon-insulator-silicon is used instead of a conventional silicon substrate [19].

In principle, the SBS effect in optical fiber is attractive for a lot of applications. For example, there are many demonstrations for Brillouin-based optical fiber sensors to measure the temperature like: Brillouin optical correlation-domain analyzers, Brillouin optical time domain reflectometers and Brillouin optical time domain analyzers [20, 21, 22], respectively. In [23] for example, a method for temperature sensing utilizing SBS-based slow light (where the group velocity of the light wave within a medium is much less than the light velocity in vacuum) is presented by using 100 m single mode optical fiber and a continuous wave pump. The approach of sensing is based on the temperature dependence of the Brillouin frequency shift in the optical fiber. As consequence, the spatial resolution is realized by measuring the frequency shift in dependence of the time delay of the input pump pulse.

Additionally, optical amplifiers and filters are key elements of any long fiber optic communication system. Recently, an elegant method was reported to filter and amplify

spectral lines out of a frequency comb generated by a mode-locked fiber laser (MLFL) [24, 25]. The MLFL which has a very high precision is utilized for producing a very narrow linewidth and high quality tunable single line laser and generating a very high quality millimeter wave with a very low phase noise. The MLFL contains around 100.000 spectral lines with a repetition rate of 100 MHz. However, the conventional optical filters are not sufficient to filter one line out of that MLFL, since their bandwidths are higher than the MLFL repetition rate. Therefore, the non-linear effect of polarization pulling assisted stimulated Brillouin scattering (PPA-SBS) [26] in a 50 km long standard single mode fiber (SSMF) with a bandwidth of 10-30 MHz is utilized to select and amplify any spectral line out of the MLFL comb.

The high quality extracted spectral lines out of the MLFL have very important applications. For example, coherent detection systems require a highly stable single spectral line and therefore can be used for optical communications. In addition, wavelength-division multiplexing systems, high resolution spectroscopy as well as multilevel modulation formats require a narrow linewidth, very stable and widely wavelength-tunable single spectral line. Whereas, two extracted spectral lines out of the MLFL can be utilized to generate high quality RF signals, i.e. millimeter and sub-millimeter waves. In principle, when two optical waves are mixed at a proper photo diode an optoelectronic conversion will take place and therefore an RF signal will be generated.

1.2 Thesis Outline

This thesis investigates the effect and applications of SBS in optical fibers as well as its gain enhancement in SOI waveguides.

In chapter two, the physics and theory of SBS are presented as well as the origin of SBS scattering within optical fibers is studied and equations are driven.

Chapter three covers the SBS effect in SOI waveguides. Equations that govern the opto-mechanical forces within SOI waveguides are derived. Simulation results and practical challenges are presented. SBS gain enhancement is shown within these simulations.

The second part of the thesis is focused on the utilization of SBS for the processing of frequency combs. Chapter four investigates an important application of SBS in optical fibers: the extraction and stabilization of a single line out of a frequency comb produced by a MLFL. The generated frequency comb is utilized with the help of the polarization pulling assisted stimulated Brillouin scattering to extract a high quality spectral laser line. Several methods for measuring the extracted laser line are explained. The experimental setup and results are presented.

Chapter five deals with another important SBS application which is a high quality millimeter wave generation and stabilization. Millimeter waves generation and stabi-

lization as well as the phase noise are explained. The practical setup and results are presented. Chapter six exhibits the conclusions and proposes the outlook.

Chapter 2

Stimulated Brillouin Scattering

2.1 Introduction

As early as 1918, Leonid Mandelstam believed to have recognized the possibility of inelastic light scattering, nevertheless he published that idea in 1926 [27]. In 1922, Léon Nicolas Brillouin predicted the inelastic light scattering by thermally excited acoustic phonons [28]. Therefore, that kind of non-linear effect is named by his name: Brillouin Scattering.

In principle, the interaction between the incident light waves (photons) with the acoustic waves (phonons) is responsible for the so-called: Brillouin scattering effect. Within this effect, the incident photons will be annihilated. As a result and with the creation or annihilation of a phonon, a scattered radiation (photons) will be generated at the downshifted frequency component (Stokes) or upshifted frequency component (anti-Stokes), respectively. On the other hand, the acoustic wave inside the medium originates from the density fluctuations which travel through the medium at the velocity of sound. Additionally, optical property variations of the medium could also lead to light scattering. Normally at low intensity light level, the scattering is caused by thermal or quantum mechanical excitation. This kind of scattering is known as spontaneous scattering. Furthermore, at high light power level stronger light scattering could be achieved due to the excitation of the density fluctuations. This kind of scattering is called stimulated. For both spontaneous and stimulated light scattering, the periodic density fluctuations causes a refractive index modulation. Hence, the incident light scatters.

Among the other non-linear effects in optical fibers like: Four-Wave-Mixing, Self- and Cross-Phase Modulation, Solitons and Raman scattering, the Stimulated Brillouin scattering (SBS) has the lowest threshold power. Therefore, a relative low incident power is adequate to generate the SBS. As it will be shown later, in optical communication systems when the SBS threshold will be exceeded, all the input power will be scattered back and hence, the signal power could not be increased further. Thus, the usable input power within optical communication systems is determined by SBS. However, this can be

avoided easily by increasing the SBS threshold by using a transmitted signal with higher bandwidth than the intrinsic Brillouin gain.

This chapter is organized as follows: the derivations of Maxwell's equations are studied and the linear and non-linear effects are first explained in general and then in detail. The optical fiber linear effects are explained in detail through the derivations of the linear wave propagation and polarization effect equations within a linear optical medium. Then, the non-linear optical effects are studied and the non-linear- wave and polarization equations are derived.

The chapter is focused on the origin of the non-linear Brillouin scattering effect which is explained in detail. After that, the spontaneous and stimulated Brillouin scattering are studied. Then the theoretical description of stimulated Brillouin scattering is given. After that, Brillouin scattering factors are determined. At the end of this chapter, the pump depletion effect in stimulated Brillouin scattering is presented.

2.2 Linear and Non-Linear Optical Effects

The terms linear and non-linear effects, in optics (as illustrated in Fig. 2.1) refer to the intensity independent (black line) and the intensity-dependent (red curve) responses of the optical medium, respectively.

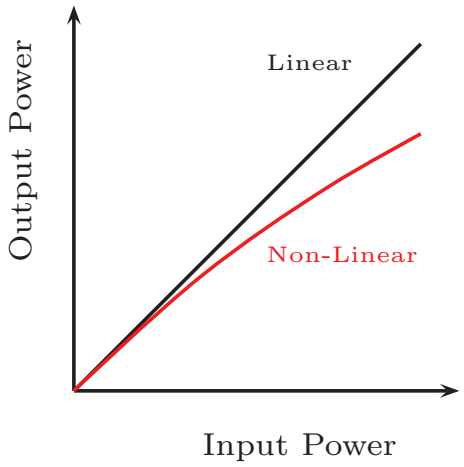

Figure 2.1: Linear and non-linear interaction effects performance [4].

In principle, when the electromagnetic field hits the optical medium particles like atoms or molecules, there will be two possible reactions:

First, if the material band gap is smaller or equal to the photons energy ($\hbar\omega$), then the photons will be absorbed via electrons of the atom, where $\hbar$ is the Planck's constant

and ω is the photon angular frequency. Therefore, the absorbed energy will be transformed into internal energy of the absorber, like thermal energy [29]. The reduction in the intensity of the light wave propagating through a medium by absorption of a part of its photons is called attenuation. Normally, the absorption of waves is intensity independent i.e. it is linear. Nevertheless, in optics the medium changes its transparency depending on the intensity of the incident waves, and hence a saturable absorption i.e. non-linear absorption takes place. On the other hand, after the absorption the excitation decay of the atom could take different forms with different energy and frequency from the original wave. The most important and dominant in optical telecommunications is the spontaneous emission [7], since within some materials it can be transferred to the region of stimulated emission by which lasers and Erbium-doped amplifiers (EDFA) based on.

Second, if the band gap of the material is larger than the photon energy, then and contrary to the first case, no excitation towards the higher atom energy level will occur. However, the absorbed photon will upset the distribution of the charges within the atom. Since, the charges depend on the incident electric field, they will be accelerated. Additionally, the emitted photons have the same energy and frequency of the original wave. Nevertheless, they have a different phase by which the linear optical effects originate from, such as diffraction, reflection, refraction, absorption and scattering. On the other hand, in mediums like optical fibers which are made from silica glass, only the excitation in the way of charge acceleration can occur because they have a much higher band gap than the photon energy.

To describe the linear effects in optical fibers, one should start from the Maxwell's equations in vacuum that describe the interaction between the electromagnetic field (optical wave) and the material (optical fiber).

The Maxwell equations can be written as [30]:

$$\nabla \times \boldsymbol{E} = -\frac{\partial \boldsymbol{B}}{\partial t} \tag{2.1a}$$

$$\nabla \times \boldsymbol{H} = \boldsymbol{j} + \frac{\partial \boldsymbol{D}}{\partial t} \tag{2.1b}$$

$$\nabla \cdot \boldsymbol{D} = \rho \tag{2.1c}$$

$$\nabla \cdot \boldsymbol{B} = 0 \tag{2.1d}$$

where ∇ is the Nabla operator, $\boldsymbol{E}$ and $\boldsymbol{H}$ are the electric and magnetic field vectors with the corresponding flux densities (inductions) $\boldsymbol{D}$ and $\boldsymbol{B}$, respectively. $\boldsymbol{j}$ is the current density and ρ is the carrier density. In Eq. 2.1a a time varying field ($-\frac{\partial \boldsymbol{B}}{\partial t}$) is the origin of the electric field eddies ($\nabla \times \boldsymbol{E}$). While, in Eq. 2.1b either the current density ($\boldsymbol{j}$) or the time dependent variation in the electric flux density ($\frac{\partial \boldsymbol{D}}{\partial t}$) is the origin of magnetic eddies. On the other hand, the existance of the sources (ρ) is the origin of the electric field as illustrated in Eq. 2.1c. Whereas, the magnetic field is free of sources as shown in Eq. 2.1d.

In vacuum, the electric flux density ($\boldsymbol{D}$) is related to the electric field vector ($\boldsymbol{E}$) by the vacuum permittivity (ε_0), i.e. ($\boldsymbol{D} = \varepsilon_0 \boldsymbol{E}$) and within identity, ($\boldsymbol{B} = \mu_0 \boldsymbol{H}$), where ($\mu_0$) is the permeability [31, 32]. Since in vacuum there are no current ($\boldsymbol{j}$) and carrier (ρ) densities, and by using the magnetic flux ($\boldsymbol{B}$) instead of ($\boldsymbol{H}$) and ($\boldsymbol{E}$) instead of ($\boldsymbol{D}$) in Eq. 2.1b then Eq. 2.1 can be rewritten as follows:

$$\nabla \times \boldsymbol{E} = -\frac{\partial \boldsymbol{B}}{\partial t} \tag{2.2a}$$

$$\nabla \times \boldsymbol{B} = \mu_0 \varepsilon_0 \frac{\partial \boldsymbol{E}}{\partial t} \tag{2.2b}$$

by substituting Eq. 2.2b into Eq. 2.2a, one can get a hyperbolic partial differential equation which is the wave equation of the electromagnetic field that propagates in vacuum and can be written as:

$$\left(c^2 \nabla^2 - \frac{\partial^2}{\partial t^2} \right) \boldsymbol{E} = 0 \tag{2.3}$$

where $c = 1/\sqrt{\varepsilon_0 \mu_0}$ is the speed of light in vacuum (299,792,458 m/s) which is identical for all waves in vacuum and (∇^2) is the spatial Laplace operator (Δ). Therefore, Eq. 2.3 can be rewritten as follows:

$$\Delta \boldsymbol{E} = \frac{1}{c^2} \frac{\partial^2 \boldsymbol{E}}{\partial t^2} \tag{2.4}$$

The medium can be classified to:

1. Simple Medium.

2. Dispersive Medium.

3. Non-linear Medium.

4. Anisotropic Medium.

5. Bi-isotropic and Bi-anisotropic Medium.

Here, it will be discussed only the simple and non-linear dispersive medium.

2.2.1 Linear Effects

When a wave travels within a certain medium, that medium affects the propagating wave and hence the wave equation itself. For example, the phenomena of conduction, polarization, and magnetization would take place. In principle, within vacuum ($\boldsymbol{P}$=

0), where ($\boldsymbol{P}$) is the (polarization vector) which is the vector sum of the electric dipole moments per unit volume, i.e. the volume density of electric dipole moment. For example, when an electric field of a condenser is applied to an insulator which placed into that condenser, then the charges of the insulator atoms will shift as an influence of the electric field force. This phenomenon is called polarization [7]. Therefore, the electric flux density will be:

$$\boldsymbol{D} = \varepsilon_r \varepsilon_0 \boldsymbol{E} \tag{2.5}$$

where ε_r is the relative permittivity which depends on the medium, polarization and the frequency of the incident wave.

The simple medium is the non-dispersive, linear and isotropic medium. Hence, within such medium the vector ($\boldsymbol{P}$) is parallel and linearly related to the external low strength electric field ($\boldsymbol{E}$). In principle, the relation between them can be written as:

$$\boldsymbol{P} = \boldsymbol{P}_L = \varepsilon_0 \chi \boldsymbol{E} \tag{2.6}$$

where $\boldsymbol{P}_L$ refers to the linear polarization and ($\chi = \varepsilon_r - 1$) is the electric susceptibility and refers to the polarizability of the medium. Therefore, Eq. 2.5 can be rewritten by using Eq. 2.6 as follows:

$$\boldsymbol{D} = \varepsilon_0 \left(1 + \chi\right) \boldsymbol{E} = \varepsilon_0 \boldsymbol{E} + \boldsymbol{P} \tag{2.7}$$

The main difference between linear and non-linear optics is that the polarization is linearly and non-linearly proportional to the electric field strength, respectively, i.e. depending on the strength of the applied electric field itself. For instance, by applying a noncoherent source like a light emitting diode, lamps or a sunlight, linear optical effects take place. Substituting Eq. 2.7 in Eq. 2.1b and by assuming the current density ($\boldsymbol{j}$=0) within the simple medium, one can get:

$$\nabla \times \boldsymbol{B} = \varepsilon_0 \mu_0 \frac{\partial \boldsymbol{E}}{\partial t} + \mu_0 \frac{\partial \boldsymbol{P}}{\partial t} \tag{2.8}$$

Thus, the wave equation for the stable, uniform simple medium will be:

$$\Delta \boldsymbol{E} = \frac{1}{c^2} \frac{\partial^2 \boldsymbol{E}}{\partial t^2} + \frac{1}{\varepsilon_0 c^2} \frac{\partial^2 \boldsymbol{P}}{\partial t^2} \tag{2.9}$$

The first term refers to the primary wave, while the second term refers to the secondary wave which originates from the polarization effect of the medium as a result of the external wave. Both waves have the same frequency but with a relative phase shift. Substituting Eq. 2.6 into Eq. 2.9 and by using Eq. 2.5, then the wave equation in a simple medium will be:

$$\Delta \boldsymbol{E} = \frac{\varepsilon_r}{c^2} \frac{\partial^2 \boldsymbol{E}}{\partial t^2} \tag{2.10}$$

In isotropic simple media, both the electric and polarization vectors are in the same direction and the susceptibilities in all directions are equal. Additionally, in isotropic media the relative permittivity is a constant scalar [31]. On the other hand, in other (non-simple) media the relative permittivity is a complex second order tensor. The solution of Eq. 2.10 will be used to describe the linear optical effects. The main difference between the wave propagation in vacuum and material is that: within material the wave will travel slower than within vacuum by a factor of $(1/n)$, where n is the real part of the complex refractive index $(\hat{n}(\omega))$ of the material and can be written as [7]:

$$\hat{n}(\omega) = n(\omega) + j\kappa(\omega) = \sqrt{\varepsilon_r(\omega)} \tag{2.11}$$

where (κ) and (ω) are the extinction coefficient and the molecule resonance frequency of the material, respectively. In principle and referring to Eq. 2.9, the phase difference between the primary and secondary waves results in a wave propagation velocity difference between vacuum and material. Therefore, the wave propagation velocity in material depends on the electromagnetic wave frequency and the material properties while this is not the case within vacuum and the wave propagates with the velocity of light.

By assuming a plane transverse monochromatic wave which depends only on one coordinate (z direction for example), then Eq. 2.10 will be:

$$\frac{\partial^2 \boldsymbol{E}}{\partial z^2} = \frac{\hat{n}^2}{c^2} \frac{\partial^2 \boldsymbol{E}}{\partial t^2} \tag{2.12}$$

here $\boldsymbol{E} = (E_x, E_y, 0)$ is perpendicular to the propagation direction z. The solution for Eq. 2.12 will be:

$$\boldsymbol{E}(z,t) = \frac{1}{2}(\hat{E}e^{j(\hat{n}k_0 z - \omega t)} + c.c)\mathbf{e}_i = \left|\hat{E}\right| cos(\hat{n}k_0 z - \omega t + \varphi_0)\mathbf{e}_i \tag{2.13}$$

where $(\hat{E} = \mathrm{Re}(\hat{E}) + \mathrm{j}\ \mathrm{Im}(\hat{E}) = a + \mathrm{j}b)$ is the complex amplitude of the wave, $(\omega = 2\pi f)$

is the angular frequency, ($k_0 = 2\pi/\lambda$) is the wave number, $\mathbf{e}_i$ is the unit vector for an arbitrary i-direction and ($\varphi_0 = \arctan\frac{a}{b}$) is the phase for z=0, therefore $\hat{E}$ can be written as:

$$\hat{E} = E_0 e^{j\varphi_0} \tag{2.14}$$

In principle, all linear optical phenomena like: scattering, reflection, refraction, absorption and diffraction can be described by Eq. 2.10 and for a particular condition (propagation in z direction) Eq. 2.13 can be used as a solution for Eq. 2.10. When Eq. 2.11 is used in Eq. 2.13, then the wave propagation within insulator can be written as:

$$\boldsymbol{E}(z,t) = \frac{1}{2}(\hat{E}e^{j((n+j\kappa)k_0 z-\omega t)} + c.c)\mathbf{e}_i = \frac{1}{2}(\hat{E}e^{-\kappa k_0 z}e^{j(nk_0 z-\omega t)} + c.c)\mathbf{e}_i \tag{2.15}$$

To understand the optical signal attenuation within optical fibers, a brief focus on Eq. 2.15 will be given. Mainly, scattering and absorption are the origin of an attenuation in optical fibers. The term ($\hat{E}e^{-\kappa k_0 z}$) for instance, refers to the wave amplitude decrease within z distance propagation. Additionally, the wave intensity is related to the square of the wave amplitude as:

$$I = \frac{1}{2}n\varepsilon_0 c\left|\hat{E}\right|^2 \tag{2.16}$$

therefore, the wave intensity as a function of distance z can be written as:

$$I(z) = I_0 e^{-2k_0\kappa z} = I_0 e^{-\alpha z} \tag{2.17}$$

where α denotes the attenuation constant ($\alpha = 2\kappa k_0 = \frac{4\pi}{\lambda_0}\kappa$) measured in km^{-1}. For example, α for a normal window glass is 11500 km^{-1}, while it is 0.04 – 0.07 km^{-1} in optical fibers for telecommunication wavelengths (1550 nm) [7]. Although the attenuation constant is small for optical fibers compared to the ordinary glass and the power losses are very low, they are not negligible if too long optical fibers are used. In principle, the wave intensity can be written as:

$$I = \frac{P}{A_{eff}} \tag{2.18}$$

where P is the wave power and A_{eff} is the effective area of the fiber core that the

wave propagates through. In case, when the effective area is constant during the wave propagation, then both the intensity and the power of the wave are related to the squared amplitude. Therefore, and referring to Eq. 2.17, the wave power will be introduced as:

$$\frac{dP(z)}{dz} = -\alpha P(z) \tag{2.19}$$

If z is changed with L: the propagation length, then Eq. 2.19 can be written as:

$$P(L) = P(0)e^{-\alpha L} \tag{2.20}$$

where $P(0)$ denotes the wave power at the fiber input.

2.2.2 Non-Linear Effects

Within a non-linear medium the relation between the polarization and the electric field is non-linear . The non-linearity originates mainly from either microscopic or macroscopic considerations. In general, the polarization density P can be considered as a product of dipole moment p induced by the applied electric field $\boldsymbol{E}$ and the dipole moments number density N, i.e. $P = pN$ [33]. Within the microscopic consideration, when the electric field strength is high enough typically 10^5-10^8 V/m, i.e. it has values near the inter-atomic electric field, then the relation between the dipole moment p and the electric field $\boldsymbol{E}$ becomes non-linear. In principle, the dipole moment $p = -ex$, here x is the mass displacement which has a charge $-e$ related to the applied electric force $-e\boldsymbol{E}$. When Hooke's law is satisfied [34], i.e. the restraining force is linearly proportional to the displacement then the equilibrium displacement x is proportional to $\boldsymbol{E}$. Hence, P is linearly related to $\boldsymbol{E}$ and the medium is linear. Additionally, when the restraining force is non-linearly functioning with the displacement, then the equilibrium displacement x and the polarization density P both are non-linearly related to the electric field $\boldsymbol{E}$. Therefore, the medium can be considered as non-linear.

In principle, if the dipole moments number density N of the medium depends on the incident electric field $\boldsymbol{E}$, then the macroscopic consideration takes place. In this case, the polarization is the summation of the discrete macroscopic field induced dipole moments of ith molecule, depending on the macroscopic symmetry of the medium. Hence, the polarization can be expressed as:

$$\boldsymbol{P}(t) = \sum_{i=1}^{N} \boldsymbol{P}_i(t) \tag{2.21}$$

and therefore the macroscopic polarization can be expressed as a power Taylor series [33, 35]:

$$\boldsymbol{P}(t) = \varepsilon_0(\chi^{(1)}E(t) + \chi^{(2)}E^2(t) + \chi^{(3)}E^3(t) + ...) \tag{2.22}$$

The susceptibility terms $\chi^{(i=1,2,3,...)}$ (linear and non-linear) are tensors of rank $(i+1)$. In principle, the susceptibility defines the relation between the induced polarization if it is linear or non-linear. Additionally, it describes whether the electric fields produce phase shifts or waves with new frequencies, and if the incident field will be absorbed or amplified. The first order susceptibility $\chi^{(1)}$ refers to the dipole excitation with bound and free electrons produced by a single photon. In principle, the real part of $\chi^{(1)}$ is related to the real part of the refractive index, while the imaginary part of $\chi^{(1)}$ refers to the gain or loss.

The energy level diagram in Fig. 2.2 (a) illustrates the dipole excitation related to $\chi^{(1)}$ processes as a contribution to the refractive index through atomic dipole oscillation between the ground and the virtual states. Additionally, Fig. 2.2 (b) refers to another $\chi^{(1)}$ contribution which originates from free carrier absorption to the photons with non-radiative recombination, hence contributes to the refractive index.

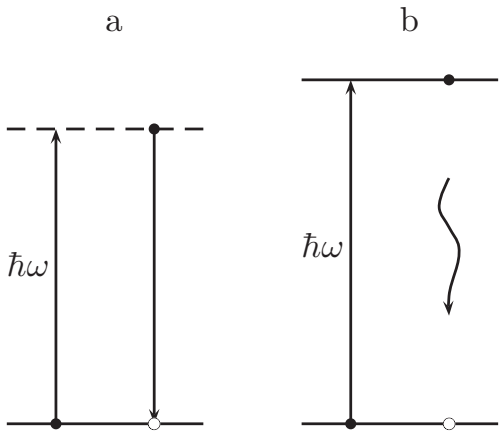

Figure 2.2: Energy level diagrams illustrate the possible single photon dipole transitions associated to refractive index change (a), free carrier absorption (b).

Referring to Eq. 2.6, the linear polarization can be written as:

$$\boldsymbol{P}_L^{(1)}(\omega) = \varepsilon_0\chi^{(1)}(\omega)\boldsymbol{E}(\omega) \tag{2.23}$$

Within the same frequency ω, both the polarization and the incident electric field are linearly related including the linearity constant $\chi^{(1)}$. Hence and referring to Eq. 2.9, the primary wave promotes the dipoles to oscillate with its frequency ω and the secondary wave has a phase shift without any new frequency components. Having the fact that the susceptibility is a tensor of $(i+1)$ rank, then Eq. 2.23 can be written as:

$$\boldsymbol{P}_{Li}^{(1)}(\omega) = \varepsilon_0 \sum_j \chi_{ij}^{(1)}(\omega)\boldsymbol{E}_j(\omega) \tag{2.24}$$

where $i, j = x, y, z$. Here, the first order susceptibility tensor ($\chi_{ij}^{(1)}$) contains nine elements (3^1x3). Depending on the material symmetry arguments, the susceptibility tensor can be reduced. For example and according to [36], the first order susceptibility tensor $\chi^{(1)}$ of an isotropic material contains a single frequency dependent element. As mentioned earlier, this contributes to refractive index.

The second order susceptibility $\chi^{(2)}$ depends on the combination of the input frequencies, since the external fields can interact with each other and nine field combinations are possible. For example, when the incident field has two different frequencies, then they achieve a second order polarization at the sum, difference or multiples of the incident frequencies. And therefore, the secondary wave contains new as well as the original frequency components. Additionally, the second order susceptibility $\chi^{(2)}$ is related to the incident field vectors as well as the field vector of the polarization. Therefore, the second order non-linear polarization which connect two incident fields can be written as:

$$\boldsymbol{P}_{NLi}^{(2)}(\omega_1, \omega_2) = \varepsilon_0 \chi^{(2)}(\omega_1, \omega_2)\boldsymbol{E}(\omega_1)\boldsymbol{E}(\omega_2) \tag{2.25}$$

Having the fact that the second order susceptibility $\chi_{ijk}^{(2)}$ has 27 elements (3^2x3) and only 9 field combinations (3^2) are possible, therefore Eq. 2.25 can be written as:

$$\boldsymbol{P}_{NLi}^{(2)}(\omega_1, \omega_2) = \varepsilon_0 \sum_{jk} \chi_{ijk}^{(2)}(\omega_1, \omega_2)\boldsymbol{E}_j(\omega_1)\boldsymbol{E}_k(\omega_2) \tag{2.26}$$

where, $i, j, k = x, y, z$.

Eq. 2.25 is responsible for all the second order non-linear effects. Since optical fibers are made from silica glass which has a symmetry center, all the 27 tensor elements of the second order susceptibility $\chi^{(2)}$ are zero. Therefore, the second order non-linear effects can be ignored.

The third order susceptibility tensor $\chi^{(3)}$ consists of 81 elements ($3^3 \times 3$) for three directions and the third order polarization P_{NL}^3 connects three fields, therefore 27 field combinations (3^3) are possible. As in the second order case, the polarization will be produced at the sum, difference or multiples of the incident frequencies. The third order polarization can be written as:

$$\boldsymbol{P}_{NLi}^{(3)}(\omega_1, \omega_2, \omega_3) = \varepsilon_0 \chi^{(3)}(\omega_1, \omega_2, \omega_3)\boldsymbol{E}(\omega_1)\boldsymbol{E}(\omega_2)\boldsymbol{E}(\omega_3) \tag{2.27}$$

and in summation form:

$$\boldsymbol{P}^{(3)}_{NLi}(\omega_1,\omega_2,\omega_3) = \varepsilon_0 \sum_{jkl} \chi^{(3)}_{ijkl}(\omega_1,\omega_2,\omega_3)\boldsymbol{E}_j(\omega_1)\boldsymbol{E}_k(\omega_2)\boldsymbol{E}_l(\omega_3) \tag{2.28}$$

where, $i,j,k,l = x,y,z$ directions.

Referring to Eq. 2.11 where $n = \sqrt{\varepsilon_r} = \sqrt{\chi^{(1)}+1}$, the non-linear wave equation for a non-linear medium will be:

$$\Delta\boldsymbol{E} = \underbrace{\frac{1}{c^2}\frac{\partial^2 \boldsymbol{E}}{\partial t^2}}_{L} + \underbrace{\frac{1}{c^2}\chi^{(1)}\frac{\partial^2 \boldsymbol{E}}{\partial t^2} + \frac{1}{c^2}\chi^{(2)}\frac{\partial^2 \boldsymbol{EE}}{\partial t^2} + \frac{1}{c^2}\chi^{(3)}\frac{\partial^2 \boldsymbol{EEE}}{\partial t^2} + ...}_{NL} \tag{2.29}$$

and therefore:

$$\Delta\boldsymbol{E} - \frac{n^2}{c^2}\frac{\partial^2 \boldsymbol{E}}{\partial t^2} = \frac{1}{c^2}\frac{\partial^2}{\partial t^2}\left(\chi^{(2)}\boldsymbol{EE} + \chi^{(3)}\boldsymbol{EEE} + ...\right) \tag{2.30}$$

Since the second order susceptibility χ^2 is depending on the material symmetry, the first term on the right hand side of Eq. 2.30 will be zero for a material with inversion symmetry. Therefore, the second order non-linear effects like second order harmonics, sum and difference frequency generation do not exist within such materials.

A variety of non-linear effects exhibit from the second term on the right hand side of Eq. 2.30 (third order non-linearity) such as:
Self Phase Modulation (SPM)
Cross Phase Modulation (XPM)
Four Wave Mixing (FWM)
In principle, these effects limit the optical transmission capacity within optical communication systems. Additionally, some of them such as Brillouin scattering , offer interesting applications for optical filtering and amplification.

2.3 Brillouin Scattering Physics

Brillouin scattering is a third order non-linear effect by which optical photons are coupled to acoustic phonons, i.e. two optical modes are coupled through an elastic mode. In other words, the incident optical wave for instance, will be deviated via the density fluctuations within the transfer medium i.e. refractive index variation associated with a sound wave of the frequency Ω. The sound velocity of the acoustic wave that causes the

density fluctuations (grating) is denoted as ($\boldsymbol{\nu}_A$). The frequencies of incident (pump), Stokes (scattered) and acoustic waves are denoted as f_P, f_S and f_A, respectively. The wave vectors of the pump, Stokes and acoustic waves will be denoted as: $\boldsymbol{k}_P, \boldsymbol{k}_S$ and $\boldsymbol{k}_A$, respectively.

Fig. 2.3 illustrates the Brillouin scattering process via medium induced density variations which originate from the acoustic wave in two directions, (a) and (b), traveling with sound velocity ($\boldsymbol{\nu}_A$) and having the angle θ with the incident optical pump field.

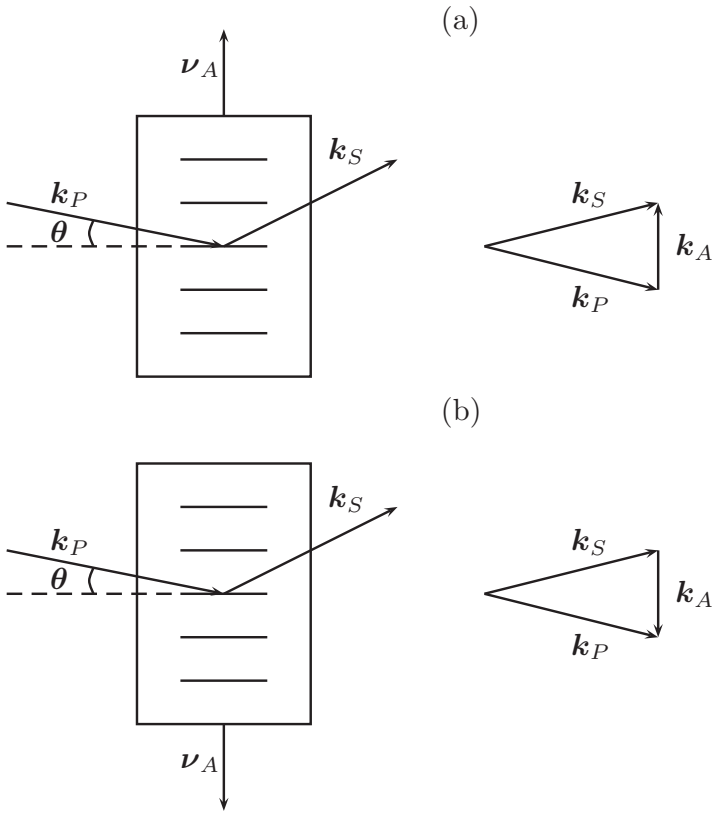

Figure 2.3: Brillouin scattering process illustration at medium density fluctuations for two directions (a) and (b) with sound velocity ($\boldsymbol{\nu}_A$) and wave vectors representation.

The Energy ($\hbar\omega$) and momentum ($\hbar k$) are conserved during the scattering process. Therefore, according to the vector diagrams in Fig. 2.3 the condition can be written as:

$$\boldsymbol{k}_S = \boldsymbol{k}_P \mp \boldsymbol{k}_A \tag{2.31}$$

and hence, the scattered wave frequency will be:

$$f_S = f_P \mp f_A \tag{2.32}$$

Therefore and according to the Doppler effect, if the wavefront of the acoustic wave moves away from the incident light, the scattered wave has a down-shifted frequency ($\omega_s = \omega_p - \Omega$), as illustrated in Fig. 2.4 (a) the red arrows. While, if the acoustic wavefront moves in opposite direction then the scattered wave frequency is up-shifted ($\omega_s = \omega_p + \Omega$), refer to Fig. 2.4 (a) the black arrows.

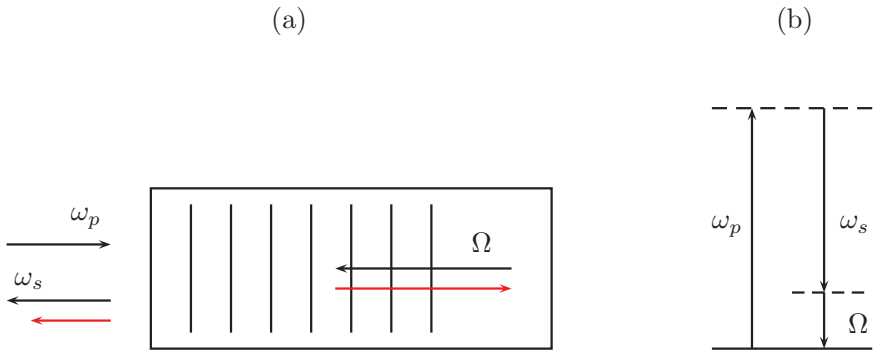

Figure 2.4: (a) Illustration of the up-shifted and down-shifted scattered wave frequencies (black and red arrows) illustrations, respectively. (b) Photon-phonon energy level diagram interaction of the Brillouin process.

As represented in Fig. 2.4 (b), the acoustic frequency is much smaller than the incident pump frequency. Therefore, one can assume that the absolute wave vector values of both the incident and scattered waves are approximately equal ($|\boldsymbol{k}_P| \approx |\boldsymbol{k}_S|, \omega_p \approx \omega_s$). According to this assumption, the angle (θ) shown in Fig. 2.3 will be the half angle between the incident pump and scattered (Stokes) waves as illustrated via an isosceles triangle in Fig. 2.5, and therefore the absolute acoustic wave vector will be:

$$|k_A| = 2\,|k_P| \sin\theta \tag{2.33}$$

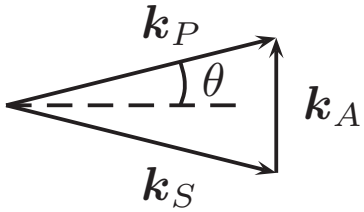

Figure 2.5: Isosceles triangle illustrates the wave vector diagram of the pump, Stokes and acoustic waves. The dashed line represents the grating.

Having the fact that the absolute value of the acoustic wave vector is ($|k_A| = \frac{\Omega}{\boldsymbol{\nu}_A}$), and the absolute value of the pump wave vector is ($|\boldsymbol{k}_P| = \frac{2\pi n}{\lambda_{P_0}}$), therefore the acoustic frequency which in turn is the frequency shift of the backscattered wave can be written as:

$$f_A = \frac{2n\boldsymbol{\nu}_A}{\lambda_{P_0}} \sin\theta \tag{2.34}$$

where λ_{P_0} is the wavelength of the optical pump in free space, n is the refractive index and θ is the angle between the incident pump wave and the grating, see Fig. 2.5. From Fig. 2.3 and referring to Fig. 2.5, one can see that if ($\theta = 0$) i.e. both the Stokes and the pump have the same direction (forward), then ($f_A = 0$). Therefore, no frequency shift between the Stokes and the pump exists. Contrary, when ($\theta = \pi/2$) i.e. the Stokes and the pump have opposite directions, then the frequency shift will be maximum (backward), since ($\sin\pi/2 = 1$).

Additionally, Eq. 2.34 can be rewritten as:

$$f_A = 2\boldsymbol{\nu}_A f_P(\frac{n}{c}) \sin\theta \tag{2.35}$$

where (c/n) is the velocity of light in the medium. If that medium is assumed to be a pure silica glass, then with the acoustic velocity $\boldsymbol{\nu}_A = 5.96$ km/s [37] and the refractive index ($n = 1.44$) at a wavelength of 1550 nm, the frequency shift of the Stokes wave will be $f_A \approx 11.4$ GHz. Referring to Eq. 2.32 and Fig. 2.4 (b), the Stokes wave frequency is smaller than the pump wave frequency.

2.4 Spontaneous and Stimulated Brillouin Scattering

A light scattering is said to be spontaneous, when the medium periodic density modulations i.e. the refractive index changes (grating) are caused by thermal or quantum mechanical zero-point effects [1], and the amount of scattering is proportional to the incident field intensity. Additionally, a light scattering is said to be stimulated, when the density modulations are induced or excited via a high intensity incident field. Therefore, the density fluctuations are caused by the incident field itself and a large amount of the incident power will be transferred to the scattered wave (Stokes). The most interesting light scattering here is the stimulated Brillouin scattering (SBS).

In principle, the spontaneous Brillouin scattering is caused by the pump wave scattering at an arbitrary density modulation of the medium, i.e. at the acoustic waves. The density modulation itself is a superposition of many monochromatic plane acoustic waves. Each acoustic wave is leading to a spatial and temporal density modulation within the medium. Due to the energy and momentum conservation requirement for the Brillouin scattering, the spontaneous Brillouin scattering is very weak since not all the acoustic

waves could generate a Stokes wave.

Contrary to the spontaneous Brillouin scattering, the SBS is a result of a high incident field in the optical medium. Therefore, a beating (interference) between the incident pump wave and the back scattered wave (Stokes) will take place. In principle when the pump power is high enough, then the power transfer from the pump to the Stokes is higher than the attenuation within the medium. Additionally, the interference between the pump and Stokes waves contains a frequency component at a frequency difference between the pump and Stokes waves i.e. at the acoustic frequency (Ω) and in the direction of the pump wave.

The medium will response to that interference in a way that will act as a new source for the sound wave and increase the acoustic amplitude. Hence, the interference results into reinforce (amplification) to the acoustic wave. In principle, the superposition between the pump and Stokes waves results in a fading with the acoustic frequency. Therefore, an intensity modulation in the direction of the pump wave will take place. Afterwords, the intensity modulation will be translated to a density modulation through an electrostriction effect. A high pump wave results in a higher interference and therefore, a stronger acoustic wave and stronger Stokes will be generated and so on, which is called stimulation. Under certain conditions i.e. sufficient temporal and spatial coherence of the pump source, the positive interference feedback achieves exponential growth (amplification) of the Stokes amplitude [38, 39]:

$$I_{S_{(Output)}} = I_{S_{(Input)}} \underbrace{\exp(g_B I_{P(L)} L_{eff})}_{G} \tag{2.36}$$

$$L_{eff} = \frac{[1 - \exp(-\alpha z)]}{\alpha} \tag{2.37}$$

where $I_{S_{(Output)}}$ and $I_{S_{(Input)}}$ are the scattered wave (Stokes) output and input intensities at $z = 0$ and $z = L$, respectively as illustrated in Fig. 2.6.

The length of the optical fiber is denoted as L and the specific length position as z. The factor G refers to the Stokes amplification as a function of the gain coefficient g_B, pump intensity $I_{P(L)}$ and the fiber interaction length (effective length) L_{eff}, see Fig. 2.7. The gain coefficient g_B is a function of the frequency shift $\Delta\Omega$ from the gain center and depends on the optical fiber properties and the scattering environments. Eq. 2.36 (which will be derived in the next section) shows that the Stokes intensity strongly depends on the pump intensity $I_{P(L)}$, therefore if the pump intensity is increased by a small magnitude, the Stokes intensity will be increased by orders of magnitude. Additionally, at the gain center when the frequency shift $\Delta\Omega = 0$ which is called resonance frequency and will be denoted as $\Omega_B(0)$, the Stokes intensity reaches the maximum value which is called gain maximum or resonance condition ($g_B(0)$).

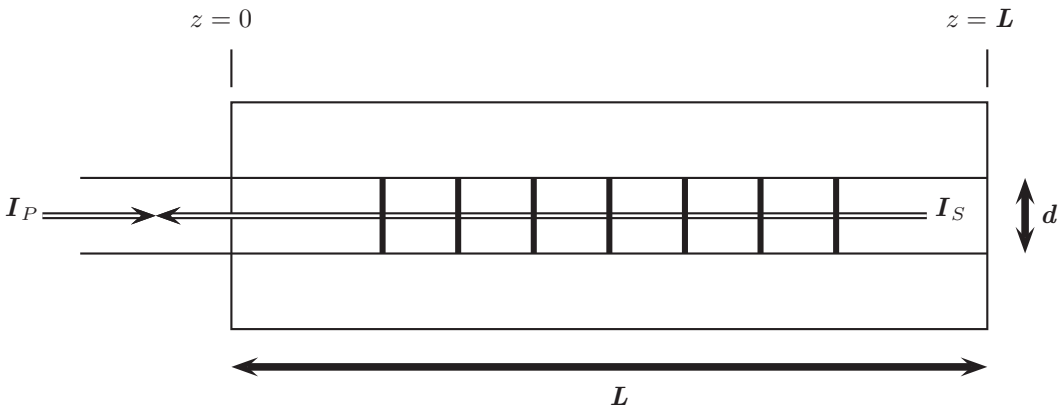

Figure 2.6: Schematic representation of the SBS process.

As shown in Fig. 2.5 and Fig. 2.6 where $\theta = \pi/2$, the back scattered SBS (BSBS) is considered to be the dominant process for the following facts:

1. Within BSBS, and when $\theta = \pi/2$ the maximum gain value is along the axis of the beam and directly related to the effective length L_{eff}. While for other angles, L_{eff} depends on the beam diameter d, see Fig. 2.6.

2. The minimum acoustic response time occurs at $\theta = \pi/2$ [38].

3. If the pump and Stokes waves interference includes fields with complex wavefront and spatial structure, then a higher increasing rate of the Stokes takes place. Hence, the scattered mode will be spatially correlated with the pump beam only over a cumulative interference length for BSBS direction. Additionally, that spatial correlation of the Stokes leads to an important phenomenon which is called Phase Conjugation or Wave Reversal.

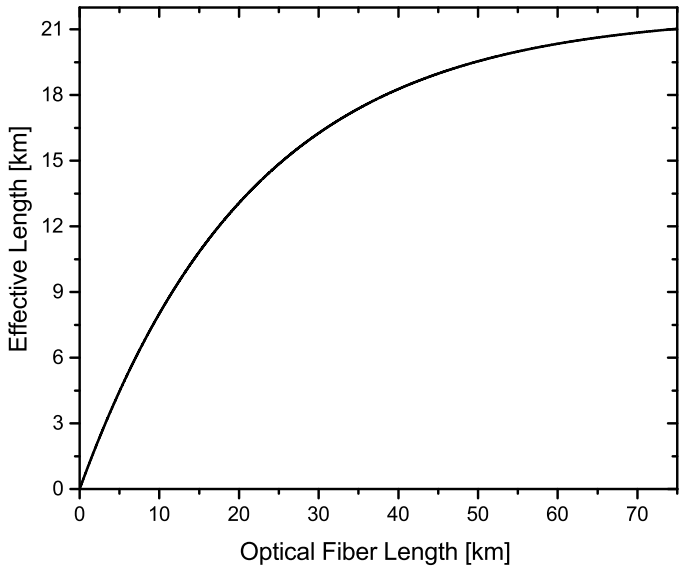

Figure 2.7: Effective optical fiber length versus the real optical fiber length using Eq. 2.37 with fiber attenuation constant α=0.2 dB/km.

2.5 Mathematical Description of SBS

Through the SBS process, the interference (the non-linear coupling) among the pump, Stokes and acoustic waves can be described by the non-linear wave equation (Eq. 2.30). Contrary, the spontaneous scattering process can be described by linear optics. In principle, Eq. 2.27 is responsible for the stimulated scattering process. According to the slowly varying envelope approximation [40], the wavefront varies slowly compared to the optical period. Hence, and referring to Eq. 2.29 one can neglect the second derivatives with respect to the space propagation direction (z) and the time (t), since $[\partial^2 E_j/\partial z^2 << k_j(\partial E_j/\partial z)]$ and $[\partial^2 E_j/\partial t^2 << \omega_j(\partial E_j/\partial t)]$. Therefore, the non-linear part of Eq. 2.29 can be rewritten as:

$$\frac{i\omega_j}{2\epsilon_0 c n_j} P_j^{NL} \exp\left(\mp i k_j z\right) = \mp\frac{i}{2k_j}\nabla_T^2 E_j + \frac{n_j}{c}\frac{\partial E_j}{\partial t} \mp \frac{\partial E_j}{\partial z} + \frac{1}{2}\alpha E_j \tag{2.38}$$

where the squared Nabla operator diffraction of the wave is: $\nabla_T^2 = (\partial^2/\partial x^2) + (\partial^2/\partial y^2)$.

Additionally, the non-linear polarization is connected to the medium density ρ and

the temperature T as follows [38]:

$$P_{NL} = \left[\underbrace{\left(\frac{\partial \varepsilon}{\partial \rho}\right)_T \Delta\rho}_{Electrostriction} + \underbrace{\left(\frac{\partial \varepsilon}{\partial T}\right)_\rho \Delta T}_{Absorption} \right] \boldsymbol{E} \tag{2.39}$$

where $\Delta\rho$ and ΔT are the intensity dependent modifications of the density and temperature amplitudes, respectively.

In general, for optical fibers the interference between the pump and the Stokes waves can drive the acoustic wave via two different physical mechanisms. The first mechanism (the first term in Eq. 2.39) is the electrostriction which can be defined as the tendency of media to become more dense (mechanical deformation or strain) in regions of high optical intensity. Therefore, within electrostriction which is the major SBS mechanism in optical fibers, the density fluctuations are induced by electric field interactions between the pump and the Stokes waves.

The other mechanism (the second term in Eq. 2.39) is the optical absorption. Within the regions of high optical pump intensity, the heat evolved by absorption leads for causing the optical material to extend in those regions. The density fluctuations involved by this effect can excite an acoustic disorder. Absorptive SBS is less commonly used than electrostrictive SBS, since it can occur only in lossy optical media (absorbing medium). The absorptive SBS is also called stimulated temperature Brillouin scattering (STBS). Within the next mathematical description, we will consider that ($\Delta T = 0$), i.e. no absorbing medium is available and neglecting all the intensity dependent temperature effects. Additionally, we will treat the waves as plane waves for simplicity, i.e. the transverse components ($\nabla_T = 0$). Therefore, Eq. 2.15 can be rewritten as:

$$\begin{aligned} \mathbf{E}(z,t) = & \underbrace{\frac{1}{2}\left[\hat{E}_P \exp\left[i(k_P z - \omega_P t)\right] + \hat{E}_P^* \exp\left[-i(k_P z - \omega_P t)\right]\right]}_{pump} + \\ & \underbrace{\frac{1}{2}\left[\hat{E}_S \exp\left[i(k_S z - \omega_S t)\right] + \hat{E}_S^* \exp\left[-i(k_S z - \omega_S t)\right]\right]}_{Stokes} \end{aligned} \tag{2.40}$$

Eq. 2.40 describes the pump and Stokes waves, where $\hat{E}_P\hat{E}_P^* = \left|\hat{E}_P\right|^2$ and $\hat{E}_S\hat{E}_S^* = \left|\hat{E}_S\right|^2$. Having ($k_A = k_P + k_S \cong 2k_P$), see Fig. 2.5 and ($\Omega = \omega_p - \omega_s$), see Fig. 2.4, since the pump and acoustic waves are traveling in the ($+z$) direction while the Stokes is traveling in the ($-z$) direction. In general, the acoustic frequency has a small detuning from the resonance frequency Ω_B, therefore ($\Delta\Omega = \Omega - \Omega_B$). Additionally, if a small

variation in the medium density is considered ($\Delta\rho = \rho^{'} - \rho_0$): where ρ_0 is the average density, which is evolved by the pump field, the medium density wave can be written as:

$$\Delta\rho = \frac{1}{2}\left[\rho \exp\left[i(k_A z - \omega t)\right] + c.c\right] \tag{2.41}$$

As mentioned earlier, the medium becomes more dense in the regions of high optical field, since the medium is mainly response to the superposition of the pump and Stokes waves, i.e. at the beat frequency ($\Omega = \omega_p - \omega_s$) which travels at a velocity:

$$\nu_A = \frac{\omega_p - \omega_s}{k_P + k_S} \tag{2.42}$$

Therefore, and according to the energy and momentum conservation (corresponding to resonance), the electrostrictive deriving force remains in phase with the generated acoustic wave. Hence, and from Eq. 2.28 the pump and Stokes field equations can be written as [38]:

$$\frac{\partial E_P}{\partial z} + \frac{n}{c}\frac{\partial E_P}{\partial t} + \frac{1}{2}\alpha E_P = \frac{i\omega_p}{4cn_p}\frac{\gamma_e}{\rho_0}E_S\rho \tag{2.43}$$

$$-\frac{\partial E_S}{\partial z} + \frac{n}{c}\frac{\partial E_S}{\partial t} + \frac{1}{2}\alpha E_S = \frac{i\omega_s}{4cn_s}\frac{\gamma_e}{\rho_0}E_P\rho^* \tag{2.44}$$

having the electrostriction coefficient ($\gamma_e = \rho_0(\partial\epsilon/\partial\rho)_T$). The non-linear disorder amplitude within the medium density ρ is obtained by combining the equation of continuity with the Navier–Stokes equation including an electrostrictive force, therefore, the material description equation will be:

$$\frac{\partial^2\rho}{\partial t^2} - 2i\Omega\frac{\partial\rho}{\partial t} - (\Omega^2 - \Omega_B^2 + i\Omega\Delta\Omega_B)\rho = \frac{\gamma_e\varepsilon_0 k_B^2}{2}E_P E_S^* \tag{2.45}$$

where $\Delta\Omega_B$ is the linewidth of the Brillouin distribution FWHM (full-width at half-maximum) and k_B is the Brillouin wave vector. Since the acoustic wave does not propagate significantly on the timescale of the scattering i.e. $\nu_A \ll c/n$, the spatial derivative of the acoustic field is neglected in Eq. 2.45. In principle, the right hand side of Eq. 2.45 is representing the electrostriction force that induces the high density in the regions of high pump field. Therefore, Eq. 2.45 is forming a forced damped harmonic

oscillator. Additionally, in practical case one can assume that the acoustic wave amplitude growth is slow in comparison to the acoustic frequency, therefore the approximation ($\partial^2\rho/\partial t^2 \ll 2\Omega(\partial\rho/\partial t)$) is valid. In principle, if the SBS process is driven by a very short pulse i.e. the acoustic period ≈ 1 ns, then the above approximation is not valid.

As mentioned earlier, if a small detuning from resonance is considered, i.e. ($\Omega^2 - \Omega_B^2 = (\Omega + \Omega_B)(\Omega - \Omega_B) \approx 2\Omega_B\Delta_\Omega$), then the acoustic wave can be described as:

$$\frac{\partial\rho}{\partial t} + (-i\Delta_\Omega + \frac{\Delta\Omega_B}{2})\rho = \frac{i\gamma_e\varepsilon_0 k_B}{4\nu_A}E_P E_S^* \tag{2.46}$$

In general, and by the consideration of plane wave interaction, the SBS process can be described by Equations 2.43, 2.44 and 2.46 regarding time and space. In case of a steady state set of equations, i.e. the time derivatives are zero, then the density wave will be:

$$\rho = \frac{i\gamma_e\varepsilon_0 k_B}{4\nu_A}\frac{1}{(1 - 2i\Delta_\Omega/\Delta\Omega_B)}E_P E_S^* \tag{2.47}$$

Having the intensity-field relation ($I_j = \varepsilon_0 cn\left|E_j\right|^2/2$) and by inserting Eq. 2.47 into equations 2.43 and 2.44, one can obtain the set of the two coupled non-linear equations that describes the relation between the pump and Stokes waves for approximately monochromatic waves or relatively long pulses:

$$\frac{dI_P}{dz} = -g_{Bp}I_P I_S \tag{2.48}$$

$$\frac{dI_S}{dz} = -g_{Bs}I_P I_S \tag{2.49}$$

As mentioned earlier, that the frequency shift between the pump and Stokes wave is small ($f_A \approx 11.4$ GHz). This leads to the consideration that the Stokes wave frequency is approximately equal to the pump wave frequency. Hence, one can assume that both the Brillouin gain coefficient and the attenuation factor are approximately equal for the pump and Stokes waves. Therefore, ($g_{Bp} \approx g_{Bs}, \alpha_p \approx \alpha_s$). Now, the steady state Brillouin gain coefficient (g_B) can be given as:

$$g_B = \Omega_B(0)\frac{1}{1 + (2\Delta\Omega/\Delta\Omega_B)^2} \tag{2.50}$$

and the maximum gain coefficient at resonance is:

$$\Omega_B(0) = \frac{\omega_s^2(\gamma_e)^2}{c^3 \nu_A \rho_0 \Delta\Omega_B} \tag{2.51}$$

Additionally, if the loss inside the medium is considered, then the attenuation factor α should be added. Therefore, Equations 2.48 and 2.49 can be rewritten as:

$$\frac{dI_P}{dz} = -g_B I_P I_S - \alpha_p I_P \tag{2.52}$$

$$\frac{dI_S}{dz} = -g_B I_P I_S + \alpha_s I_S \tag{2.53}$$

where ($\alpha_p \approx \alpha_s = \alpha$) are the attenuation constants for the pump and Stokes wave, respectively, which both are approximately equal, as mentioned earlier. In principle, equations 2.52 and 2.53 show that there is a power transfer from the pump wave to the Stokes wave ($-g_B$), in addition it is attenuated within the medium via (α). The Stokes wave growth in the backward direction ($-z$) and shows an exponential growth while the pump wave shows a depletion. With low intensities, the pump depletion is rather small. Therefore, the first term in Eq. 2.52 can be neglected and can be represented as:

$$I_P(z) = I_P(0) \exp(-\alpha z) \tag{2.54}$$

Eq. 2.54, shows that, under the above simplifications the pump intensity depends only on the attenuation of the fiber, and at any fiber position (L) the pump intensity can be written as:

$$I_P(L) = I_P(0) \int_0^L e^{-\alpha z} dz = \frac{I_P(0)}{\alpha}(1 - e^{-\alpha L}) = I_P(0) L_{eff} \tag{2.55}$$

If the pump intensity is not effected by the Brillouin process, then Eq. 2.53 can be represented as:

$$\frac{dI_S}{dz} = (-g_B I_P + \alpha) I_S \tag{2.56}$$

Now, by substituting Eq. 2.55 into Eq. 2.56, the Stokes intensity at any position (L) can be given as:

$$I_S(L) = I_S(0)e^{-g_B P_0 L_{eff}/A_{eff}+\alpha L} \tag{2.57}$$

where $I_S(0)$ is the Stokes intensity at the fiber input ($z = L$) and can be written as:

$$I_S(0) = I_S(L)e^{g_B P_0 L_{eff}/A_{eff}-\alpha L} \tag{2.58}$$

Fig. 2.8 shows the exponential growth of the Stokes wave versus a polarization maintaining optical fiber length according to Eq. 2.58 for three pump powers: 1.5, 1.4 and 1.3 mW. The initiating wave power $I_S(L)$ at the fiber input was 1x10^{-10} W for the three pump powers, which is required at the position L with the right frequency shift to generate the Stokes wave. In principle, $I_S(L)$ can be initiated by: the spontaneous scattering or the noise floor within the optical fiber.

It can be clearly seen from Fig. 2.8 that if the optical fiber is longer than 20 km the Stokes wave grows rapidly. Additionally, at about 65 km optical fiber length the Stokes wave power reaches its maximum and starts to decrease again for longer fiber due to the fiber attenuation. This means that at longer optical fibers the loss is greater than the amplification by the Brillouin process.

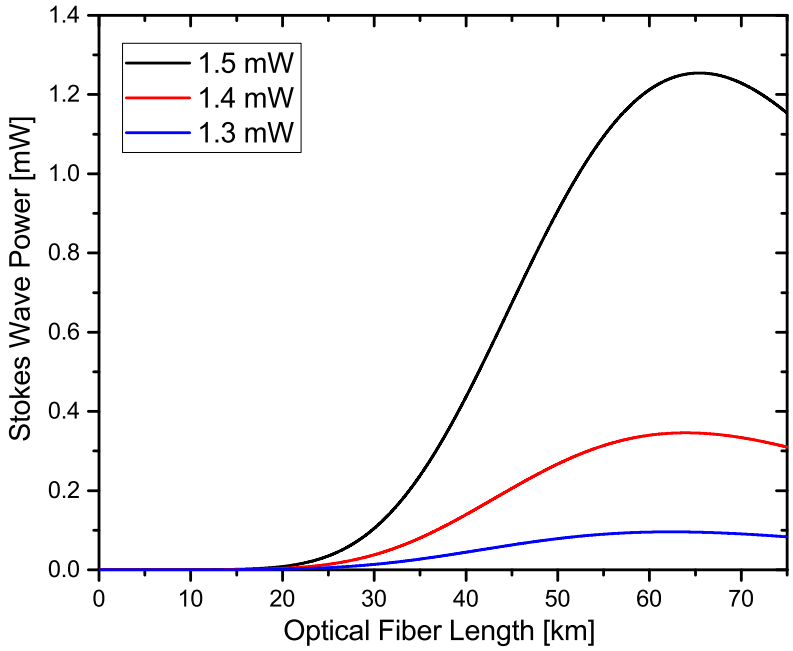

Figure 2.8: Stokes wave powers at the input of the optical fiber versus optical fiber length for three pump powers.

2.6 Brillouin Scattering Factors

2.6.1 The Brillouin Gain

In principle and referring to Eq. 2.50, the Brillouin gain coefficient (g_B) depends on:

1. The linewidth distribution ($\Delta\Omega_B$).

2. The maximum gain (g_{Bmax}) or ($g_B(0)$).

3. The frequency shift between the pump and Stokes waves (f_A) or (Ω).

Fig. 2.9 shows the Brillouin gain Lorentzian distribution according to Eq. 2.50, where ($g_{B(0)} = 2e^{-11}$ m/W, $\Omega_B = 11.25$ GHz and the full-width at half-maximum (FWHM) $\Delta\Omega_B = 35$ MHz). Eq. 2.50 represents the general form of the Brillouin gain distribution where the pump wave spectrum is a quasi- monochromatic wave. However, if relatively short pump pulses are used then the gain distribution converges towards a Gaussian distribution, since high power will be provided [7].

In principle, the Brillouin gain distribution has a very narrow linewidth, as mentioned above. This feature made the SBS the most attractive non-linear effect for optical filters.

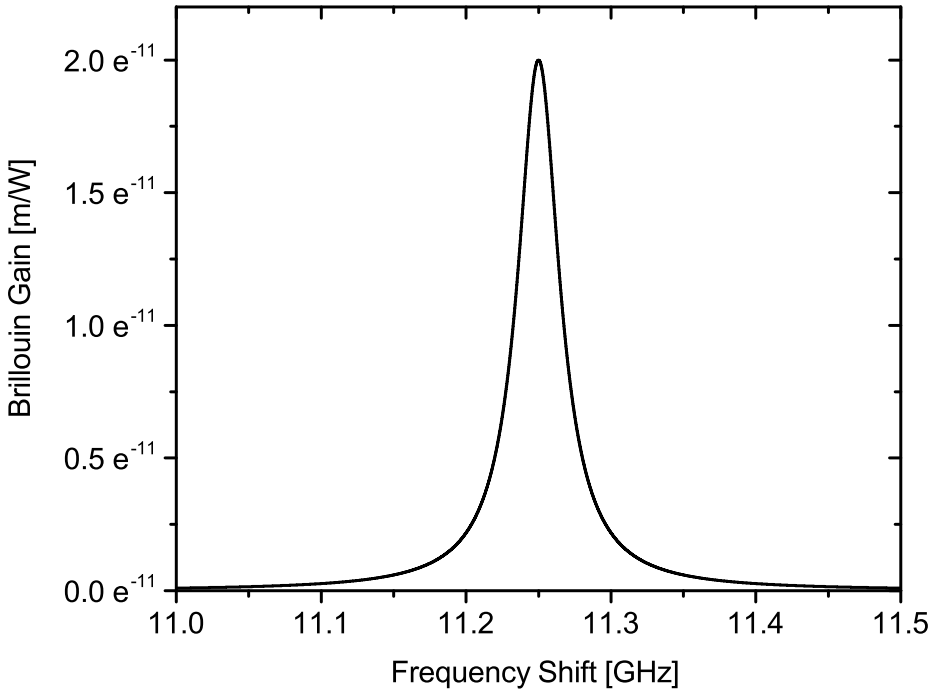

Figure 2.9: Brillouin gain Lorentzian distribution against frequency shift $\Delta\Omega$.

However, many attempts had been done to reduce the SBS linewidth even further as we will see later.

Referring to Eq. 2.34 regarding the frequency shift, it is worthwhile to mention that in addition to the longitudinal acoustic modes that travel with sound velocity ν_A, there are other transverse vibrational modes in the core and cladding of a cylindrical waveguide. In principle, these modes have their own resonance frequencies since they depend on the medium density at the core and cladding in addition to the interference between these modes. These transverse modes could also scatter light within the medium, therefore it can be predicted that several Brillouin gain distribution maxima ($g_{B(max)}$) exist. Additionally, and referring to Eq. 2.51, the Brillouin gain maxima ($g_{B(max)}$) depends on the pump wave linewidth, medium properties and characteristics.

In principle, the acoustic fluctuation and the corresponding phonon has a life time, therefore the Brillouin process is not instantaneous. Hence, the scattering process efficiency is highly affected by the ratio between the life time and the temporal duration of the pump excitation. For example, if the phonon life time is much lower than the excitation temporal duration time of the pump pulses, then the maximum gain ($g_{B(max)}$) and the linewidth distribution ($\Delta\Omega_B$) both depend on the material characteristics [7].

While, if both the phonon life time and the excitation temporal duration time of the pump were in the same range, the gain maxima will be decreased. Therefore, Eq. 2.51 can be rewritten as [7]:

$$g_{B(max)} = \frac{\pi f_A^2 M_2}{2nc\Delta\Omega_B} \left(\frac{\Delta\Omega_B}{\Delta\Omega_B \otimes \Delta f_p} \right) \tag{2.59}$$

where (M_2) is the elasto-optic figure of merit, Δf_p is the spectral width of the pump wave and $\otimes$ is the convolution between the two waves. Therefore, for Lorentzian distribution one can have:

$$\Delta\Omega_B \otimes \Delta f_p = \sqrt{\Delta\Omega_B^2 + {\Delta f_p}^2} \tag{2.60}$$

and for Gaussian distribution:

$$\Delta\Omega_B \otimes \Delta f_p = \Delta\Omega_B + \Delta f_p \tag{2.61}$$

Additionally, the Brillouin gain coefficient (g_B) is affected by other environmental circumstances such as temperature, mechanical influences like stress, strain or other fiber distortions. In principle, these effects are disadvantages for several applications. Nevertheless, they can be used for distributed temperature and strain measurements.

The third parameter that affects the Brillouin gain maxima is the frequency shift (f_A). As mentioned earlier, f_A represents the first Brillouin gain maximum for a longitudinal mode. Referring to Eq. 2.35, it is clear that the frequency shift depends on the longitudinal mode sound velocity, pump wave frequency and the refractive index of the optical medium. For example, the refractive index and the acoustic velocity depend on the optical fiber dopant concentration. Higher dopant concentration leads to slower acoustic velocity and on the other hand it increases the refractive index, and therefore the frequency shift will be decreased. Additionally, within optical fibers the temperature and mechanical strain have a great influence on the frequency shift.

2.7 Pump Depletion Effects in SBS

Referring to Eq. 2.58, and by the assumption of invariant pump power, one can predict that the Stokes wave would experience an exponential growth through its propagation within optical fiber. This behavior is shown in Fig. 2.10 (green curve). The arrows

are referring to the directions of propagation, i.e $L = 0$ is the fiber input for the pump wave as well as it is the fiber output for the Stokes wave. In principle, when the Stokes power is growing to an analogous power of the pump wave, then a significant pump power depletion must take place because of the power transfer from the pump to the Stokes. The input pump power level at which the Stokes power level at the optical fiber input is comparable to that of the pump power level (transmitted power) is called: threshold pump power (critical pump power of the Brillouin scattering process) and governed by the following relation:

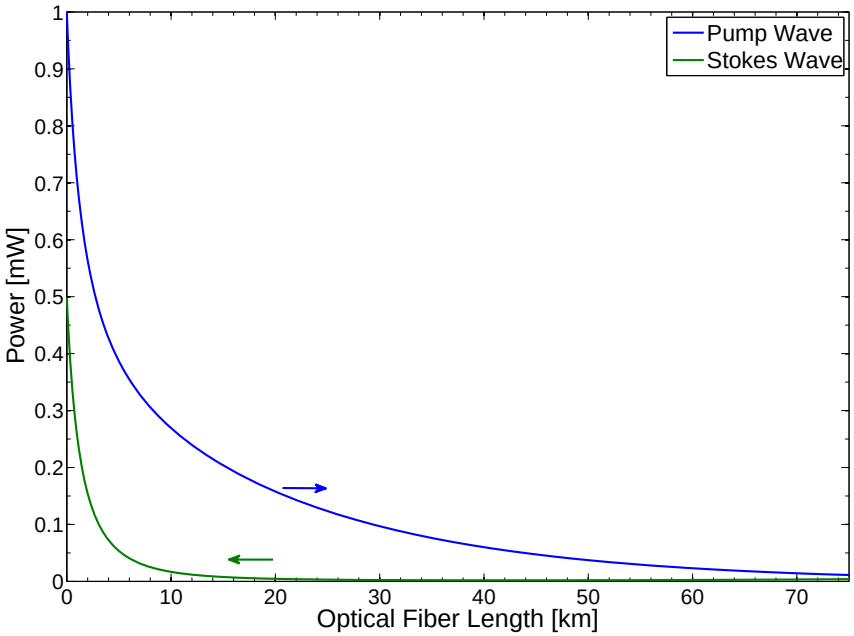

Figure 2.10: Pump and Stokes waves power behavior against optical fiber length.

$$P_0^S = 21\frac{k_B \times A_{eff}}{g_B(0)L_{eff}} \tag{2.62}$$

where K_B is a factor of either 1 or 2 and refers to the polarization dependence of the pump and Stokes waves. For example, if the pump and Stokes waves have the same polarization, then $K_B = 1$.

Therefore, and under this condition the coupled intensity equations 2.48 and 2.49 should be resolved simultaneously. Hence, one could assume that:

$$\frac{dI_P}{dz} = \frac{dI_S}{dz} \tag{2.63}$$

and therefore:

$$I_P(z) = I_S(z) + C \tag{2.64}$$

where C is the integration constant which is related to the boundary conditions [1]. Hence, Eq. 2.49 can be rewritten as:

$$\frac{dI_S}{I_S(I_S + C)} = -g_B dz \tag{2.65}$$

After integration Eq. 2.65 will be:

$$\int_{I_S(0)}^{I_S(z)} \frac{dI_S}{I_S(I_S + C)} = -\int_0^z g_B dz' \tag{2.66}$$

then:

$$\ln\left\{\frac{I_S(z)[I_S(0) + C]}{I_S(0)[I_S(z) + C]}\right\} = -g_B C z \tag{2.67}$$

In principle, the pump power value $I_P(0)$ is known, therefore the integration constant C can be expressed as $(C = I_P(0) - I_S(0))$. Hence, Eq. 2.67 can be solved algebraically for the Stokes power at any position of the optical fiber (z) as:

$$I_S(z) = \frac{I_S(0)[I_P(0) - I_S(0)]}{I_P(0)\exp\left(g_B z[I_P(0) - I_S(0)]\right) - I_S(0)} \tag{2.68}$$

Referring to Eq. 2.64, the pump power at (z) position of the optical fiber can be written by means of the power conservation law as:

$$I_P(z) = I_S(z) + I_P(0) - I_S(0) \tag{2.69}$$

Now one can find the intensity values for both the pump and Stokes at z, i.e. the spatial distribution in terms of the given boundary values at the input of the optical fiber $I_P(0)$ and $I_S(0)$. Referring to Fig. 2.11, the boundary values $I_P(0)$ and $I_S(L)$ could

be defined physically. Therefore, and by setting ($z = L$) in Eq. 2.68 one can get the unknown value of $I_S(0)$ through predefining the values of $I_P(0)$ and $I_S(L)$. Hence, the Stokes intensity at the position L will be:

$$I_S(L) = \frac{I_P(0)[I_S(0)/I_P(0)][1 - I_S(0)/I_P(0)]}{\exp\left(g_B I_P(0) L[1 - I_S(0)/I_P(0)]\right) - I_S(0)/I_P(0)} \tag{2.70}$$

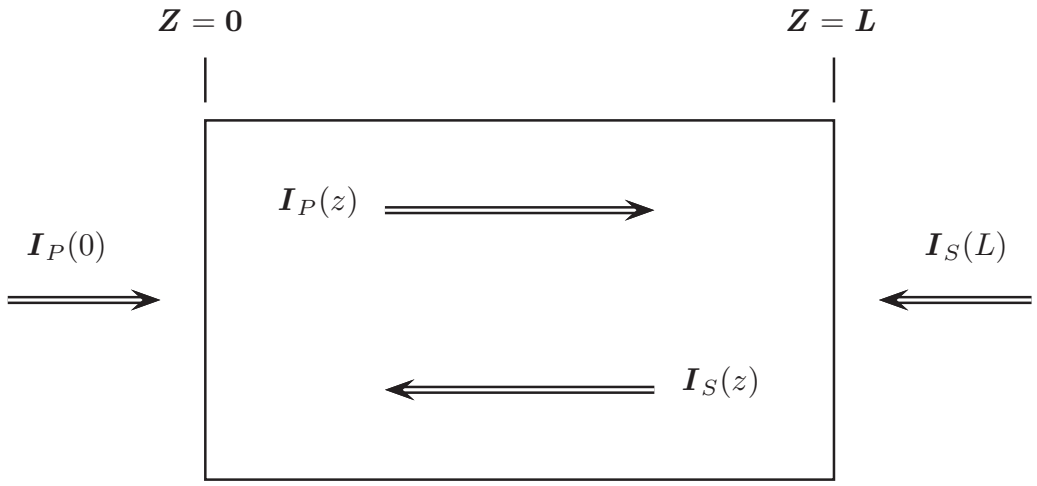

Figure 2.11: SBS process illustration with predefined boundary values of $I_P(0)$ and $I_S(L)$.

2.8 Summary

In order to understand the Brillouin scattering physics, the linear and non-linear effects behavior within an optical medium had been explained with the help of the Maxwell equations. The linear polarization equation as well as the non-linear polarization had been derived.

The Brillouin scattering can be defined as a third order non-linear effect, which exhibits interaction between the optical mode and the acoustic mode. In case of high pump power, there will be a density fluctuation which in turn leads to a time dependent refractive index change within the optical material through the electrostriction effect. Due to the refractive index change, which plays the role of a time variable grating, a part of the pump power will be scattered back which is called Stokes wave.

For telecommunication wavelengths in standard single mode fiber (SSMF), the Stokes wave has a frequency shift of about 11 GHz from the pump wave frequency which is equal to the acoustic frequency. The frequency shift depends on the fiber type and the pump wave characteristics. Since the density modulation of the medium moves with a relative

velocity to the pump and in its direction, the Stokes wave is down shifted in frequency. Therefore, both pump and Stokes waves are counter propagating through the optical medium.

The governing equations for the pump and Stokes waves had been derived in addition to the Brillouin gain parameter. The Brillouin gain coefficient linewidth depends on many factors like: the optical medium characteristics, the temperature as well as the optical fiber core diameter and the spectral width of the pump wave. Usually for a silica optical fiber within room temperature the Brillouin gain coefficient has a natural gain linewidth of about 35 MHz. However, by increasing the pump power the bandwidth decreases.

At a certain pump power level, the scattering starts to be stimulated. Therefore, the Stokes wave growths up exponentially within the optical medium. That specific pump power level is called threshold and governed by the gain coefficient. The Brillouin scattering effect has the lowest non-linear threshold pump power. The threshold pump power level depends mainly on the fiber length, by which it decreases with increasing fiber length. However, it will reach a fixed value after a length that could be defined by the fiber attenuation depending on the fiber effective length behavior. The threshold power level limits the input pump power for a lot of applications. However, one can get rid of this limitation by using a higher bandwidth transmitted signal than the intrinsic Brillouin gain bandwidth and therefore increasing the SBS threshold.

Chapter 3

SBS Gain Enhancement Based on Integrated Silicon Photonics

3.1 Introduction

As explained in the previous chapter, the Stimulated Brillouin Scattering (SBS) is a third-order non-linear optical process by which optical photons are coupled to acoustic phonons, i.e. two optical modes (the pump and the Stokes) are coupled through an elastic mode. The SBS has unique properties, which makes it very attractive for many applications developed in the last few years. For optical telecommunications especially the alteration of the group velocity (Slow- and Fast Light), Quasi Light Storage (QLS) [41], microwave photonics and Ultrahigh-Resolution Spectroscopy (URS) are very important [7, 1, 2]. In principle, in optical fibers the SBS is initiated by electrostriction, which makes the effect rather low and requires kilometers of fiber to be effective and sufficient. However, within the nano-scale this role can be broken down, since tremendous pressure forces can form new SBS non-linearities [18].

In silicon-on-insulator (SOI) based sub-wavelength waveguides a combination of electrostriction and radiation pressure can lead to an enhancement of the SBS effect by several orders of magnitude. Therefore, such type of nano-waveguides based chips have the potential to effectively store optical packets, measure optical spectra with ultrahigh resolution, or can be the building blocks of microwave photonics [42].

In principle, SOI technology refers to the utilization of a layered silicon–insulator–silicon substrate in place of conventional silicon substrates in semiconductor utilization like microelectronics. The main difference between SOI-based devices and conventional silicon-built devices is that the silicon junction is above an electrical insulator. For example, silicon dioxide or sapphire devices which are called silicon on sapphire (SOS). The selection of insulator type depends mainly on the desired application. For example, sapphire being used for high-performance radio frequency (RF) and radiation-sensitive applications. Additionally, silicon dioxide is used for diminished short channel effects in

microelectronics devices [43]. However, the insulating layer and topmost silicon layer also can be different according to the desired application [44].

In RF applications for instance, the development of an SOI fabrication technology using a standard 0.5 μm CMOS node and an enhanced sapphire substrate had been done. The invention of silicon on sapphire (SOS) fabrication is widely used in high-performance RF applications, since its intrinsic benefits of the insulating sapphire substrate which allows high isolation, high linearity and electro-static discharge. Additionally, SOI wafers are mainly used for silicon photonics fabrications. For example, nowadays the crystalline silicon layer on insulator is used for optical nano-waveguides fabrication as well as other passive optical devices for integrated optics. In principle, the crystalline silicon layer is sandwiched between the buried insulator and top cladding of air (or Silicon oxide or any other low refractive index material). Therefore, this enables propagation of electromagnetic waves in the waveguides on the basis of total internal reflection.

Having the fact, that within SBS process two optical modes are coupled through an elastic mode, therefore at a certain beat frequency (simultaneously frequency and phase matched) a dynamic optical force is generated through the interference between the pump and Stokes waves. Hence, a mechanical oscillation takes place in the nano-waveguide. Because of the transverse dimensions of the silicon nano-waveguide, both waves are greatly confined as discrete sets of Eigen-modes. The optical forces inside the nano-waveguide can be divided into two types: electrostriction and radiation forces and each type has two kinds: bulk and boundary forces.

This chapter is organized as follows: the silicon crystalline structure as well as the silicon lattice structure will be explained. The two-photon absorption non-linearity will be presented in order to calculate the maximum launchable input pump power for the SOI waveguide. Two kinds of forces: electrostriction and radiation will be studied. For each force two types will be investigated: body and pressure.
The Brillouin gain and the predicted Stokes wave power will be calculated in terms of the opto-mechanical forces and the elastic waveguide deformation. Two kinds of waveguides will be studied: strip and rib, each two structures will be investigated. Simulation results will be presented for rectangular SOI based strip and rib nano-waveguides, showing the very high potential of this new approach.

3.2 Silicon Crystalline Structure

3.2.1 Silicon Lattice

Silicon has a cubic crystalline centro-symmetric structure. In general, the crystals eventually terminate at a surface since they are not infinitely large. Semiconductor devices are fabricated at or near a surface; therefore the surface properties give an indication about the device characteristics. It is interesting to describe these surfaces in terms of the lattice. Assuming a general three dimensional unit cell shown in Fig. 3.1 with wave vectors a, b and c.

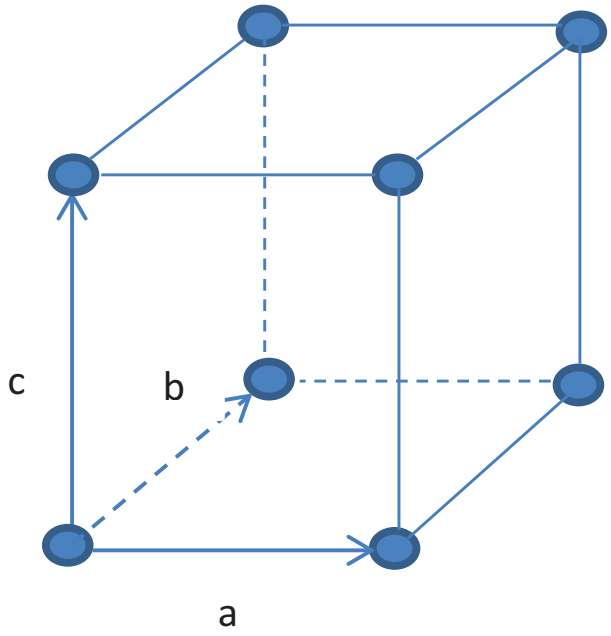

Figure 3.1: Arbitrary three dimensional unit cell.

In principle, the wave vectors are referring to the relation between the unit cell and the lattice. Each lattice point can be found using the following relation:

$$m = pa + qb + sc \tag{3.1}$$

where p, q and s are integers, therefore the magnitudes of the vectors a, b and c refer to the lattice constants of the unit cell. By considering the intersects of the planes along a, b and c axes of the lattice, the planes or surfaces through the crystal can be defined.

In a cubic crystal like silicon, three planes can be considered to be an indication for the material itself. The blue plane in Fig. 3.2 is parallel to a and c axes, in such the intercepts (m) are given by:

$$\begin{aligned} p &= \infty \\ q &= 1 \\ s &= \infty \end{aligned} \tag{3.2}$$

Miller indices of (0, 1, 0) can be obtained by taking the reciprocal of (m) [45]. Therefore, the plane in Fig. 3.2 is denoted as (010) plane. Any plane parallel to that plane and separated by integral number of the lattice constants is referred to be as (010). In the same manner, the plane in which it is parallel to b and c is referred as (100) and the

plane parallel to a and b is referred as (001). Since, all the planes in silicon lattice are equivalent, sometimes they are grouped to be referred as (100).

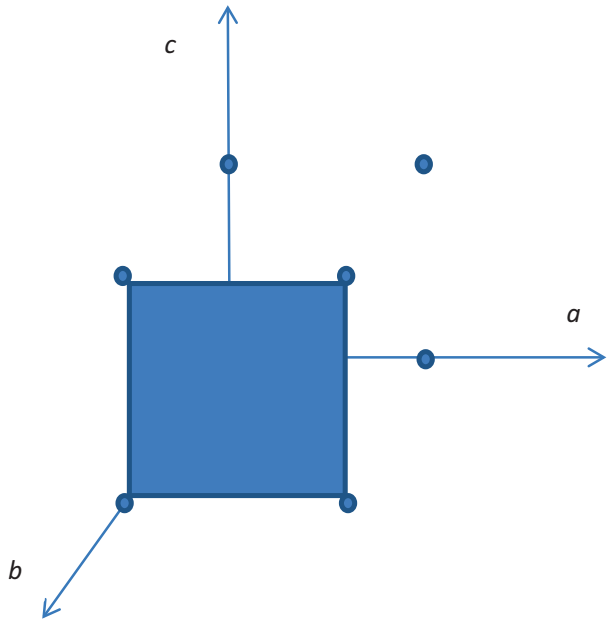

Figure 3.2: Silicon unite cell with lattice plane (010).

3.2.2 Silicon Photo-Elastic Tensor

For isotropic materials like amorphous glasses and for cubic crystals like silicon, the electrostrictive tensor is given by [46, 47]:

$$< \sigma_{ij}^{es} >= -\frac{1}{2}\varepsilon_0 n^4 \left[p_{ijkl}\right] < E_k E_l > \tag{3.3}$$

where n=3.47 is the silicon refractive index [48], p_{ijkl} is the photo-elastic (stiffness) tensor [49], ε_0 is the permittivity of vacuum and $E_k E_l$ are the electric field components in k and l directions, respectively. According to Hooke's Law [49], the electric field (E_{kl}) can be considered as a stress and the photo-elastic tensor (p_{ijkl}) as a strain. Whereas, (p_{ijkl}) expresses the linear relation between the second rank tensors (E_{kl}) and (σ_{ij}). The photo-elastic coefficient p_{ijkl} is a tensor of rank four, hence (p) for a pair (ij) can be

written as [49]:

$$p_{ij} = \begin{bmatrix} p_{11} & p_{12} & p_{13} & p_{14} & p_{15} & p_{16} \\ p_{21} & p_{22} & p_{23} & p_{24} & p_{25} & p_{26} \\ p_{31} & p_{32} & p_{33} & p_{34} & p_{35} & p_{36} \\ p_{41} & p_{42} & p_{43} & p_{44} & p_{45} & p_{46} \\ p_{51} & p_{52} & p_{53} & p_{54} & p_{55} & p_{56} \\ p_{61} & p_{62} & p_{63} & p_{64} & p_{65} & p_{66} \end{bmatrix} \tag{3.4}$$

Since the tensors E_{kl} and σ_{ij} are symmetric, the photo-elastic coefficients are unaffected when either the first two or the last two indices are interchanged, Hence:

$$\begin{aligned} p_{ijkl} &= p_{jikl} \\ p_{ijkl} &= p_{ijlk} \end{aligned} \tag{3.5}$$

According to that symmetry, p_{ijkl} is symmetric about its main diagonal and therefore, Eq. 3.4 can be rewritten as:

$$p_{ij} = \begin{bmatrix} p_{11} & p_{12} & p_{13} & p_{14} & p_{15} & p_{16} \\ p_{12} & p_{22} & p_{23} & p_{24} & p_{25} & p_{26} \\ p_{13} & p_{23} & p_{33} & p_{34} & p_{35} & p_{36} \\ p_{14} & p_{24} & p_{34} & p_{44} & p_{45} & p_{46} \\ p_{15} & p_{25} & p_{35} & p_{45} & p_{55} & p_{56} \\ p_{16} & p_{26} & p_{36} & p_{46} & p_{56} & p_{66} \end{bmatrix} \tag{3.6}$$

Since, silicon has a cubic crystalline symmetric structure and according to the earlier silicon lattice description by which silicon is symmetric with respect to x=0, y=0 and z=0, thus p_{ij} is zero if it contains odd number of certain components. Therefore, p_{ij} can be rewritten as:

$$p_{ij} = \begin{bmatrix} p_{11} & p_{12} & p_{13} & 0 & 0 & 0 \\ p_{12} & p_{22} & p_{23} & 0 & 0 & 0 \\ p_{13} & p_{23} & p_{33} & 0 & 0 & 0 \\ 0 & 0 & 0 & p_{44} & 0 & 0 \\ 0 & 0 & 0 & 0 & p_{55} & 0 \\ 0 & 0 & 0 & 0 & 0 & p_{66} \end{bmatrix} \tag{3.7}$$

Referring to the silicon parameters as: refractive index $n = 3.47$, Young's modulus E = 170×10^9 Pa and Poisson's ration $\nu = 0.28$. The photo-elastic coefficients would

be: $p_{11} = p_{22} = p_{33} = -0.09$, $p_{12} = p_{13} = p_{21} = p_{23} = p_{31} = p_{32} = 0.017$ and $p_{44} = p_{55} = p_{66} = -0.051$ [49]. These parameters had been used to achieve the simulation results, presented in the next sections.

3.3 Two-Photon Absorption (TPA) in Silicon

Due to the high index contrast between the silicon core and silica cladding, silicon waveguides allow strong optical confinement and large effective non-linearity. Therefore, it facilitates low cost chip-scale demonstration of all-optical non-linear functional devices at low pump powers.

In SOI waveguides the non-linear Kerr parameter can scale up to $7{\times}10^3$ ($W^{-1}{*}m^{-1}$) [50]. Hence, it is about three orders of magnitude higher than the non-linearity in highly non-linear optical fibers. Additionally, within SOI waveguides there are a variety of optical non-linear effects since they are generated from the interaction of the optical field with phonons and electrons.

Two-Photon Absorption (TPA) is a third order non-linear process. It is one of the most effective non-linear effects in SOI waveguides, by which it is dominated in high optical intensities. Additionally, it can be assumed as a fundamental limitation for the SOI devices. Silicon has an indirect band gap of 1.12 eV. Therefore, a single photon is not enough to excite an electron from the Valence band (Vb) to the Conduction band (Cb) as illustrated in Fig. 3.3.

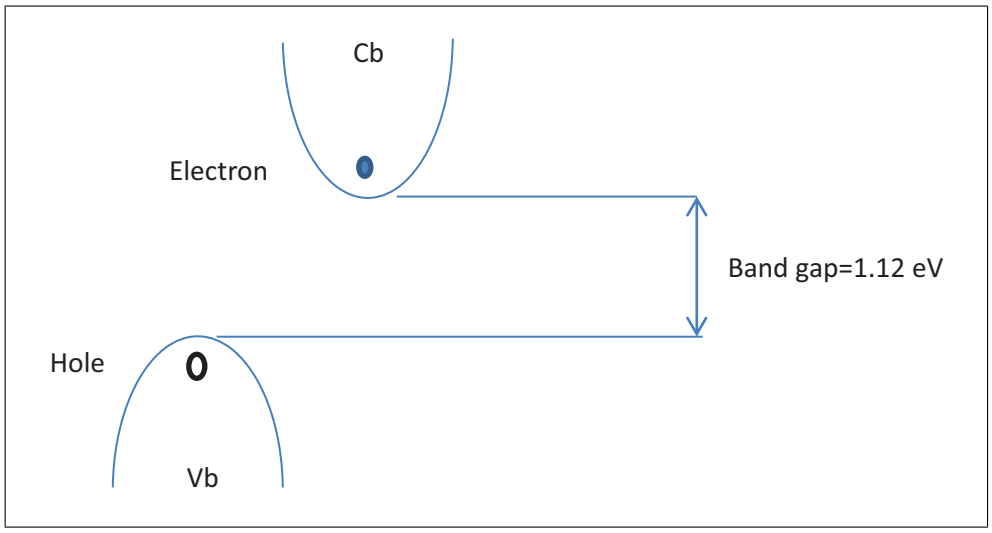

Figure 3.3: Indirect band gap illustration of silicon.

In principle, TPA involves the simultaneous absorption of two photons during the excitation of one electron from Vb to Cb. Since silicon has an indirect bad gap of 1.12 eV, the sum of the energies of the two absorbed phonons should exceed 1.12 eV.

TPA excitations are absorbing, since energetically they correspond to an excitation of an electron from the Vb to the Cb. Therefore, TPA generates free carriers in the Cb in which they act as sources for Free Carrier Absorption (FCA) and Free Carrier Index (FCI). Thus, the long lifetime of the free carriers in the Cb leads to long-lasting FCA and FCI effects. The results is a speed down of SOI devices. The TPA loss is governed by the following intensity dependent relation:

$$\frac{dI}{dx} = -\beta I^2 \tag{3.8}$$

where x is the propagation direction, β is the TPA coefficient and I is the optical intensity in the waveguide. One can use the Drude model to describe the TPA-induced free carrier absorption loss as [51]:

$$\Delta_{\alpha FCA} \cong 6.04e^{-18}\lambda_p^2 \beta I^2 (\tau_{eff}/2E_p) \tag{3.9}$$

where λ_p denotes the pump wavelength in nm, τ_{eff} is the effective carrier lifetime (carrier lifetime is the average time it takes for a minority carrier to recombine) and E_p is the photon energy. The TPA parameter (β) was measured by many groups and it is varying between 0.4 to 1.5 cm/GW [52]. If the two photons have the same frequency, then this is referred as degenerate TPA (two photons from the Pump or the Stokes wave). Non-degenerate TPA takes place when the two photons have different frequencies (one photon from the pump and one from the Stokes wave). According to [53], the TPA threshold input power for the same SOI waveguide type and dimensions that was in the simulations here is 30 mW.

Many methods can be found in the literature to reduce the effect of the FCA, such as:

1. Operation at low pump power.
2. Increase the device length.
3. Using a pulsed pump power laser.
4. Sweeping out the free carriers from the optical mode using a transverse p-n junction structure.

3.4 Electrostriction Forces

The forces are generated through the SBS process by the interaction of the Pump wave ($E_p e^{i(k_p x - \omega_p t)}$) and the Stokes wave ($E_s e^{i(-k_s x - \omega_s t)}$), this results in a beat wave with a frequency ($\Omega = \omega_p - \omega_s$) and a wave vector ($k_A = k_P - k_S$), as described in the previous chapter. In principle, the maximum SBS gain value is determined by the elastic

wave damping [18]. At resonance, the peak elastic displacement velocity is proportional to the phononic quality factor (Q) and the optical force value. Therefore, within simulations and depending on the silicon damping limit for the frequency range of interest [54], one can assume a frequency-independent quality factor of Q=1000 as a phononic property (energy loss in the resonator) for all elastic modes, where [49, 55, 56]:

$$Q = 2\pi \frac{\texttt{maximum energy stored during a period of oscillation}}{\texttt{energy lost during a period of oscillation}} \tag{3.10}$$

The pump and Stokes waves can be launched in the same direction for forward SBS (FSBS) and in opposite direction for backward SBS (BSBS). In FSBS, the generated forces excite standing-wave elastic modes, while in BSBS traveling-wave elastic modes are excited. The high optical intensity in the waveguide leads to a compression of the material in that region, so that an electrostriction force is generated in the bulk, while the electrostriction pressure is generated from the discontinuities of the optical intensities and photo-elastic coefficients at the boundaries. The parametric conversion between the pump and Stokes waves is described by Eq. 2.56. Instead, here we used x rather than z.

Although, the Brillouin gain g_B can be calculated from Eq. 2.50 in terms of values of the maximum gain $\Omega_B(0)$, frequency shift $\Delta\Omega$ and linewidth $\Delta\Omega_B$. One can get the Brillouin gain g_B from the following relation [16]:

$$g_B = 2\left(\frac{\omega_s}{\Omega}\right)\int_{wg} Re\left[\widetilde{f}_n(x,y)\widetilde{u}_n(x,y)\right] dA \tag{3.11}$$

where $\widetilde{f}_n$ are the total optical forces, $\widetilde{u}_n$ is the elastic Eigen mode deformation and $\widetilde{f}_n(x,y)\widetilde{u}_n(x,y)$ is the overlap integral between the forces and the elastic deformation. For the bulk forces the integration is taken over the waveguide cross section while for the pressure forces it is taken over the boundaries.

In principle, the electrostriction forces can be derived from the electrostriction tensor. Therefore, the total electric field of the waveguide system will be substituted in Eq. 3.3. The total electric field within the waveguide system is:

$$E = \frac{E_p e^{i(k_p x - \omega_p t)} + E_s e^{i(-k_s x - \omega_s t)}}{2} + C.C. \tag{3.12}$$

then Eq. 3.3 can be rewritten as:

$$< \sigma_{ij}^{es} >= -\frac{1}{4}\varepsilon_0 n^4 \left[p_{ijkl}\right]\left(E_{pk}E_{sl}^* + E_{pl}E_{sk}^*\right) \tag{3.13}$$

where E_p is the electric field of the Pump wave and E_s that of the Stokes component. In principle, within integrated photonics fabrication most waveguide structures are aligned with the material principal axes. Hence, one can use the symmetry of the cubic crystalline lattice of the silicon with respect to planes: $x = 0$, $y = 0$ and $z = 0$ [47]. Therefore, Eq. 3.13 and referring to 3.7 can be written in the contracted notation [57]:

$$\begin{bmatrix} \sigma_{xx} \\ \sigma_{yy} \\ \sigma_{zz} \\ \sigma_{yz} \\ \sigma_{xz} \\ \sigma_{xy} \end{bmatrix} = -\frac{1}{4}\varepsilon_0 n^4 \begin{bmatrix} p_0 & p_S & p_S & 0 & 0 & 0 \\ p_S & p_0 & p_S & 0 & 0 & 0 \\ p_S & p_S & p_0 & 0 & 0 & 0 \\ 0 & 0 & 0 & p_R & 0 & 0 \\ 0 & 0 & 0 & 0 & p_R & 0 \\ 0 & 0 & 0 & 0 & 0 & p_R \end{bmatrix} \begin{bmatrix} E_{px}E_{sx}^* \\ E_{py}E_{sy}^* \\ E_{pz}E_{sz}^* \\ E_{py}E_{sz}^* + E_{pz}E_{sy}^* \\ E_{px}E_{sz}^* + E_{pz}E_{sx}^* \\ E_{px}E_{sy}^* + E_{py}E_{sx}^* \end{bmatrix} \tag{3.14}$$

As mentioned earlier, assuming [100], [010] and [001] symmetry direction of the crystalline silicon coincide with x, y and z, respectively. Therefore, under this orientation the photo-elastic coefficients will be: $p_{11} = p_{22} = p_{33} = p_0 = -0.09$, $p_{12} = p_{13} = p_{21} = p_{23} = p_{31} = p_{32} = p_S = 0.017$ and $p_{44} = p_{55} = p_{66} = p_R = -0.051$. Hence, the body force of the electrostriction effect can be found from the divergence electrostriction tensor as [16]:

$$f_x^{es} = -ik_A\sigma_{xx} - \sigma_y\sigma_{xy} - \sigma_z\sigma_{xz} \tag{3.15a}$$
$$f_y^{es} = -ik_A\sigma_{xy} - \sigma_y\sigma_{yy} - \sigma_z\sigma_{yz} \tag{3.15b}$$
$$f_z^{es} = -ik_A\sigma_{xz} - \sigma_y\sigma_{zy} - \sigma_z\sigma_{xz} \tag{3.15c}$$

The electrostrictive pressure force on the interface between the silicon and the cladding can be calculated as follows:

$$f_i^{es} = \sigma_{1ij} - \sigma_{2ij} \tag{3.16}$$

where σ_{1ij} is the photo-elastic coefficient of air and is about zero, and σ_{2ij} is the photo-elastic coefficient for the silicon. Therefore the force will point inward.

For FSBS $E_p \approx E_s \approx E$, since the phase shift between the pump and Stokes waves is small compared to the frequency of the pump wave. Additionally, the propagation is in the x-direction, whereas E_x is imaginary and E_y, E_z are real. Therefore, Eq. 3.14 can

be rewritten as:

$$\begin{bmatrix}\sigma_{xx}\\ \sigma_{yy}\\ \sigma_{zz}\\ \sigma_{yz}\\ \sigma_{xz}\\ \sigma_{xy}\end{bmatrix} = -\frac{1}{4}\varepsilon_0 n^4 \begin{bmatrix} p_0 & p_S & p_S & 0 & 0 & 0\\ p_S & p_0 & p_S & 0 & 0 & 0\\ p_S & p_S & p_0 & 0 & 0 & 0\\ 0 & 0 & 0 & p_R & 0 & 0\\ 0 & 0 & 0 & 0 & p_R & 0\\ 0 & 0 & 0 & 0 & 0 & p_R \end{bmatrix} \begin{bmatrix} |E_x|^2\\ |E_y|^2\\ |E_z|^2\\ 2Re(E_yE_z)\\ 0\\ 0 \end{bmatrix} \tag{3.17}$$

Therefore, Eq. 3.15 will be rewritten as:

$$f_x^{es} = 0 \tag{3.18a}$$
$$f_y^{es} = \sigma_y\sigma_{yy} - \sigma_z\sigma_{yz} \tag{3.18b}$$
$$f_z^{es} = \sigma_y\sigma_{zy} - \sigma_z\sigma_{xz} \tag{3.18c}$$

Within BSBS $k_A = 2k_p$ and $E_p = E$, $E_s = E^*$, therefore Eq. 3.14 can be expressed as:

$$\begin{bmatrix}\sigma_{xx}\\ \sigma_{yy}\\ \sigma_{zz}\\ \sigma_{yz}\\ \sigma_{xz}\\ \sigma_{xy}\end{bmatrix} = -\frac{1}{4}\varepsilon_0 n^4 \begin{bmatrix} p_0 & p_S & p_S & 0 & 0 & 0\\ p_S & p_0 & p_S & 0 & 0 & 0\\ p_S & p_S & p_0 & 0 & 0 & 0\\ 0 & 0 & 0 & p_R & 0 & 0\\ 0 & 0 & 0 & 0 & p_R & 0\\ 0 & 0 & 0 & 0 & 0 & p_R \end{bmatrix} \begin{bmatrix} E_x^2\\ E_y^2\\ E_z^2\\ 2E_yE_z\\ 2E_xE_z\\ 2E_xE_y \end{bmatrix} \tag{3.19}$$

Additionally, it can be shown that the electrostrictive body force is both transverse and longitudinal since Eq. 3.15 has a non-zero component.

3.5 Radiation Forces

In principle, both body and radiation pressure forces can be derived from Maxwells Stress Tensor (MST) which is [58]:

$$T_{ij} = \varepsilon_0\varepsilon(x,y)\left[E_iE_j - \frac{1}{2}\delta_{ij}|E|^2\right] + \mu_0\mu\left[H_iH_j - \frac{1}{2}\delta_{ij}|H|^2\right] \tag{3.20}$$

where ε_0 and ε are the vacuum dielectric and relative dielectric permittivity, μ_0 and μ are

vacuum magnetic and relative magnetic permeability, respectively. While, δ_{ij} is a short segment of the waveguide and E, H are the electric and magnetic field components. The radiation body force is the divergence of the MST in which it is longitudinal because of the x component of the electric field and transverse due to the y and z components of the electric field, for both FSBS and BSBS. The radiation pressure between the interface of air and silicon is given by [16]:

$$f_i^{rp} = T_{2ij} - T_{1ij} \tag{3.21}$$

where T_{2ij} and T_{1ij} are MST for silicon and clad respectively. Therefore, in the case of air clad, the pressure is outward and the force is transverse in both FSBS and BSBS since $T_{1ij} = 0$.

Now, after the calculation of the four forces, the SBS gain can be calculated from Eq. 3.11 through the overlap integral between the optical forces and the elastic Eigen mode deformations. The total Brillouin gain coefficients can be calculated as follows:

$$G_{B(total)} = \left(\sqrt{G_{es}} \mp \sqrt{G_{rp}}\right)^2 \tag{3.22}$$

where G_{es} is the SBS gain coefficient related to the electrostriction force and G_{rp} is the SBS gain coefficient related to the radiation pressure force. Additionally, the $(\mp)$ sign means that the electrostriction force and the radiation pressure -induced gain are add up either constructively or destructively.

Usually for optical fibers the Brillouin gain coefficient is developed in terms of light intensity. Therefore, the gain coefficient has units of (m/W). This is actually ascribed to the intrinsic response of the material which is only a reasonable approximation when the light spot size is > 2 μm. Whereas, when studying waveguides it makes more sense to formulate a gain coefficient in terms of the power carried by the waveguide mode. In this case the mode area is incorporated into the gain giving units of 1/(m.W).

3.6 Simulation Method

For the simulation of different structures the multi physics simulation software Comsol 3.4b was used. It is based on advanced numerical methods, for modeling and simulating physics-based problems. Figures 3.4 and 3.5 show the SOI waveguides with dimensions that were used in the simulation software. Fig. 3.4 shows the strip waveguide by which the core is modeled from Silicon with a width of 450 nm, height of 220 nm and length of 2μm. The substrate underneath the core is modeled from Silica (SiO2) with a width of 2μm, height of 1 μm and length of 2 μm. The overall simulation domains for both strip and rib waveguides were as a cubic of 2 μm dimensions, i.e. the core centered above the substrate with the dimensions mentioned above and the rest of the simulation domain

modeled as a clad from either air or silica.

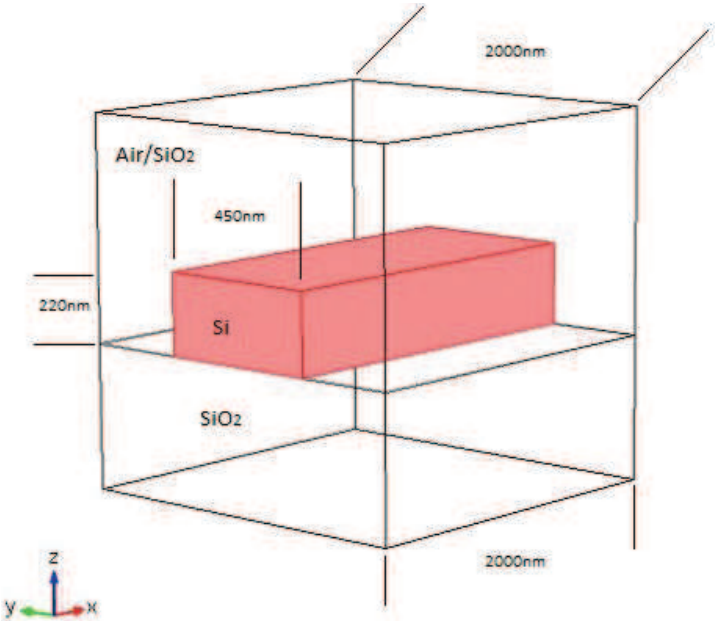

Figure 3.4: Strip SOI Waveguide: Air/SiO2 refers to either Air or Silica used as a clad for the simulations.

The next procedures were followed for both strip and rib waveguides:

1. The "Electromagnetic Module" of the Comsol software was used to simulate the TE-like optical mode by which two numerical ports were used: the first was applied to the front face of the waveguide and switched on (Pump Port) and the second port was applied to the back face and switched off (Listening Port). "Boundary Mode Analysis" study was used to calculate the effective mode index and "Frequency Domain" study was used to achieve the TE-like mode, the wavelength of the optical pump was chosen as 1550 nm. The figures 3.6 and 3.15 show the TE-like mode of the strip and rib waveguides, respectively. The electrostriction body forces were calculated for FSBS and BSBS, via Eq. 3.17 and Eq. 3.19, respectively. While the electrostriction pressure forces were calculated via Eq. 3.16. The radiation body forces were calculated via Eq. 3.20 while the radiation pressure forces were calculated via Eq. 3.21.

2. The "Elastic Wave Module" (EWM) was used to generate the elastic waves inside the SOI waveguides. The symmetric boundary condition: "Floquet Periodicity" (FP) was used to initiate the acoustic wave through the SOI waveguides, the Floquet boundary condition was applied to both front and back faces of the waveguides, in which it is modeled through the substitution of the acoustic wave vectors for FSBS and BSBS. Additionally, the "Eigen Frequency Study" (EFS) was used to calculate the elastic-Eigen frequencies. In principle, 13 Eigen frequencies were

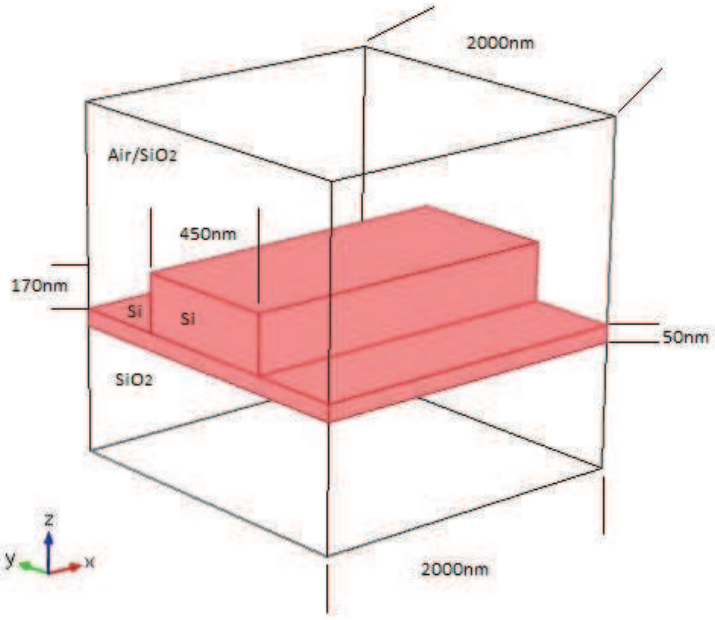

Figure 3.5: Rib SOI Waveguide: Air/SiO2 refers to either Air or Silica used as a clad in the simulations.

achieved by searching around 13 GHz for 13 Eigen frequencies: as a number of frequencies. Additionally, the quality factor ($Q = 1000$) was used for all the elastic Eigen-modes [47].

3. The "MATLAB Life Link Module" was used as a client with COMSOL server to simulate the SBS gain coefficients via Eq. 3.11. The gain profiles had been plotted versus the achieved Eigen frequencies.

3.7 220x450 nm Silicon Waveguide

First a silicon waveguide with a length of 2 μm, a height of 220 nm and a width of 450 nm had been simulated. Two kinds of waveguides were simulated (strip and rib waveguides) and for each kind two cases were investigated, silicon core on silica substrate with air cladding and silicon core on silica substrate with silica cladding. The refractive index of silicon for 1550 nm wavelength was chosen as n=3.47 and for silica as n=1.45.

A strip waveguide is a rectangular waveguide in which the core is made from silicon and the substrate from silica, the core is based directly on the substrate without a slab as shown in Fig. 3.4. The clad is made from either air or silica. Whereas, a rib waveguide is just like the strip waveguide but it consists of a slab of 50 nm between the silicon core and the substrate and this slab is made of silicon. Therefore, the core height will be 220 nm as shown in Fig. 3.5. The bold red interfaces refer to the separations between materials.

In principle, the aim of the simulations was to calculate the stimulated Brillouin scattering gain coefficients for both forward and backward scattering. Therefore, the SBS gain coefficient was calculated via an overlap integral between the optical forces and the elastic Eigen-mode deformations, by which they are simulated using the EWM in multiphysics Comsol 4.3b.

The periodic boundary condition named Floquet boundary condition, was applied to generate the acoustic wave inside the waveguide, the acoustic wave vector was chosen equal to zero for FSBS and double the pump wave vector for BSBS, as described earlier. Three values of pump power were chosen (table 3.1 on page 70) and for each value: the FSBS and BSBS gain coefficients, power inside waveguide and the (expected) Stokes power were calculated. The next figures have been captured choosing 100 mW input pump power (before the TPA was toking into account), the wavelength of the pump wave was chosen as 1550 nm. The expected Stokes power was calculated from the following relation:

$$P_S = (P_{S0})e^{Lg_B P_P} \tag{3.23}$$

where P_{S0} is the noise floor (-30 dBm), L is the waveguide length, g_B is the simulated SBS gain coefficient and P_P is the pump power. Additionally, the power inside the SOI waveguide was calculated using the following relation from the software:

$$P = \int c\varepsilon_0 n_{eff} E^2 dA \tag{3.24}$$

where $n_{eff} = \beta/k_0$ is the effective refractive index calculated by the software, β is the propagation constant, $k_0 = 2\pi/\lambda_0$ is the wave number, c is the speed of light in vacuum, ε_0 is the permittivity of vacuum and E is the electric field. The integration had been taken over the waveguide cross section area where the input power was launched.

3.8 Simulation Results

3.8.1 Strip: Air Cladding Waveguide

Fig. 3.6 shows the fundamental optical mode (normalized electric field to unity) inside the strip waveguide with air clad and silica substrate. It can be seen that the electric field is concentrated at the center of the waveguide with a small part of an evanescent field outside the core; this is because of the high index contrast between Silicon and air according to total internal reflection. Therefore, the regions surrounding the core carry very low field intensity.

The SBS gain coefficients had been plotted versus the elastic Eigen frequency using Eq. 3.11. In principle, the elastic Eigen frequencies the software is searching for are the

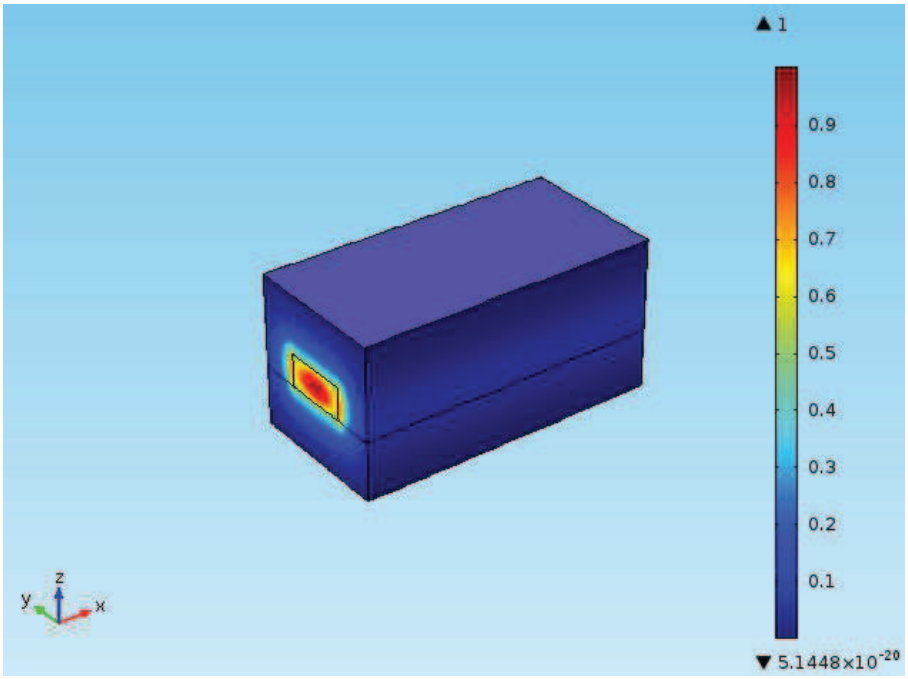

Figure 3.6: Normalized electric field of a strip SOI waveguide with air cladding.

frequency shifts from the pump wave frequency. In Fig. 3.7 and the following the red line corresponds to the SBS contribution by electrostriction (ES), the green line represents the radiation pressure (RP) contribution and the blue line depicts the total SBS gain in the waveguide as the superposition of all contributions.

Fig. 3.7 shows the gain profile of the excited Elastic Eigen modes for the FSBS of the strip SOI waveguide with air cladding. As can be seen, there are two excited Elastic Eigen modes at 12.885 and 12.988 GHz with SBS gain contributions of $0.055\text{x}10^4$ $(\text{m.W})^{-1}$ and $0.13\text{x}10^4$ $(\text{m.W})^{-1}$, respectively. In these modes the electrostriction and radiation forces interfere constructively, while at 12.899 GHz both forces add up destructively. Therefore, the total gain coefficient is approximately zero.

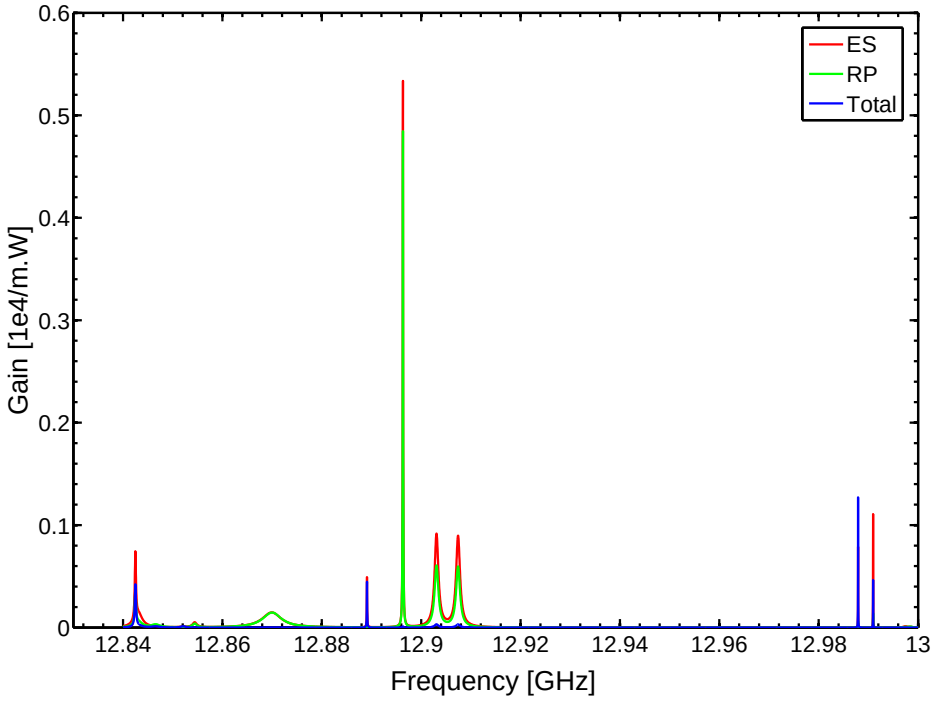

Figure 3.7: FSBS gain profile of a strip waveguide with air cladding.

Fig. 3.8 shows the excited Elastic Eigen-mode at 12.988 GHz for FSBS. As can be seen, the normalized deformation of the waveguide in y and z directions are much higher than in x direction, since the transverse behavior of both forces is the dominant.

Fig. 3.9 shows the SBS gain profile of the excited Elastic Eigen modes of the BSBS of the strip SOI waveguide with air cladding. Here, more than two excited modes can be found by which the forces add up constructively. Nevertheless, modes with destructive interference can be seen also. For example, at 13.07 GHz the gain related to electrostriction force is 0.03×10^4 $(\mathrm{m.W})^{-1}$ while the gain related to radiation force is 0.02×10^4 $(\mathrm{m.W})^{-1}$ and the destructive interference results in a total gain of 0.005×10^4 $(\mathrm{m.W})^{-1}$. Additionally, at 12.9 GHz the total gain of 0.15×10^4 $(\mathrm{m.W})^{-1}$ is a result of constructive interference between the gain contribution of electrostriction and radiation pressure.
Comparing Figures 3.7 and 3.9, in Fig. 3.7 only two constructive interferences result in total gain distributions of 0.12×10^4 and 0.05×10^4 $(\mathrm{m.W})^{-1}$, while in Fig. 3.9 more constructive interferences result in total gain distributions of 0.15×10^4, 0.07×10^4, 0.025×10^4 $(\mathrm{m.W})^{-1}$ and 0.2×10^4 $(\mathrm{m.W})^{-1}$.

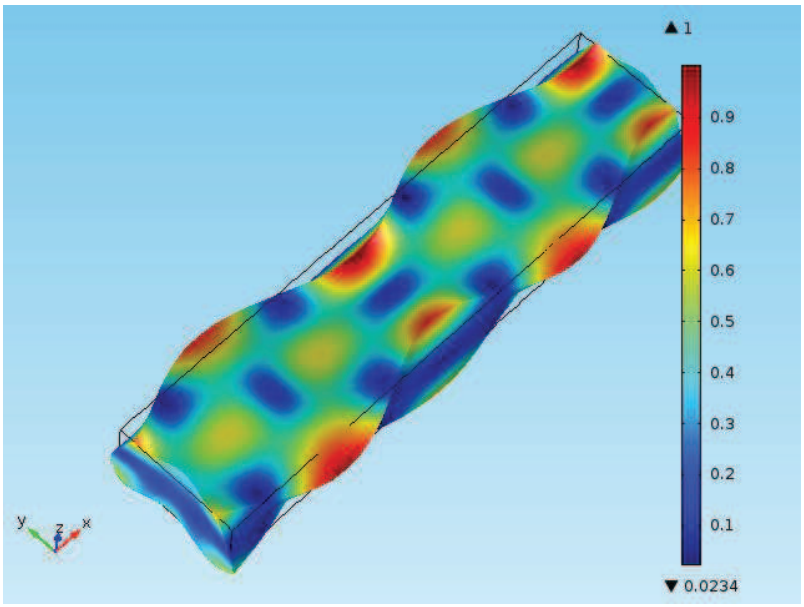

Figure 3.8: Elastic mode for the gain at 12.988 GHz on the FSBS for a strip waveguide with air cladding, the right bar shows the normalized displacement.

Fig. 3.10 shows the normalized excited Elastic Eigen mode for the gain at 13.039 GHz, a top view (left) and a bottom view (right). It can be seen that the y and z com-

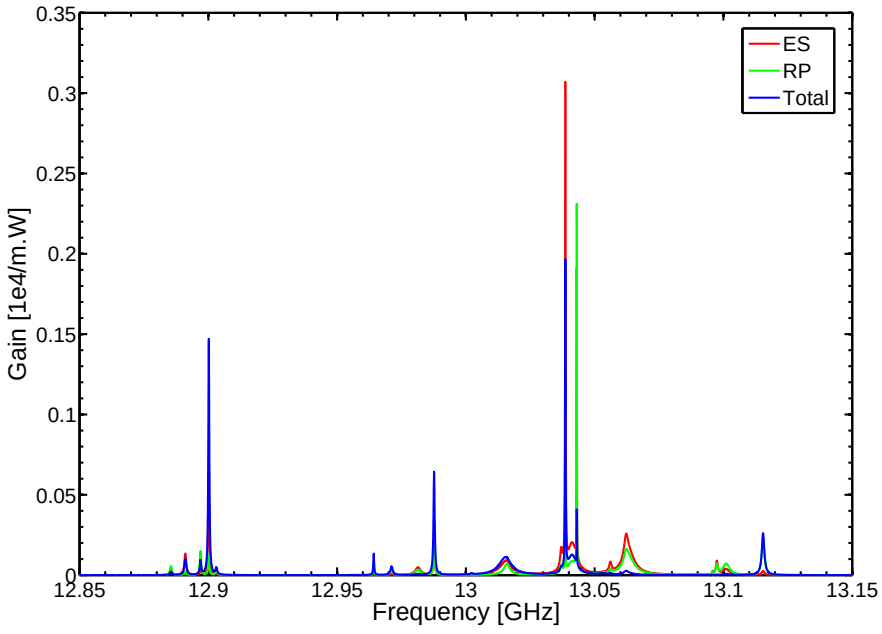

Figure 3.9: BSBS gain profile of a strip waveguide with air cladding.

ponents of the deformation are greater than the x component, therefore the forces are mostly transverse rather than longitudinal. Additionally, one can see from the bottom view of Fig. 3.10 that the guided elastic modes are propagated to the silica substrate due to the boundary forces of the waveguide core. Therefore, the displacement in the waveguide core leads to a displacement in the substrate as well [59].

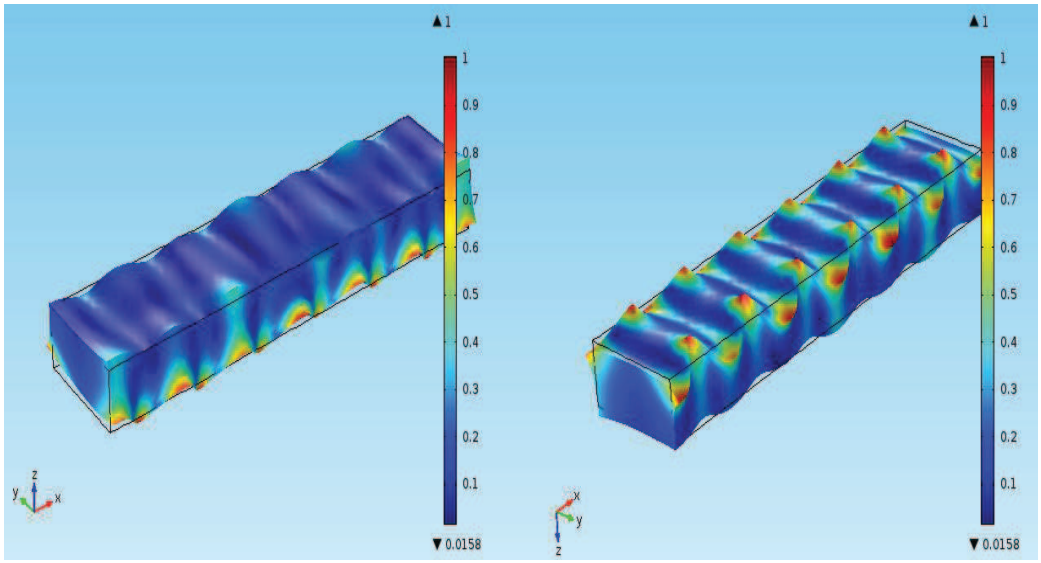

Figure 3.10: Elastic mode for the gain at 13.039 GHz in the FSBS of a strip waveguide with air cladding.

3.8.2 Strip Waveguide with Silica Cladding

For the next simulation instead of air, silica (SiO2) was chosen to cover the silicon core of the strip waveguide. In Fig. 3.11 it can be seen that there is only one constructive interference which results in a total gain distribution (blue) of 0.09×10^4 $(\text{m.W})^{-1}$ at 12.989 GHz. Whereas, the other gain contributions are destructive. For example, at 12.899 GHz both electrostriction and radiation pressure gain contributions were about 0.49×10^4 $(\text{m.W})^{-1}$ but they add up destructively and result in a total gain of zero.

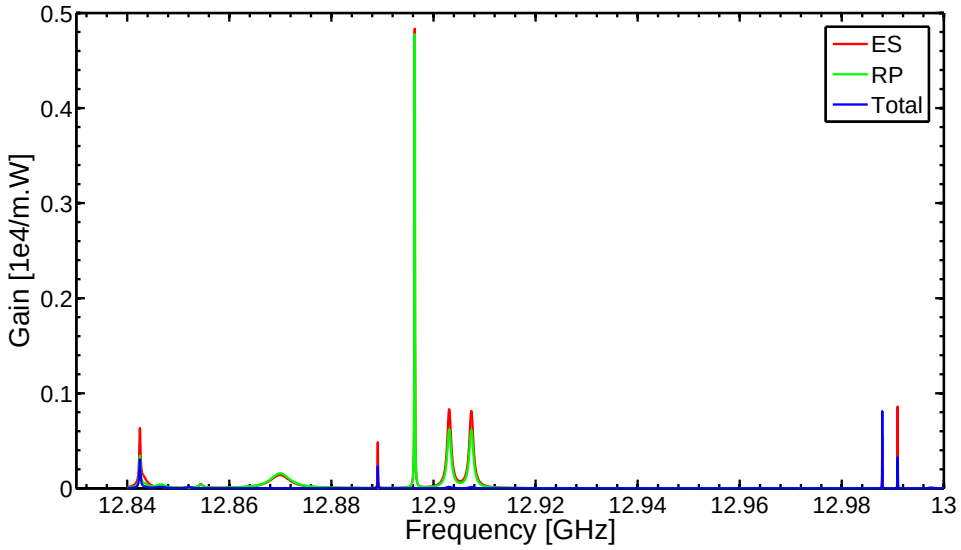

Figure 3.11: FSBS gain profile of a strip waveguide with silica cladding.

Fig. 3.12 shows the normalized elastic deformation of the gain at 12.988 GHz for FSBS, the oscillation takes place mainly in y and z at the button side of the core, i.e. the dominant force is transverse.

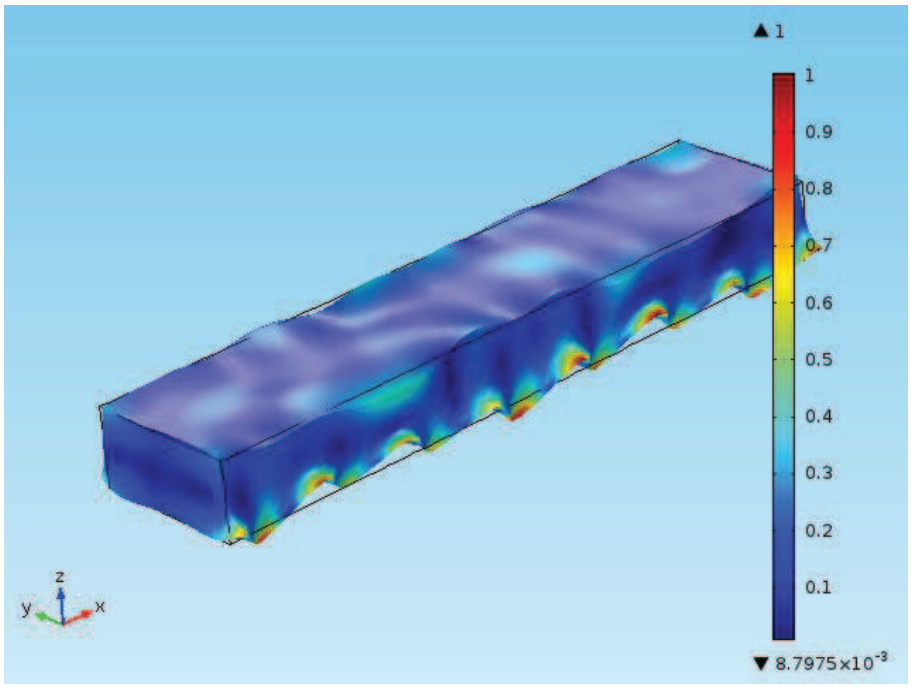

Figure 3.12: Elastic mode for the gain at 12.988 GHz in FSBS of a strip waveguide with silica cladding.

Fig. 3.13 shows the gain profile of the excited elastic Eigen modes for the BSBS in the strip SOI waveguide. It can be seen that there are five excited elastic modes at (12.9, 12.965, 12.97, 12.89, and 13.125 GHz) by which the total gain result from constructive interference.

Additionally, the gain of the elastic Eigen modes at 13.039 and 13.041 GHz result from a destructive interference, since the opposite directions for displacement of the radiation pressure and electrostriction. Although the gain contribution from radiation pressure at 13.041 GHz was about 0.25×10^4 $(\text{m.W})^{-1}$, it destructively add up with the electrostriction and results in a total gain of only 0.03×10^4 $(\text{m.W})^{-1}$.

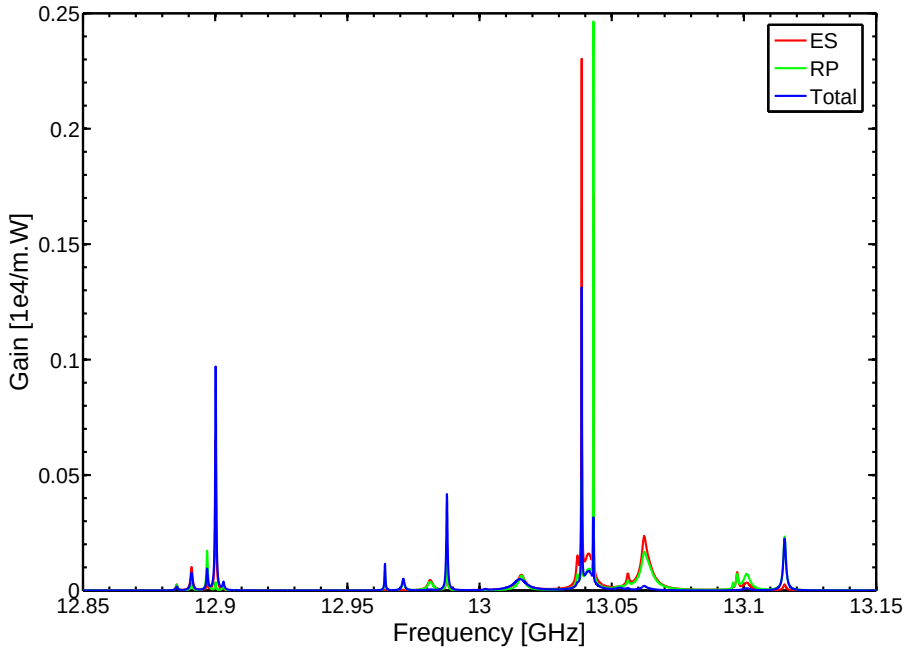

Figure 3.13: BSBS gain profile of a strip SOI waveguide with silica cladding.

Fig. 3.14 shows the normalized deformation of the excited elastic Eigen mode for the gain at 12.9 GHz, it can be seen that the waveguide oscillates in the x, y and z directions. Therefore, the optical forces are transverse and longitudinal.

3.8.3 Rib Waveguide with Air Cladding

Fig. 3.15 shows the fundamental optical mode (normalized electric field to unity) of the rib SOI waveguide. The waveguide simulation dimensions were as follows: 170 nm silicon core height and 450 nm width ached at 50 nm height and 1000 nm width as silicon slab. Here again the light is almost purely confined in the core with a little part of evanescent field outside the core. Fig. 3.16 shows the same fundamental optical mode but in transparent view to clarify the optical field at the boundaries of the SOI waveguide core.

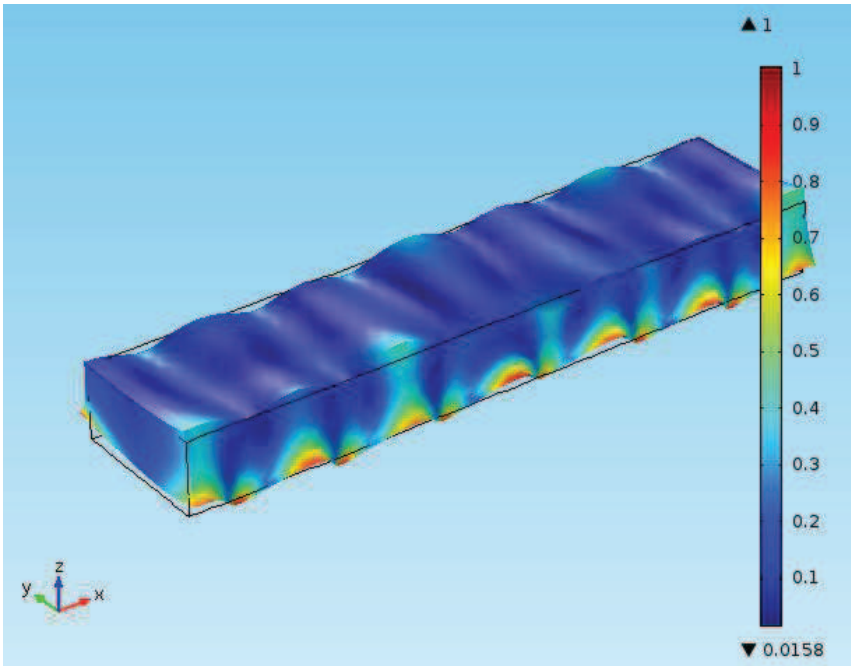

Figure 3.14: Elastic mode for the gain at 12.9 GHz in the BSBS of a strip waveguide with silica cladding.

Fig. 3.17 shows the gain profile of the excited elastic Eigen modes for FSBS in the rib SOI waveguide. As can be seen, there are four excited elastic Eigen modes in which the forces add up constructively and two modes in which the forces add up destructively. For example, at 12.85 GHz the constructive interference results in a total gain of 0.46×10^4 $(\text{m.W})^{-1}$ in which both forces produce identical coupling but the radiation pressure can be seen to be the dominant. Whereas, at 13.12 GHz the destructive interference results in a total gain of 0.01×10^4 $(\text{m.W})^{-1}$.

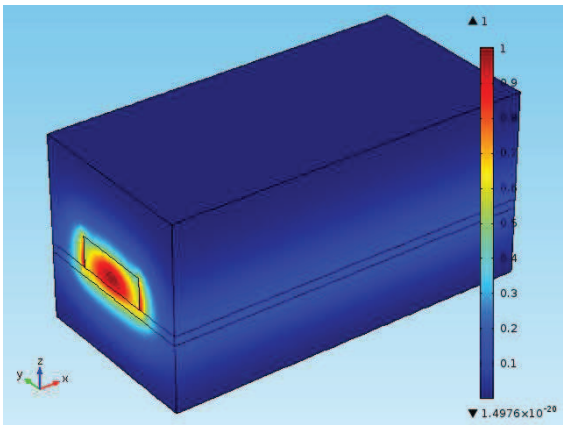

Figure 3.15: Normalized electric field of a rib waveguide with air cladding.

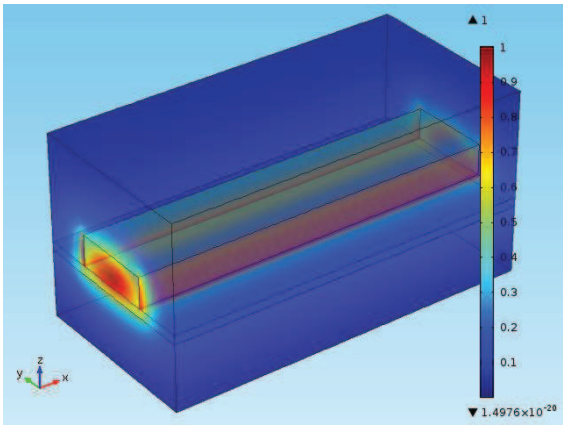

Figure 3.16: Normalized electric field of a rib waveguide with air cladding: transparent.

Fig. 3.18 shows the normalized deformation of the excited elastic Eigen mode for the gain at 12.85 GHz in the FSBS rib waveguide, it can be seen that the waveguide oscillates in the x, y and z directions. Therefore, the optical forces are transverse and longitudinal.

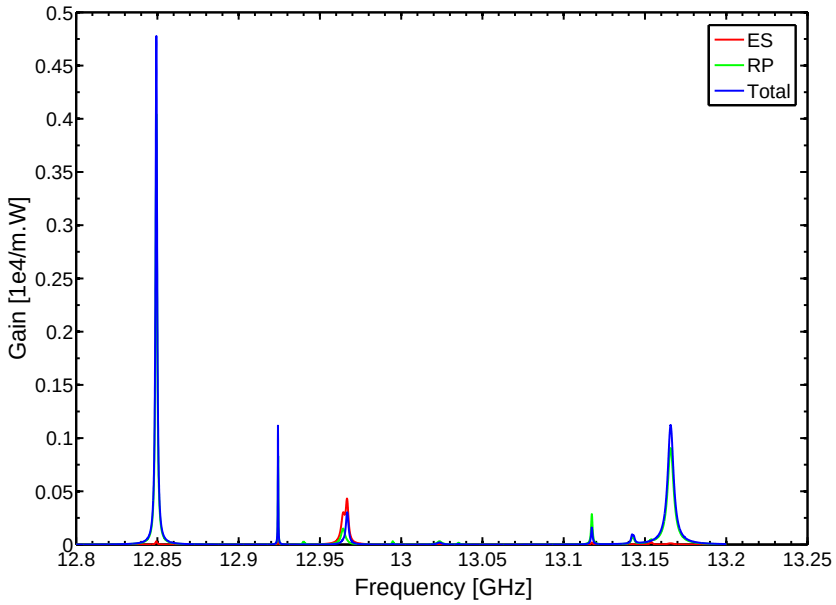

Figure 3.17: FSBS gain profile of a rib SOI waveguide with air cladding.

Fig. 3.19 shows the gain profile of the excited elastic Eigen modes for BSBS in the rib waveguide. As can be seen the constructive interference at 12.94 GHz results in a

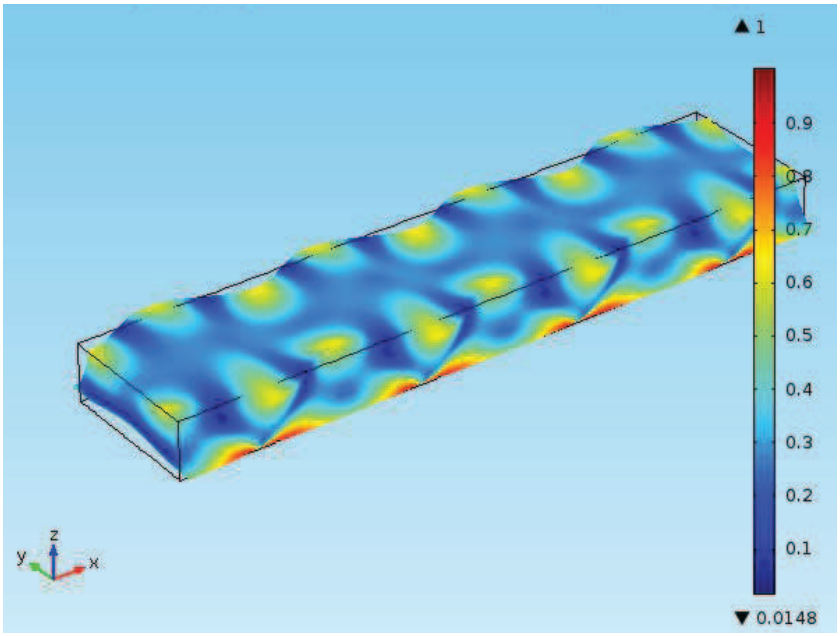

Figure 3.18: Elastic mode for the gain at 12.85 GHz in the FSBS of a rib SOI waveguide with air cladding.

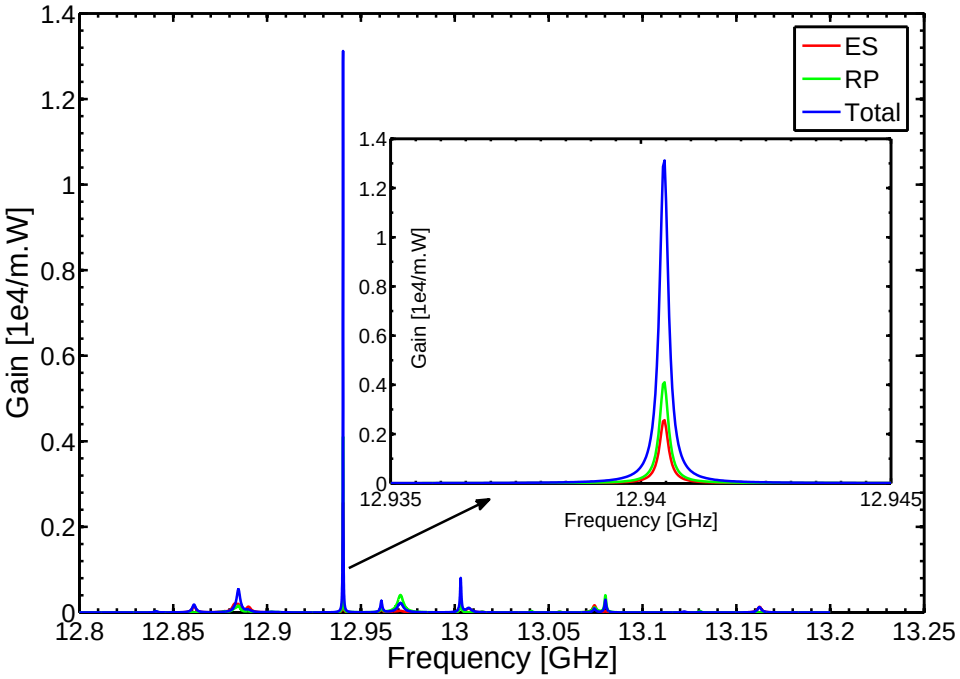

Figure 3.19: BSBS gain profile of a rib SOI waveguide with air cladding.

significant total gain of 1.32×10^4 $(\mathrm{m.W})^{-1}$.

The inset of Fig. 3.19 shows a magnified gain profile of the excited elastic Eigen mode at 12.94 GHz. As can be seen the radiation results in a gain of 0.41×10^4 $(\mathrm{m.W})^{-1}$ and the electrostriction results in a gain of 0.25×10^4 $(\mathrm{m.W})^{-1}$.

Fig. 3.20 shows the normalized deformation of the excited elastic Eigen mode for the gain at 12.95 GHz in the BSBS rib waveguide, it can be seen that the waveguide oscillates in the x, y and z directions. Therefore, the optical forces are transverse and longitudinal.

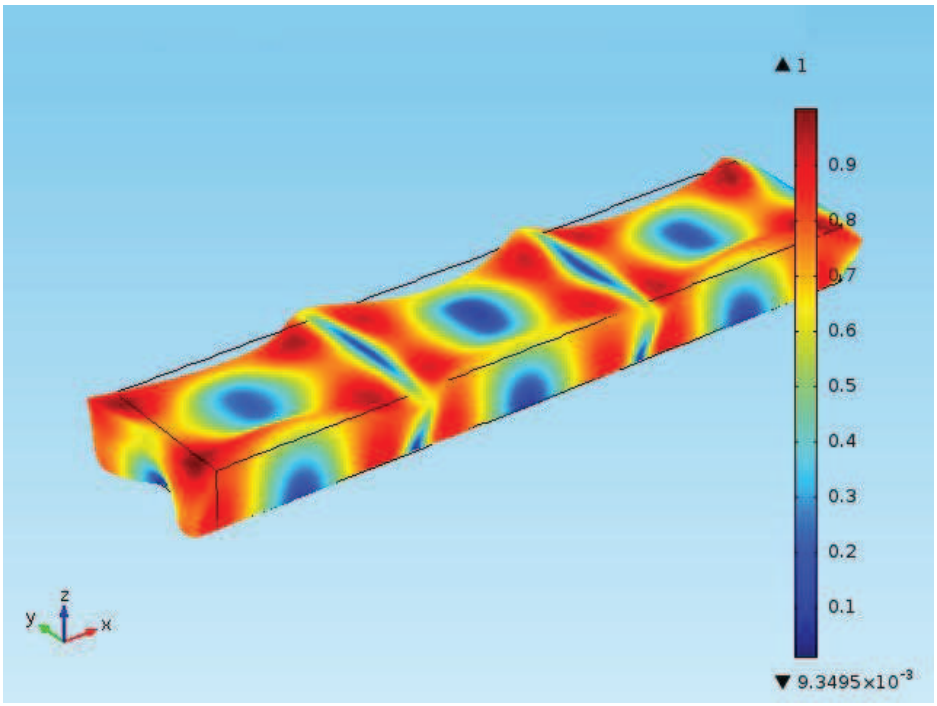

Figure 3.20: Elastic mode for the gain at 12.94 GHz in the BSBS of a rib SOI waveguide with air cladding.

3.8.4 Rib Waveguide with Silica Cladding

Fig. 3.21 shows the gain profile of the excited elastic Eigen modes for FSBS in the rib SOI waveguide. It can be seen that two excited elastic Eigen modes at 12.94 GHz and 12.969 GHz by which the constructive interferences mainly contribute from the ES and result in total gain contributions of 0.16×10^4 $(\mathrm{m.W})^{-1}$ and 0.05×10^4 $(\mathrm{m.W})^{-1}$, respectively. However, at 13.019 GHz, 13.035 GHz and 13.055 GHz destructive interferences took place and the total gain contributions result mainly from the RP.

The Figures 3.22 and 3.23 show two different elastic modes, Fig. 3.22 shows the excited elastic mode at 12.94 GHz in which the constructive interference results in a total gain of 0.16×10^4 $(\mathrm{m.W})^{-1}$, it can be seen that the deformations are symmetric about the z axis.

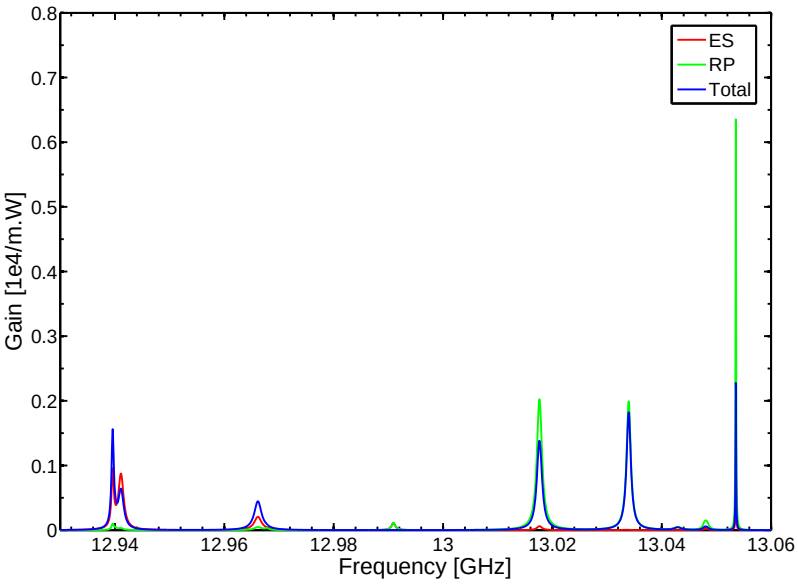

Figure 3.21: FSBS gain profile of a rib SOI waveguide with silica cladding.

Contrary to Fig. 3.22, Fig. 3.23 shows an unexcited elastic mode at 12.98 GHz since the deformations are antisymmetric. This gives a conclusion that only symmetric excited elastic modes can enhance the SBS non-linearity.

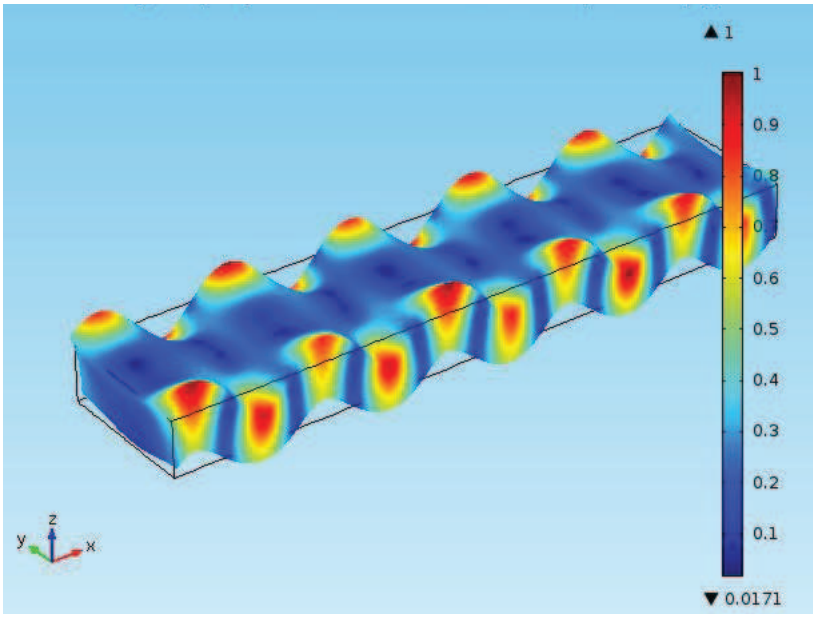

Figure 3.22: Excited elastic mode of the gain at 12.94 GHz in the FSBS of a rib SOI waveguide with silica cladding.

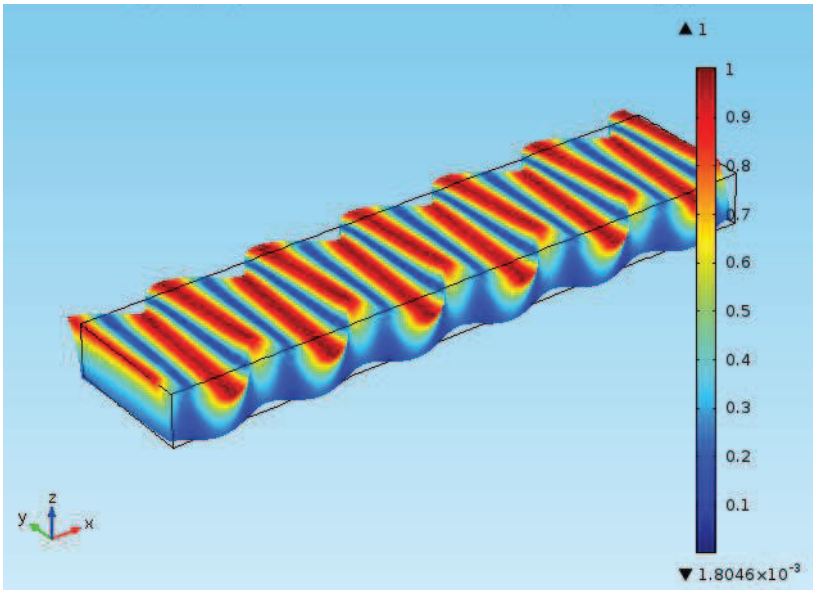

Figure 3.23: Asymmetric excited elastic mode at 13.048 GHz in FSBS of a rib SOI waveguide with silica cladding.

Fig. 3.24 shows the gain profile of the excited elastic Eigen modes for BSBS in the rib SOI waveguide. 3.24.

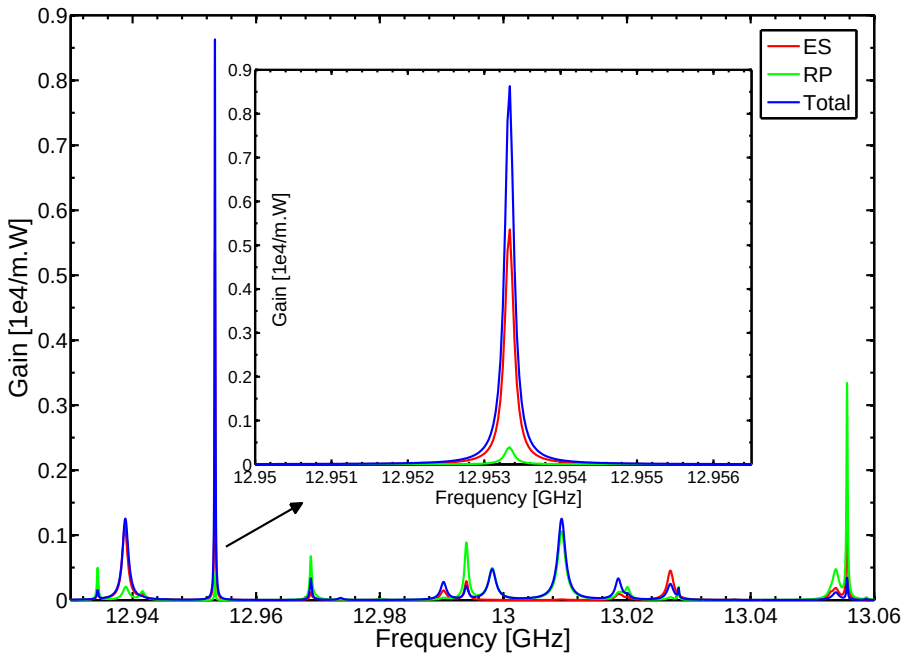

Figure 3.24: BSBS gain profile of a rib SOI waveguide with silica cladding.

It can be seen that there are five excited elastic modes by which the constructive interferences takes place. At 12.9533 GHz for example the constructive interference results in a significant total gain of 0.88×10^4 $(\mathrm{m.W})^{-1}$ by which the electrostriction is the dominant effect as shown in the inset of Fig. 3.24.

Fig. 3.25 shows the excited elastic mode at 12.9533 GHz for BSBS. It can be seen that there is a high deformation in z and therefore, the forces are mainly transverse.

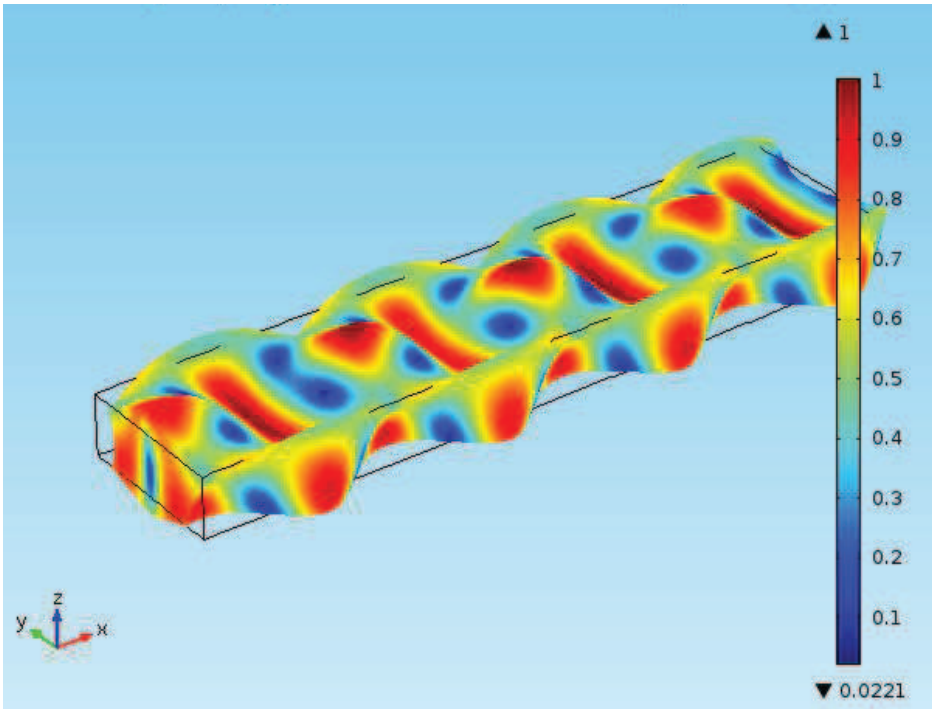

Figure 3.25: Excited elastic mode at 12.9533 GHz in the BSBS of a rib SOI waveguide with silica cladding.

3.9 Discussion and Concluding Remarks

The multi-physics simulations exhibit that in both strip and rib SOI waveguides, the propagating light is highly confined in the waveguide core due to the high index contrast between the core and air or silica cladding, as well as due to the sub-wavelength dimension of the core regarding to single mode propagation at 1550 nm telecommunication wavelength. Therefore, this highly confinement excites the elastic modes inside the SOI waveguides and therefore the non-linear effects like SBS. Table 3.1 shows the summary of the parameters which were used within simulations. For each SOI waveguide type, three input pump powers (100, 75 and 50 mW) were used to calculate the power inside the waveguide using Eq. 3.24, the FSBS and the BSBS gain coefficients as well as the

Stokes power values using Eq. 3.23.

Table 3.1: Summary of the parameters for the simulated SOI waveguides and expected Stokes power values. SiO2: Silica.

Waveguide Type	Input Power [mW]	Power inside Waveguide [mW]	FSBS Gain [10^4/m*W]	BSBS Gain [10^4/m*W]	Expected FSBS Stokes Power [µW]	Expected BSBS Stokes Power [µW]
Strip/Air Clad	100 75 50	53 39 26	0.13 0.095 0.013	0.21 0.13 0.08	1.3 1.1 1	1.5 1.2 1.1
Strip/SiO2 Clad	100 75 50	51 38 25	0.1 0.093 0.011	0.13 0.094 0.01	1.2 1.1 1	1.2 1.1 1.01
Rib/Air Clad	100 75 50	52 39 26	0.47 0.35 0.2	1.32 1.19 1.07	2.5 1.7 1.2	14 6 3
Rib/SiO2 Clad	100 75 50	49 37 24	0.25 0.12 0.06	0.9 0.79 0.65	1.6 1.2 1	6 3.3 2

Simulations reveal that the best waveguide type to achieve the highest SBS nonlinearity is the rib air cladding waveguide for the BSBS. Referring to table 3.1, the rib air cladding SOI waveguide achieved a significant peak gain coefficients of 1.32×10^4 $(\mathrm{m.W})^{-1}$ for BSBS and the calculated Stokes powers of 14, 6 and 3 (μW) for the input pump powers of 100, 75 and 50 (mW), respectively. Due to the superposition of the gains which are originating from the pressure and electrostriction forces, a strong photon-phonon coupling with a dominant effect of radiation-induced coupling was obtained. Comparing to the SBS gain coefficient in SSMF, it is only $2\mathrm{e}^{-11}$ (m/W).

Additionally, the detailed investigations of the interaction between the electrostriction and radiation forces, in FSBS for instance, had been shown that the transverse forces are the dominant, i.e. the transverse forces govern the FSBS coupling. In contrast, the forces that mediate the BSBS coupling were generated from the superposition of the longitudinal and the transverse forces because of the counter propagating pump and Stokes waves by which they modal interfere to generate the longitudinal forces. Both electrostriction and radiation forces as well as the waveguide deformations are scaled quadratically with the SBS gain coefficients resulting in a non-linear addition of electrostriction and radiation effects for the combined SBS gain. Therefore and within SOI waveguide fabrication process, the SBS effect can be enhanced via two ways:

1. Decrease the SOI waveguide core cross section area, therefore the optical forces will increase.

2. Fabricate the SOI waveguide in a way that makes the silicon core suspended, therefore the elastic deformations will increase [18].

In the modes where the electrostriction forces are the dominant and referring to the elastic modes oscillations, it can be seen that transverse forces have both inward and outward deformation directions. This can be understood from the different signs of the photo elastic coefficients in the electrostrictive tensor. Hence, the main diagonal coefficients have the minus sign while the other coefficients have the plus sign.

According to Figures 3.21 and 3.23 it can be seen that only symmetric waveguide oscillations enhance the SBS non-linearity. The direct interference between the optical forces can enhance or suppress the SBS process, since the Transverse Electric (TE) like mode results in symmetric force distributions for both electrostriction and radiation. Therefore, only phonon modes with even displacement with respect to the SOI waveguide core can achieve the effective SBS coupling.

Additionally, if the TPA effect limitation is considered and referring to the simulated power values inside the waveguide in table 3.1, it can be noticed that only 50 mw input power is possible to achieve the SBS non-linear effect, otherwise the TPA non-linear effect could take place. Since for (50 mW) input pump power, the calculated power inside the waveguide is below the TPA threshold, i.e. 30 (mW), as mentioned earlier. Referring to Eq. 3.24 by which the power inside the waveguide was calculated and the effective refractive index was simulated, the power loss between the input and the power inside the waveguide was due to the coupling losses which are included in the simulated effective refractive index values. In principle, one can use the fiber laser or Distributed Feed Back (DFB) lasers as a pump source of 5 mW output power with several amplifiers to reach the optimum input power of 50 (mW). Each of the fiber laser and the DFB lasers has a linewidth smaller than the SBS linewdth, therefore the expected Stokes linewidth would be about the natural SBS gain linewidth relating to the convolution of the SBS gain and the pump wave.

3.10 Suggested Experimental Setup

The suggested experimental setup to measure the SBS gain using the SOI waveguide is shown in Fig. 3.26. The blue color refers to the setup equipments that could be used to achieve FSBS measurement while the green refers to the setup that could be used to achieve the BSBS measurement.

An optical signal would be modulated using the intensity modulator (IM) and a sweep (fmod) RF signal would be used to scan the achieved gain profile of the SOI waveguide afterwords. The bias voltage (BV) would be used to suppress the carrier of the IM and the tuneable filter (TOF) would suppress the unwanted sideband and the remaining carrier of the modulator. The selected sideband out of the TF would be amplified via the Erbium Doped Fiber Amplifier (EDFA2) to be coupled with the amplified pump wave via 90/10 coupler. A fiber or DFB lasers could be used as pump source. EDFA1 output should be set for 50 mW in order to get rid of the TPA effect. Both the pump wave (blue) and the scan signal would be launched to the SOI waveguide to achieve FSBS,

while the alternative pump (green) would be launched to the SOI waveguide via port 2 of the circulator (C) to achieve BSBS as explained previously. In both FSBS and BSBS cases, the amplified signal (via SBS effect) out of the SOI waveguide would be coupled out of port 3 of the (C) and used as input to the photo diode to be measured versus the sweep RF frequency of the scanning signal via GPIB and a Labview program at the PC.

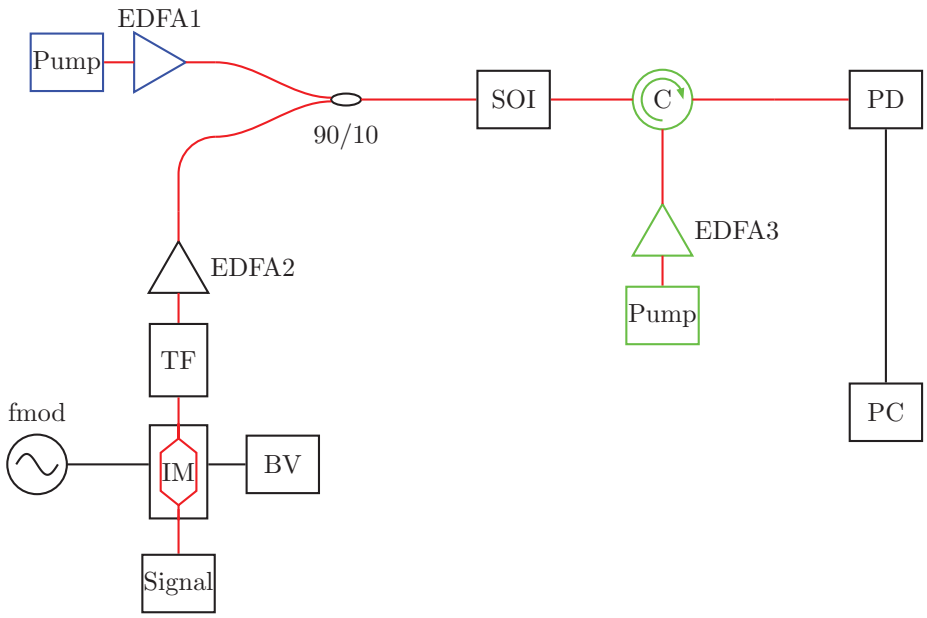

Figure 3.26: Suggested experimental setup for the SBS gain measurement within the SOI waveguide, IM: intensity modulator, EDFA: Erbium Doped Fiber Amplifier, fmod: modulation frequency, TF: tuneable filter, BV: bias voltage, SOI: Silicon on Insulator waveguide , PD: photo diode, PC: personal computer.

3.11 Summary

The silicon crystalline structure had been studied to derive the silicon photo-elastic tensors which were used to find the opto-mechanical forces inside the SOI waveguide. Among a variety of non-linear effects within silicon, the (TPA) which is a third order non-linear process is strongly limiting the SOI devices behavior. The TPA absorbs the pump field and therefore free carries will be generated. Hence, significant optical losses will take place through the accumulation of the free carriers inside the SOI waveguide. TPA can be avoided via several methods like reducing the input power and increase the device length.

Four kinds of forces had been investigated inside the nano-silicon waveguide via the overlap integral between the optical forces and the elastic Eigen modes. The bulk (body forces) and boundaries (pressure forces) non-linearities are formulated as bulk and bound-

ary integrals over the waveguide cross section and boundaries, respectively. Both body and pressure electrostriction forces had been derived from the photo-elastic tensor. The radiation body and pressure forces had been derived from the Maxwells stress tensor.

The Brillouin gain had been calculated from the overlap integral between all forces and the elastic deformation which is caused by the forces. The integration is taken over the waveguide cross section for body forces, while for pressure forces the integration is taken over the boundaries.

Two kinds of waveguides are investigated: strip and rib waveguides. For each kind, two cases are studied: air and silica cladding. The FSBS and BSBS gain within the wave guide had been calculated. It is shown that an unprecedented high SBS gain with a large magnitude can be found in many elastic Eigen-modes. A constructive interference between the forces could be found mainly with symmetric deformation of the SOI waveguide. The rib air cladding waveguide was achieved the highest BSBS non-linearity with a significant peak gain of 1.32×10^4 $(\mathrm{m.W})^{-1}$ which is order of magnitudes higher than the optical fibers peak gain coefficient.

In table 3.1, three pump powers (100, 75, and 50 mW) were simulated to find the appropriate pump power for the waveguide. It is found that with 50 (mW) pump power, the power inside the waveguide is below the TPA threshold which is 30 (mW). Therefore, the recommended maximum pump power within the suggested experimental setup was 50 mW.

Chapter 4

Extraction of High Quality Single Laser Lines

4.1 Introduction

Since the high interest in coherent detection systems as a local oscillator for optical communications as well as high resolution spectroscopy, wavelength-division multiplexing (WDM) systems and multilevel modulation formats, great efforts had been payed toward the development of stable, widely wavelength-tuneable and narrow linewidth single line lasers [60, 61, 62, 63]. Highly stable and narrow linewidth lasers are very important for digital coherent detection systems, since they are used as a technique for the enhancement of the capacity and spectral quality of the next-generation fiber-optical networks [64]. For optical sensors such high quality lasers, mainly stable single line lasers, are necessary as well.

Many methods had been demonstrated to achieve the desired requirements of the single line laser, such as widely tuneable, narrow linewidth and stable lasers for the above mentioned applications. For example, less than 5 MHz laser linewidth over 40 nm tuning range was reported using a distributed Bragg reflector (DBR) laser [65]. Additionally, in [66] a single-longitudinal mode laser with a linewidth of less than 20 kHz using a long-cavity, narrow-bandwidth SBS as filter and multi-frequency selection mechanism simultaneously had been presented. In [67] a linewidth of less than 5 kHz and a stability of 62.2 MHz for a single longitudinal mode laser is reported using spectral overlapping of two uniform fiber Bragg gratings (FBG). On the other hand, a method to reduce the linewidth of commercially available distributed feedback (DFB) laser diodes down to 1.8 kHz with an electro-optical feed-forward loop was reported [68]. Since the SBS gain bandwidth can be reduced via several amplification stages [69], a linewidth below 1 kHz of a single frequency and continuous wave Brillouin fiber-ring laser was achieved by utilizing an unbalanced Mach-Zehnder interferometer as a coupling device [70]. Regarding the laser tuneability, a conventional DFB laser diode has a tuneability range of 2-6 nm.

However, in [68] a tuneability range of 40 nm was reported for a DFB laser.

In principle, all the previous attempts for enhancing the lasers quality are limited either in the minimum linewidth or tuneability range, or both. Therefore, in this chapter a simple method to extract one spectral laser line out of a frequency comb which is generated by a mode-locked fiber laser (MLFL) will be demonstrated and experimentally implemented. The frequency comb has unique features such as broad bandwidth i.e. thousands of spectral lines with equidistant frequency spacing (25 MHz up to 10 GHz depending on the resonator length [76]) and a highly stable amplitude. Additionally, according to [71, 72] some frequency combs have a bandwidth of about 100 nm and the linewidth of each spectral mode could reach down to sub-millihertz.

In order to extract one spectral line out of thousands of lines, a narrow band optical filter is required. Thus, if the repetition rate is in the range of 100 MHz, an optical filter with a bandwidth less than 100 MHz is needed. Therefore, conventional optical filters are not sufficient such as a wave shaper optical filter which has a minimum bandwidth of 10 GHz or a coated thin film band bass filter which has a bandwidth in the GHz range. In [73] for example, a 325 MHz bandpass filter is reported via Fiber Bragg Gratings (FBG). Narrow FBG cannot be tuned very far and conventional FBGs are too broad. However, in [74] a Fabry-Perot filter of 250 MHz bandwidth with several filter modes as well as a repetitive structure was reported.

Thus, here the non-linear effect of polarization pulling assisted SBS (PPA-SBS) had been utilized as a filter and amplifier [26]. Such a filter offers a narrow bandwidth in the order of 10-30 MHz within standard single mode fibers (SSMF). Therefore, the bandwidth of PPA-SBS is less than the frequency difference between any two neighboring spectral lines of the frequency comb. Hence, any specific spectral line can be discriminated. In principle, the idea behind the extraction of the desired spectral comb line via PPA-SBS is the suppression of the unwanted spectral lines via the careful polarization setting of the pump wave (which is used to generate the SBS effect) and the pre-filtered (to provide sufficient signal to noise ratio for the next step) comb lines by a polarization controller. Therefore, the state of polarization of the desired and amplified spectral comb line via SBS is perpendicular to the state of polarization of the unwanted comb lines. Additionally, the linewidth determination of the extracted spectral line is very important. Therefore, several techniques will be presented to determine the linewidth of the spectral line.

This chapter is organized as follows: optical frequency comb operation principles and generation are explained. The polarization pulling assisted SBS is introduced and the previously derived SBS differential equations are modified depending on the state of polarization of both pump and Stokes waves. Several laser linewidth measurement techniques are presented. The experimental setup and results for the extraction of the laser, linewidth measurement, tuneability and stabilization are presented as well. Finally, a discussion, concluding remarks and a summery are given.

4.2 Optical Frequency Combs

In the late 1970s the optical frequency comb was developed through a picosecond laser [75]. There are many different mechanisms to generate optical frequency combs including: amplitude modulation of a continuous wave laser, four wave mixing, micro-ring resonator or a mode locking inside a lasers cavity [76]. The most popular and famous mechanism for achieving a frequency comb is a mode locked laser (MLL). In the frequency-domain the frequency comb consists of thousands of equidistant narrow spectral lines over a broad spectral range each spectral line is known as a mode. If all these frequencies (modes) are locked in phase, i.e. fixed phase relationship between all of the lasing longitudinal modes, this corresponds to a sequence of pulses in the time domain. Fig. 4.1 shows the representation of a pulse train composition by adding three waves with different frequencies (modes). The vertical black line refers to the time points where all waves are equal in phase.

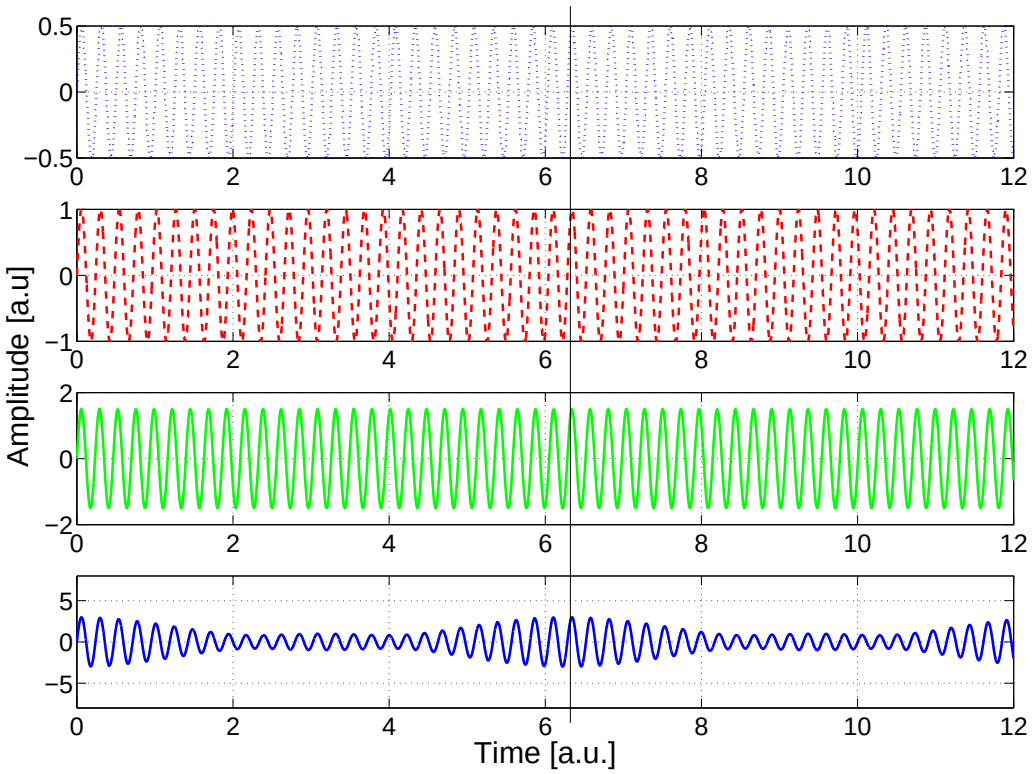

Figure 4.1: Pulse train composition (solid blue) by superposition of three different frequency waves.

Generally, the laser requires a cavity consisting of two mirrors with different perme-

ability by which the laser light can resonate (radiate) and pass through a gain medium. The gain medium such as an erbium-doped fiber will compensate for losses during the light propagation inside the cavity. Laser diodes are mainly used for the pumping of MLL. Hence, the laser diode provides energy to the gain medium, whereas the circulating pulse reproduces energy in a uniform time period. The term mode locking refers to the method by which ultra-short laser pulses can be obtained. For mode locking, the laser cavity needs to contain either an active element such as an optical modulator or a non-linear passive element such as a saturable absorber. Therefore, the formation of ultra-short pulses will circulate inside the laser cavity. Every time the pulse hits the output coupler mirror, a part of the pulse will be emitted and therefore a pulse train will be generated.

The different frequency lines are separated by the repetition rate which is the inverse of the round trip time of the laser resonator. Whereas, the pulse duration is inversely related to the number of the involved modes times the frequency spacing between them, i.e. more involved modes result in a shorter pulse duration.

Frequency combs are commonly used in metrology [77]. In the field of ultrafast spectroscopy the interest is to achieve extremely short time domain bursts of the electric field, which requires a large spectral bandwidth. In contrast, in the field of precision measurements the interest is to have lasers with a very narrow spectral linewidth. Therefore, both requirements can be satisfied simultaneously by utilizing a MLL frequency comb. Frequency combs can also be used for atomic clocks and Lidar (inspecting technology by which a distance can be measured by illuminating a target with a laser light) or the synthesization of arbitrary optical waveforms by modulating the phase and amplitude of individual lines [78, 79, 80]. Moreover, the extraction of spectral lines out of the frequency comb is very important. For example, they can be used to generate high quality single line lasers [24], as well as high quality microwaves with phase noise much lower than achievable by conventional microwave oscillators as will be shown in the next chapter [25].

To understand how the mode-locked laser is working, a simulation model had been made for 100 modes without phase coherence between the modes, the results are shown in Fig. 4.2. In principle, the simulated model adds up cavity electrical field modes. The cavity and simulation parameters were set as follows:

The noise factor was either 0 (phase locking) or >> 0 (large phase noise), the cavity length was l = 1.5 m, and the free spectral range of the cavity was FSR = $c_0/(2\times l)$. The total electric field $E = E_m \cos(2\pi f t + \Delta\nu)$, where f is a frequency goes from fundamental to higher laser frequencies with a step of the free spectral range, $\Delta\nu$ is the phase and t is the time from 0 to 50 ns.

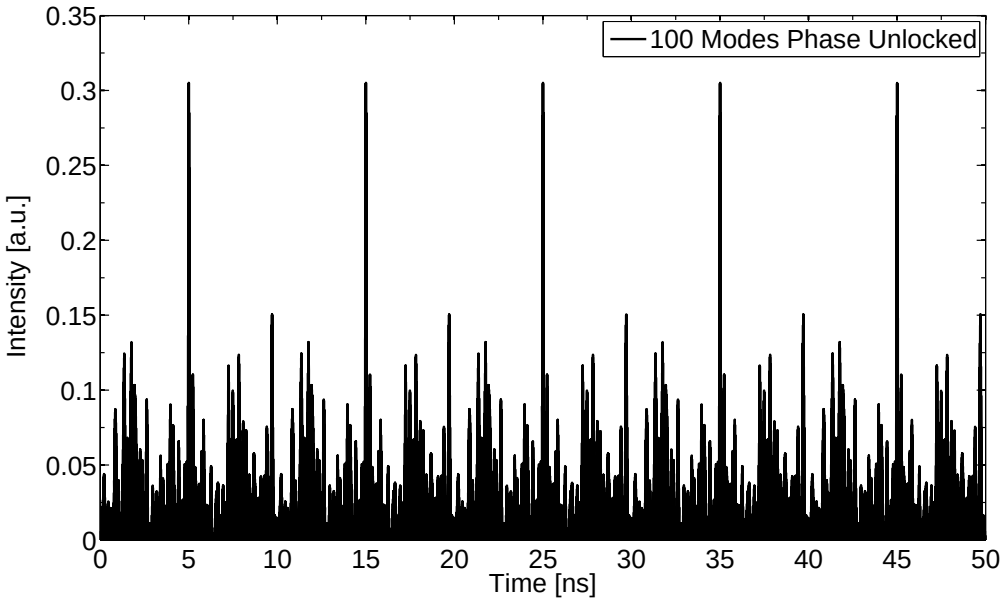

Figure 4.2: Simulated 100 phase unlocked laser modes.

The time domain in Fig. 4.2 shows a large amount of unequal phase laser modes, since each mode has a randomly changing phase with respect to the others. However, in Fig. 4.3 and Fig. 4.4, 10 and 100 modes laser output with phase coherence between the modes are simulated, respectively. The time domain shows that with phase locking, i.e. fixing the phase relation between the modes, the modes interfere constructively at multiples of the cavity round trip time where the phases are equal. Referring to Fig. 4.4, the mode-locking process achieves shorter pulses such as a spikes with the increasing of the number of modes.

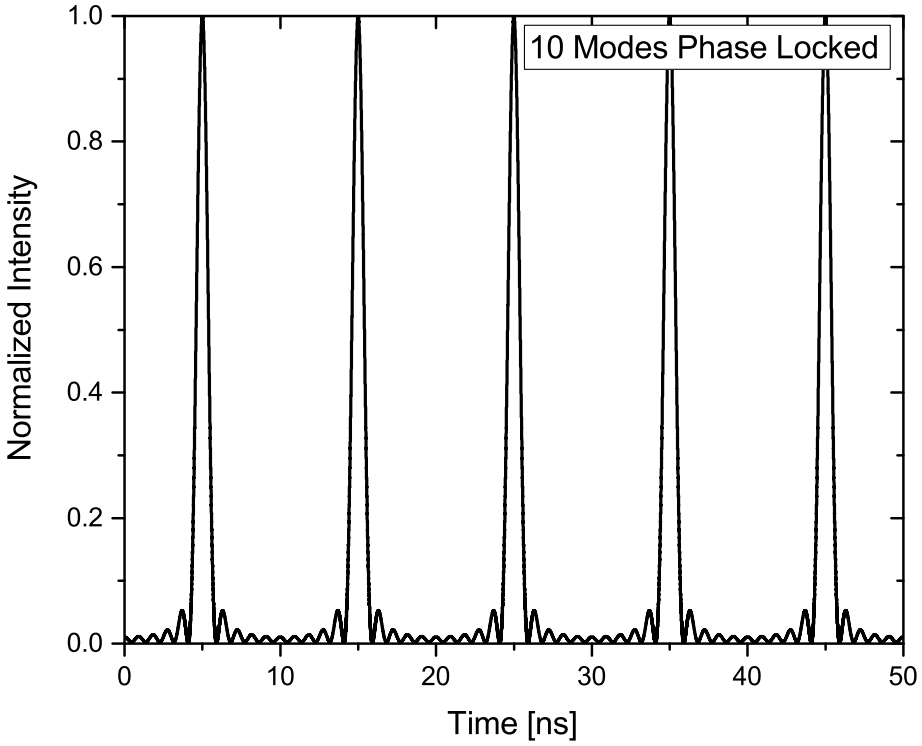

Figure 4.3: Simulated 10 phase locked laser modes.

4.3 Polarization Pulling-Assisted SBS

Through SBS process, there is interference between the pump and the counter propagating signal waves. This interference has its maximum when both the pump and the signal electric fields have the same polarization. In principle, when both pump and signal electric field vectors trace parallel ellipses within the same rotation direction, the interference between both pump and signal is more efficient. Whereas, if these identical ellipses traced in opposite rotation directions i.e. perpendicular to each other, then the interference could vanish. Thus, the input state of polarization (SOP) of both the pump and the signal waves plays an important role for achieving the maximum interference (gain) between the pump and the signal waves. Therefore, by carefully setting the input SOP for both pump and signal, maximum signal amplification could be achieved. For instance, for 5 km SSMF the maximum Brillouin gain was obtained when both pump and signal waves have the same polarization, while for perpendicular polarization minimum gain was obtained [81].

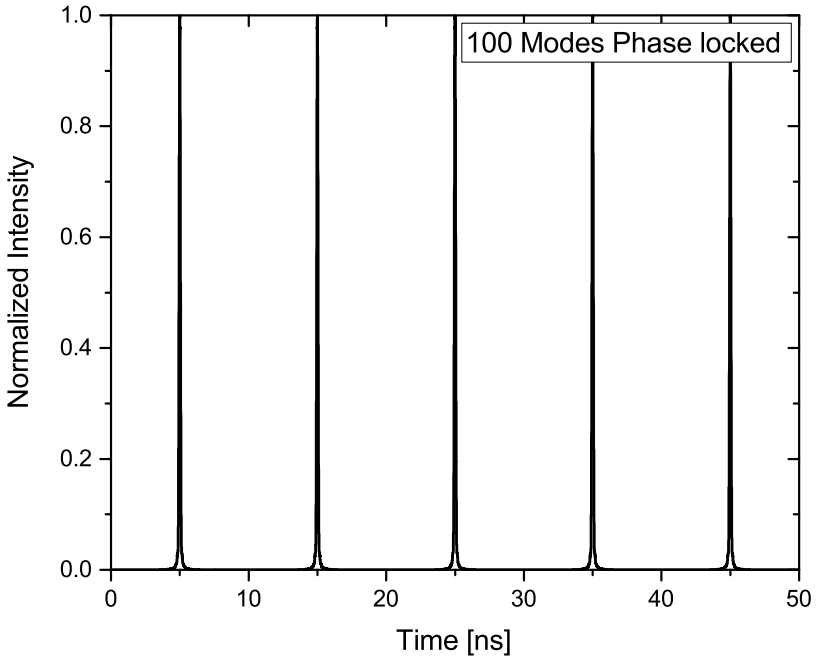

Figure 4.4: Simulated 100 phase locked laser modes.

As mentioned earlier, in order to select one spectral line of the frequency comb, a narrow bandwidth optical filter is required where its bandwidth should be less than the frequency difference between each neighboring spectral lines. Hence, conventional optical filters are not sufficient and therefore the PPA-SBS will be utilized as can be seen later.

According to [82], to describe the SOP of an optical signal the Stokes representation can be used as $[\underline{S} = S_0, S_1, S_2, S_3]$, where $(\underline{S})$ is the SOP of the incident light and (S_0, S_1, S_2, S_3) are the SOP of the light emerging from the four quadrants of the half-shade system, see [82] for more details. Therefore, if two coherent optical co-propagating signals with polarizations (S_a, S_b) are mixed at a photomixer, the mixing efficiency can be written as [83]:

$$\psi(\Longrightarrow) = \frac{1}{2}(S_a S_b) = \frac{1}{2}(1 + S_{1a}S_{1b} + S_{2a}S_{2b} + S_{3a}S_{3b}) \tag{4.1}$$

where the components S_1, S_2, S_3 are considered to be normalized to unit intensity $S_0 = 1$. Additionally, no depolarization of the forward pump wave is considered, i.e., $(s_1^2 + s_2^2 + s_3^2 = 1)$.

In principle, the mixing efficiency can be considered as a punishment against polarization mismatch at a coherent mixer. Hence, for co-propagating $(\Longrightarrow)$ optical signals

of identically ($\parallel$) and perpendicularly ($\perp$) polarized pump and signal waves, respectively the mixing efficiencies can be written as [83]:

$$\psi(\Longrightarrow\parallel) = \frac{1}{2}(1 + S_1^2 + S_2^2 + S_3^2) = 1 \tag{4.2}$$

$$\psi(\Longrightarrow\perp) = \frac{1}{2}(1 - S_1^2 - S_2^2 - S_3^2) = 0 \tag{4.3}$$

Whereas, for counter-propagating ($\rightleftharpoons$) pump and signal waves the Stokes representation will be: $[\underline{S} = 1, S_1, S_2, -S_3]$ [84]. Hence, Eq. 4.1 can be rewritten with polarizations $(\underline{S_p}, \underline{S_s})$ as:

$$\psi(\rightleftharpoons) = \frac{1}{2}(S_p S_s) = \frac{1}{2}(1 + S_{1p}S_{1s} + S_{2p}S_{2s} - S_{3p}S_{3s}) \tag{4.4}$$

Therefore, and according to [83] equations 4.2 and 4.3 can be rewritten for the counter-propagating pump and signal waves as:

$$\psi(\rightleftharpoons\parallel) = \frac{1}{2}(1 + S_1^2 + S_2^2 - S_3^2) = 1 - S_3^2 \tag{4.5}$$

$$\psi(\rightleftharpoons\perp) = \frac{1}{2}(1 - S_1^2 - S_2^2 + S_3^2) = S_3^2 \tag{4.6}$$

For an optical fiber such as SSMF which shows low birefringence, i.e. the growth of the signal SOP is mainly governed by the SBS, equations 4.5 and 4.6 will be [83]:

$$\psi(\rightleftharpoons\parallel) = \frac{2}{3} \tag{4.7}$$

$$\psi(\rightleftharpoons\perp) = \frac{1}{3} \tag{4.8}$$

Equations 4.7 and 4.8 show that, when the pump and the signal waves have the same SOP, then $(\frac{2}{3})$ of the pump power is utilized to amplify the counter-propagating signal. While $(\frac{1}{3})$ of the pump power is used for that amplification when the SOP of the pump

and signal waves are perpendicular to each other. Therefore, equations 2.52 and 2.53 can be rewritten as:

$$\frac{dI_P}{dz} = -\psi(\rightleftharpoons) g_B I_P I_S - \alpha_p I_P \tag{4.9}$$

$$\frac{dI_S}{dz} = -\psi(\rightleftharpoons) g_B I_P I_S + \alpha_s I_S \tag{4.10}$$

Additionally, in [85] it is reported that within the SBS process it can be seen a force that pulls the signal vector towards the pump vector. In principle, this force magnitude is directly proportional to the pump power and depends on the local projection of the pump vector on the signal vector as illustrated in Fig. 4.5. The left hand side of Fig. 4.5 shows the vectors of the pump (E_p) and maximum and minimum signal powers ($E_{s(max)}, E_{s(min)}$) before the PPA-SBS non-linear effect takes place. Whereas, the right hand side of Fig. 4.5 shows the vector representations of the pump and signal after the PPA-SBS non-linear effect. According to the earlier mentioned force principle, the short black signal vector is pulled towards the pump vector. Thus, $G_{max}(\omega_s) >> G_{min}(\omega_s)$. The amplified signal is illustrated by the red long vector which represents the signal vector under SBS effect when the SOP of both pump and signal waves have the same orientation.

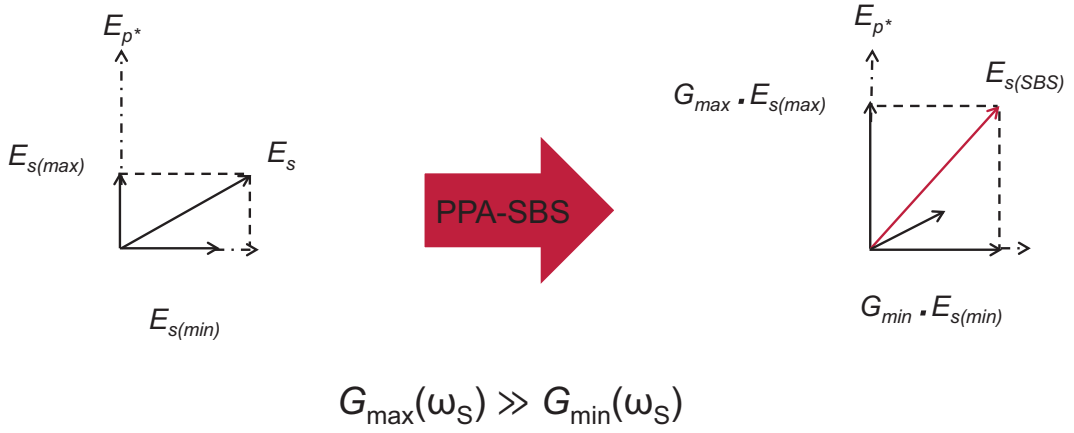

Figure 4.5: PPA-SBS process vectors illustration. $G_{max}(\omega_s)$ and $G_{min}(\omega_s)$ are the maximum and minimum Brillouin gain, respectively.

Once the PPA-SBS is utilized to discriminate and amplify one spectral line out of the frequency comb as explained in section 4.5, the linewidth of such selected line must be measured. Therefore in the next section, several linewidth measurements will be presented.

4.4 Laser Linewidth Measurement Techniques

Many applications require a full characterization of the laser parameters. For example, a laser linewidth measurement gives high potential for atomic physics, metrology and telecommunications applications, to name a few [86, 87, 88]. Additionally, in communications the proper narrow linewidth lasers and the high transmission rates demands could develop the coherent communications to the next step [89]. Since the linewidth is directly related to the achieved signal to noise ratio (SNR), these applications depend directly on the linewidth of the used lasers. Thus linewidths in and below the kHz are highly recommended for several applications and research fields. Many techniques are demonstrated to measure the laser linewidth, mainly based on the interference of two optical fields at a proper photo diode (PD) or converting frequency fluctuations into intensity fluctuations using a Mach-Zehnder interferometer. Here they are explained briefly.

4.4.1 Heterodyning with a Local Oscillator

In principle, the interference between two optical fields at a proper PD (non-linear element) results in a beat note frequency centered at the frequency difference between the interfered optical waves. The resulting linewidth is a convolution of both waves linewidths. The photo-current out of the PD, is analyzed at an electrical spectrum analyzer (ESA). Hence, the resultant beat note characteristics can be investigated in the electrical domain.
The two optical fields are the laser under test (LUT) which has unknown spectral characteristics and the local oscillator laser as a reference. The response at the ESA contains the direct detection part between the PD and the ESA and the heterodyne spectrum part. The relation that governs the power spectrum out of the PD is [90]:

$$S_i(f) \cong R^2 \left\{ \underbrace{S_d(f)}_{direct\ detection} + \underbrace{2[S_{LO}(\nu) \otimes S_{LUT}(-\nu)]}_{heterodyne\ spectrum} \right\} \tag{4.11}$$

where R is the PD responsivity, $S_d(f)$ is the ordinary direct detection spectrum at the ESA, $[S_{LO}(\nu) \otimes S_{LUT}(-\nu)]$ is the heterodyne mixing part which is a convolution between the local oscillator and the LUT signal. The time-varying multiplication between the local oscillator and the LUT at the PD produces the convolution product. In principle, multiplication in time domain is referred to convolution in frequency domain. As the convolution scans from negative to positive infinity, it passes the local oscillator at ν_{LO} as well as the LUT line shape.

As shown in the illustration of Fig. 4.6, the resultant beat note is a line shape translation as well as the power of the LUT at a frequency difference between the local oscillator and the LUT which is accessible by electronics. Assuming that the local

oscillator linewidth is very narrow, Eq. 4.11 can be rewritten as:

$$S_i(f) \cong 2R^2 P_{LO} S_{LUT}(\nu - \nu_{LO}) \tag{4.12}$$

where P_{LO} is the local oscillator power.

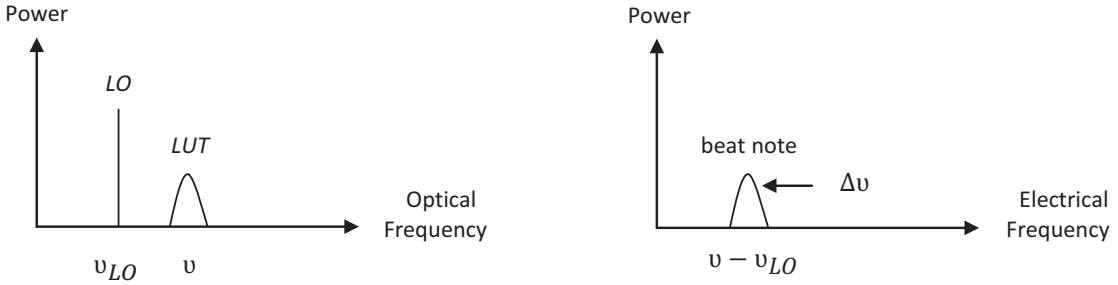

Figure 4.6: Heterodyne process illustration between laser under test (LUT) and local oscillator (LO).

In principle, the ESA will measure a signal proportional to the real LUT spectrum. Thus the local oscillator needs to be very stable with narrow linewidth, i.e. at least less than the LUT linewidth. Therefore, this technique is limited by the local oscillator characteristics itself.

4.4.2 Delayed Self-Heterodyne

The main idea behind the delayed-self heterodyne technique is to split the LUT in two ways using an optical interferometer. One way is delayed (to achieve uncorrelated ways) by a low-loss optical fiber and therefore it is phase shifted comparing to the other not delayed part. However, the non-delayed way can be frequency shifted by a modulator for instance. Both are coupled into a proper PD and the beat note will be analyzed at a proper ESA. Therefore, an individual local oscillator is not required. The detected beat note spectrum is a convolution between the coupled waves. Just like the heterodyne case, the detected spectrum at the ESA contains the direct detection and the mixing parts. Hence, Eq. 4.11 can be rewritten as:

$$S_i(f) \cong R^2 \left\{ \underbrace{S_d(f)}_{direct\ detection} + \underbrace{2[S_{LUT}(\nu - \delta_\nu) \otimes S_{LUT}(-\nu)]}_{heterodyne\ spectrum} \right\} \tag{4.13}$$

where δ_ν is a frequency difference generated at the frequency shifter and applied to the non-delayed way within the interferometer. As illustrated in Fig. 4.7, the resultant beat note linewidth, i.e. full width at half maximum (FWHM) will be twice the real linewidth for a Lorentzian-shaped laser. Whereas, for a Gaussian-shaped laser the beat note at the

ESA has a FWHM spectrum greater than the original *LUT* spectrum by a factor of $\sqrt{2}$.

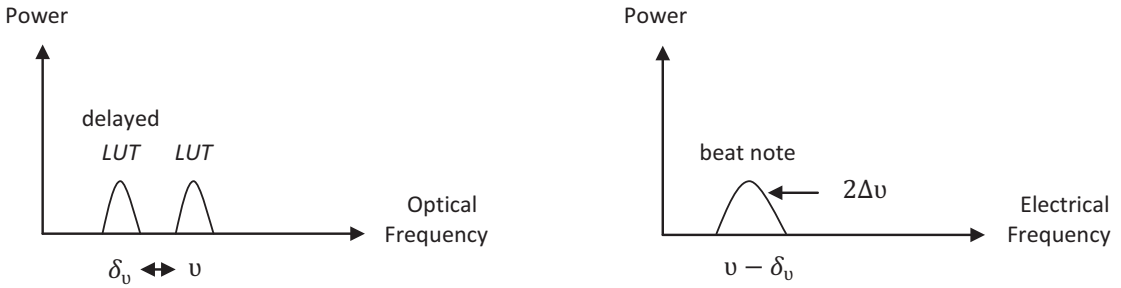

Figure 4.7: Self-Heterodyne process illustration between *LUT* and delayed *LUT*.

The fiber delay length (coherence length) depends on the linewidth of the *LUT*. That is, as long as the fiber delay length is longer than the coherence length the measurement is assumed to be correct. Therefore, the two coupled waves are uncorrelated.

The following relations govern the measurement accuracy of the delayed self-heterodyne technique:

$$L_c = \frac{c}{n}\tau_c \tag{4.14a}$$

$$\tau_c = \frac{1}{\pi\Delta\nu} \tag{4.14b}$$

$$\tau_c << \tau_d \quad ... \quad Incoherence \quad Condition \tag{4.14c}$$

where: τ_c is the coherence time, τ_d is the time delay induced by the fiber delay, L_c is the coherence length, c is the speed of light in vacuum, n is the refractive index of the fiber (1.47) and $\Delta\nu$ is the linewidth of the laser i.e. FWHM. Having the fact, that the linewidth is related inversely to the coherence length, therefore lower linewidths require higher coherence lengths to achieve the uncorrelation condition. Hence, in order to achieve uncorrelated waves at the PD, this technique is limited by the coherence length and therefore is not sufficient for linewidth measurement below several kilohertz's. For example, for 1 Hz *LUT* linewidth, the required fiber delay length is 65000 km. However, a recirculating fiber loop could be used by which the light will have many round trips in the optical fiber [91].

4.4.3 Delayed Self-Homodyne (Measurement at the Base Band)

The delayed self-homodyne method is similar to the delayed self-heterodyne method except it does not need a frequency shifter. Several optical delayed self-homodyne setups are reported in [90], for instance. The PD will couple two optical fields; these two fields are one as an exact copy of the other. Eq. 4.14c should be satisfied for the appropriate measurement.

Referring to Fig. 4.8, and because the two fields have about the same frequency, the beat note will be measured at the base-band of the ESA. This method is suitable for wide laser linewidths estimation in the Megahertz range, for instance. In principle, the frequency shifter is used for the delayed Self-Heterodyne technique to get a beat note at a frequency difference between the two waves and to avoid measuring at the base band, therefore get rid of the lower frequency limitation of the ESA.

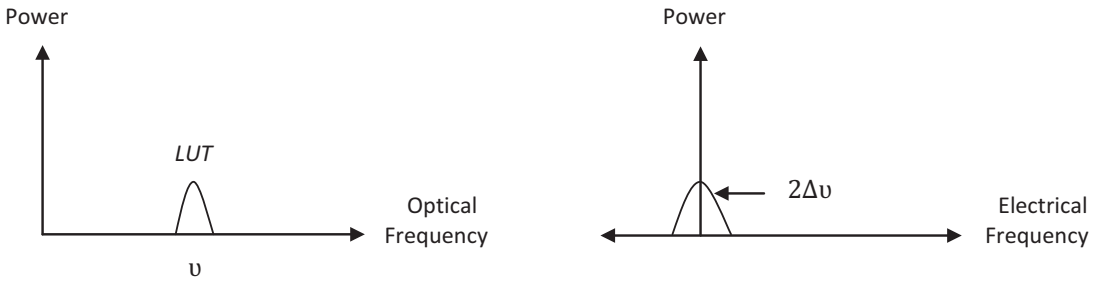

Figure 4.8: Self-Homodyne process illustration of the *LUT*.

4.5 Experimental Setup and Results

Fig. 4.9 shows the experimental setup that had been used to extract a high quality single line out of a MLFL . The high quality MLFL (Toptica FemtoFErb 1560) is used to produce the frequency comb. The frequency comb spectral density out of the MLFL is shown in Fig. 4.10. The spectral width of the MLFL at 20 dB bandwidth was about 90 nm, and the repetition rate was 100 MHz as shown in the 1 GHz span inset of Fig. 4.10. In principle, the high bandwidth of the MLFL is very useful for many applications. Nevertheless, many efforts had been paid to broaden the comb bandwidth by utilizing a hybrid highly non-linear fiber such as photonic crystal fibers and UV-exposed fibers, for instance. Therefore, an octave-spanning (doubling) continuum had been reached [92].

As explained earlier, no conventional optical filter can be used to filter one spectral line out of the produced frequency comb, since the frequency spacing between each two neighboring spectral lines is less than the minimum bandwidth of any conventional optical filter. Therefore, we utilized the previously explained non-linear effect of PPA-SBS which has a bandwidth of 10-30 MHz to extract one line out of the frequency comb. However, methods had been reported to reduce that bandwidth down to about 3 MHz [93, 94].

Referring to Fig. 4.9 (a) which depicts the MLFL frequency comb optical spectral lines, a wave shaper (WS) was utilized to pre-filter only 10 GHz bandwidth of the frequency comb, i.e. around 100 residual spectral lines were filtered out of the MLFL as illustrated in Fig. 4.9 (b). Therefore, a higher signal to noise ratio (SNR) was provided to the following Erbium doped fiber amplifier (EDFA1) which was set to 7 dBm

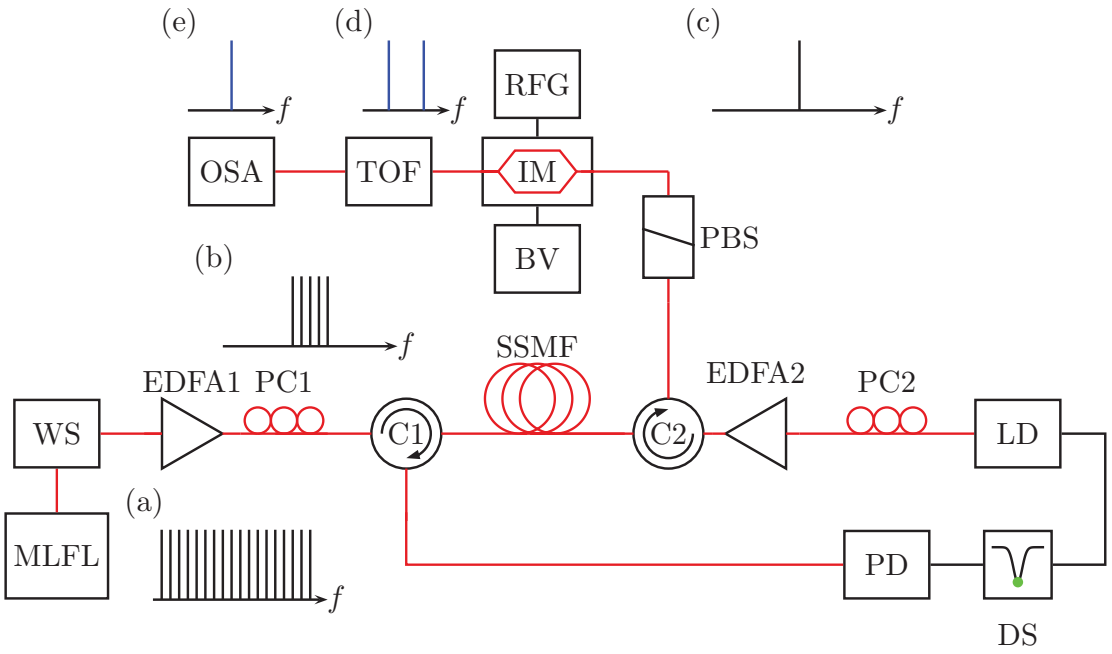

Figure 4.9: Experimental setup. red, black lines: optical, electrical connections. WS: wave shaper, EDFA: Erbium doped fiber amplifier, PC: polarization controller, C: circulator, PD: photo diode, DS: dip search, LD: distributed feedback laser diode, BV: bias voltage, IM: intensity modulator, TOF: tunable optical filter, OSA: optical spectrum analyzer, RFG: radio frequency generator, Comp: computer and FC: frequency counter.

output power. According to the previously explained PPA-SBS non-linear effect, the pre-filtered 100 spectral lines will be treated as a signal. Therefore, a polarization controller PC1 was used to control the SOP of the signal which was injected into the SSMF by port 2 of C1. A 50 km long SSMF was used to achieve the PPA-SBS non-linear effect in order to discriminate only one spectral line out of the pre-filtered frequency comb lines.

To achieve the PPA-SBS non-linear effect, the LD was utilized as a pump source. Whereas, the SOP of the pump wave was controlled by PC2 and aligned to amplify only one line out of the signal and the pump power was set to 13 dBm out of EDFA2. The pump wave was coupled into the other end of the SSMF via port 2 of C2. A dip search (DS) (will be explained in details in the next chapter) was used to lock the LD to the desired spectral comb line. Thus, a stabilization and monitoring of the desired amplified line was achieved.

In principle, and as explained earlier the polarization controllers PC1 and PC2 play a great role to suppress all unwanted spectral lines via PPA-SBS. Therefore, the two polarization controllers were carefully adjusted to get maximum amplification for the desired spectral line and suppress the others which are unwanted. Hence, the SOP of the desired spectral line was orthogonal to the SOP of the unwanted lines and has the same SOP as the pump wave. Thereby, the undesired lines will be blocked at the polarization

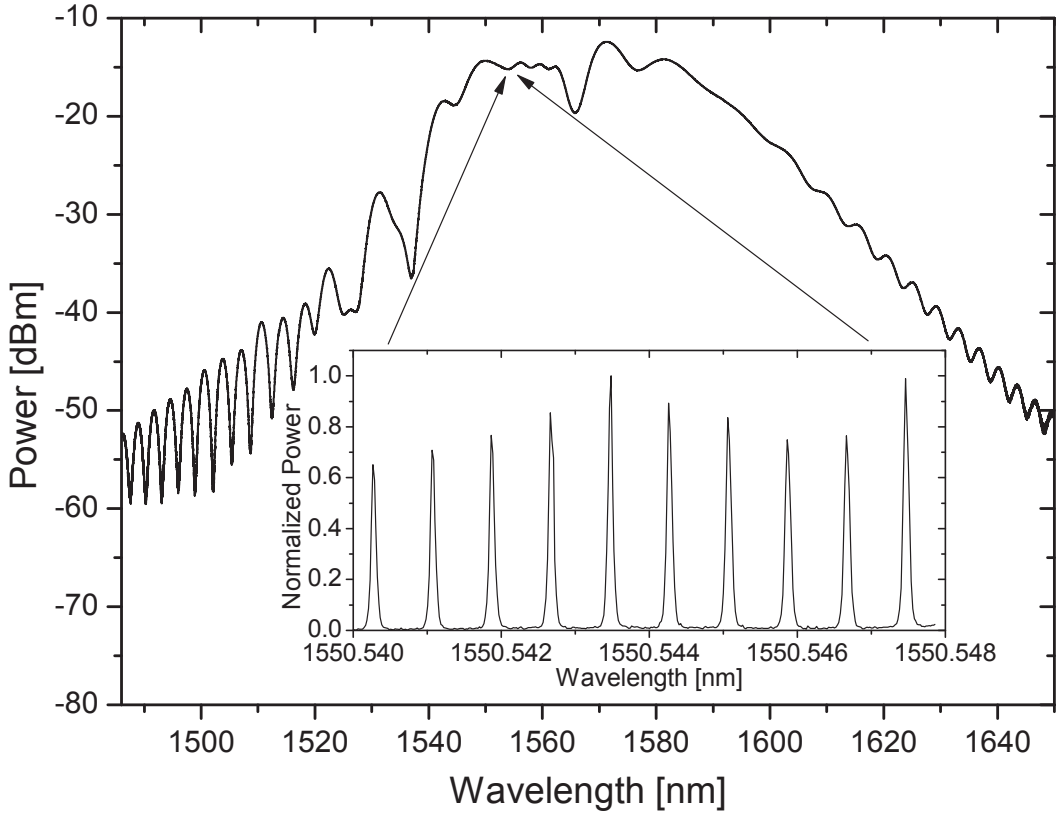

Figure 4.10: Optical Spectrum of the fs-laser measured with a conventional OSA, the inset shows a 1 GHz part of the fs-laser spectrum measured with a high resolution OSA [95].

beam splitter (PBS).

Fig. 4.11 shows the schematic diagram of the PBS which is a kind of optical filter by which light transmission or reflection depend mainly on the SOP of the incident light. In principle, if a randomly polarized (R-polarized) light ray propagates through a PBS, it will be split into two orthogonal linearly polarized components. The senkrecht (German origin) polarized (S-polarized) is reflected at 90^0 angel to the plane of incidence, which is illustrated by a black dot in Fig. 4.11. Whereas, the other component is transmitted parallel to the plane of incidence (P-polarized). Each PBS consists of a pair of precision high tolerance right angle prisms cemented together with a dielectric coating such as: polyester, epoxy, or urethane-based adhesives (the blue line in Fig. 4.11) on the hypotenuse of one of the prisms. In principle, the thickness of the resin layer is designed in a way that for a certain wavelength half of the incident light with a specific SOP is reflected due to total internal reflection and the other half with the orthogonal SOP is transmitted.

In principle, the pump and signal SOP were aligned carefully to each other with respect to the PBS by the maximum amplification OSA monitoring of the signal. Therefore, when the desired amplified spectral line (which is already pulled towards the SOP

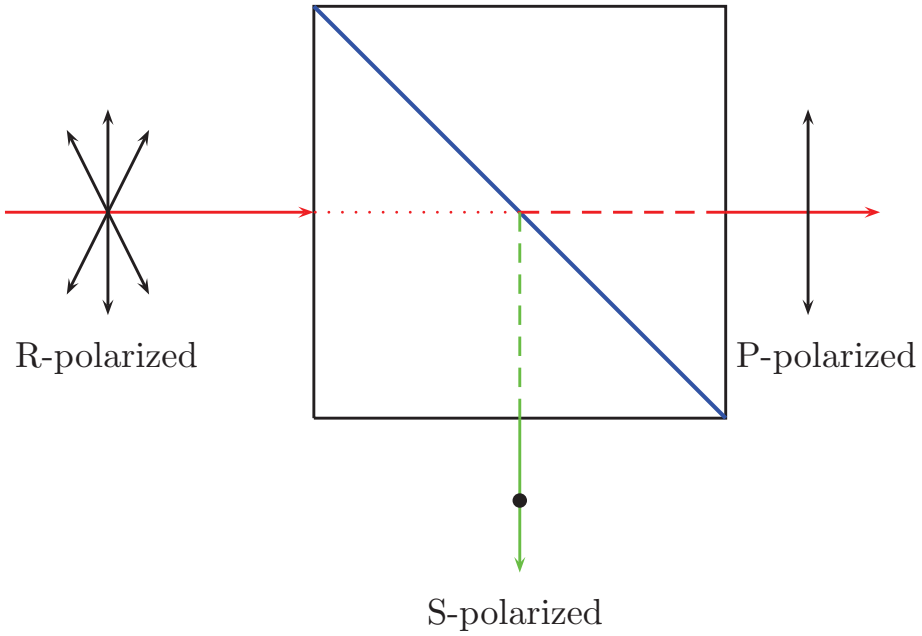

Figure 4.11: Polarization beam splitter.

of the pump via PPA-SBS) and the other unwanted spectral lines pass through the PBS, they will be totally separated. Hence, the unwanted lines will be blocked entirely by the PBS while the desired spectral line will be extracted.

Fig. 4.12 shows the optical spectrum of the extracted spectral line out of the frequency comb as well as the pre-filtered frequency comb using an optical spectrum analyzer with a resolution of 4 GHz. The blue curve refers to the pre-filtered frequency comb by the WS and the spectral line that amplified by SBS. Whereas, the black curve refers to the discriminated spectral line via PPA-SBS. Therefore, the remaining frequency comb components were suppressed below the noise level. The extracted line was centered at a wavelength of 1550.8268 nm and had a signal to noise ratio (SNR) of about 67 dB.

Referring to Fig. 4.9, the discriminated spectral line was depicted by (c). For the linewidth measurement of the discriminated spectral line, a delayed Self-Heterodyne technique was utilized. An intensity modulator was used to achieve the frequency shifting between the two ways. According to Eq. 4.11, two optical fiber lengths 65 and 70 km were used for delaying the non-frequency shifted way to perform the uncorrelated condition with the other way. An optical filter was used to suppress the remaining carrier and one of the sidebands, therefore mixing only one sideband with the delayed way at the photo diode took place. A beat note linewidth was measured with 2 kHz, therefore and as mentioned earlier the real linewidth of the extracted line was 1 kHz, see Fig. 4.13.

In order to get a high quality stable and tuneable single line besides the narrow linewidth, an IM is utilized to modulate the extracted spectral line. The IM was driven

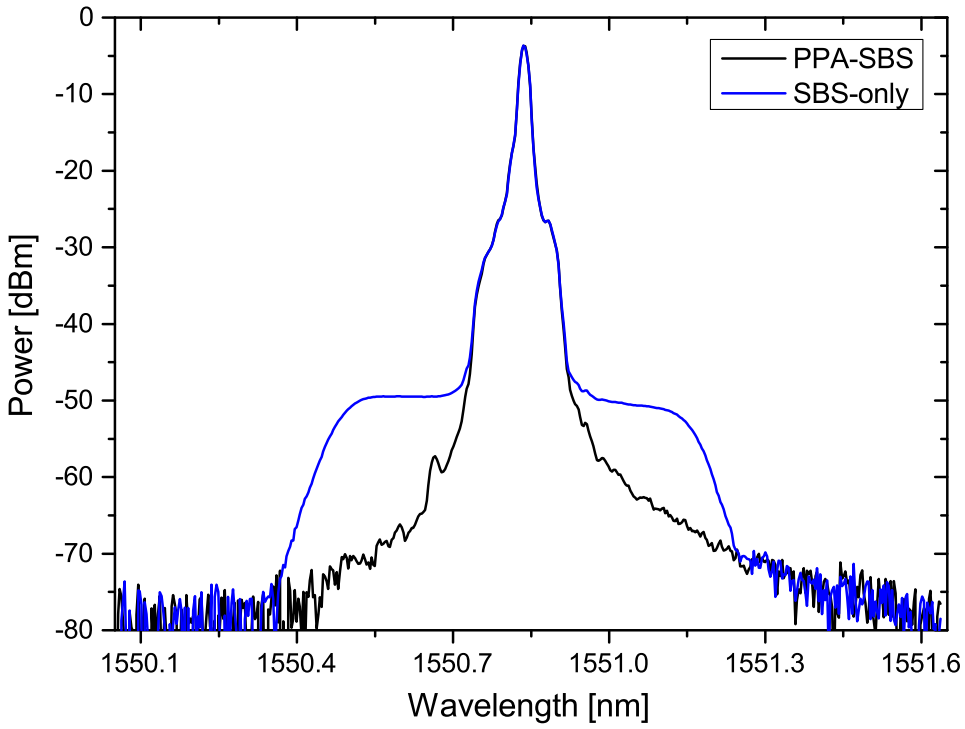

Figure 4.12: Optical spectrum of the pre-filtered comb with a single line amplified by SBS (blue) and the suppression of the unwanted components through PPA-SBS (black). Please note that the linewidth of the spectral component is much narrower than the resolution bandwidth of the OSA.

in the carrier suppressed regime as illustrated in Fig. 4.9 (d). Therefore, the BV was set to 0.84 V_π (3.2 V) and the RFG had been set to 17 dBm electrical output power. As consequence, only the first order sidebands had been achieved. As illustrated in Fig. 4.9 (e), a TOF was utilized to filter only one sideband. The TOF had a bandwidth of 10 GHz, therefore the modulation offset frequency was set to 5-20 GHz limited by the TOF and the IM bandwidths.

In order to show the ability for tuning the selected spectral line, it was modulated with 4 randomly chosen frequencies restricted by the 20 GHz bandwidth modulator. Fig. 4.14 shows the optical spectrum of the modulated line with 5, 10, 15 and 20 GHz, the SNR was 47 dB at a limited conventional OSA resolution of 4 GHz. However, a very delicate tuning can be achieved for full MLFL bandwidth by both: coarse and precise tuning of the extracted spectral line. For example, when the pump wave is shifted by changing the laser diode current and locking to another spectral line via the DS technique, then a coarse tuning will be achieved with a step of 100 MHz. Whereas, with the

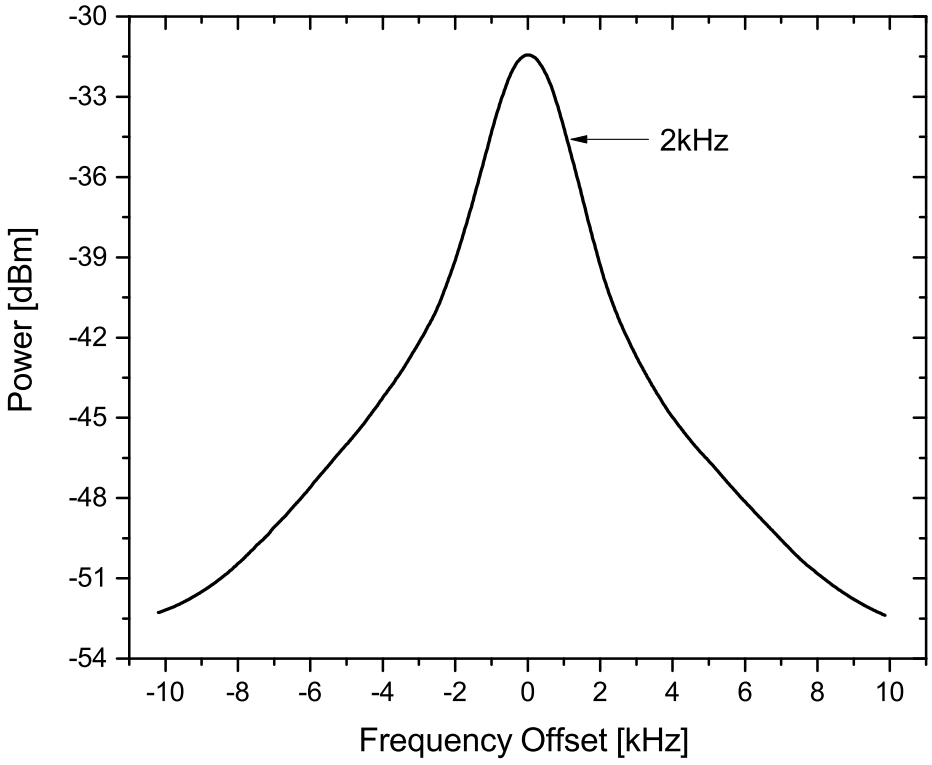

Figure 4.13: Measured linewidth of the generated single line via delayed Self-Heterodyne technique.

offset modulation frequency one can fine tune the selected spectral line down to 1 mHz, depending on the used ESA.

Additionally, a 20 dBm power difference between Fig. 4.12 and Fig. 4.14 can be noticed. In principle, that is due to the insertion loss of both the TOF and the modulator. Consequently, a single sideband modulation with a suppressed carrier regime can be used to avoid the utilization of the TOF. Therefore, the optical SNR of the discriminated and modulated spectral line can be improved.

To prove the stabilization concept (will be discussed in details within the next chapter) and get rid of the repetition rate drift of the MLFL due to the temperature changes and therefore stabilize the alteration of the extracted line relative frequency, the repetition rate was measured via the electrical MLFL output and a frequency counter (FC). In principle, the repetition rate was adapted as follows: the FC will measure the instantaneous repetition rate out of the MLFL, then that value will be compared to the ideal repetition rate value (100 MHz) via a computer software (Comp) as illustrated in Fig.

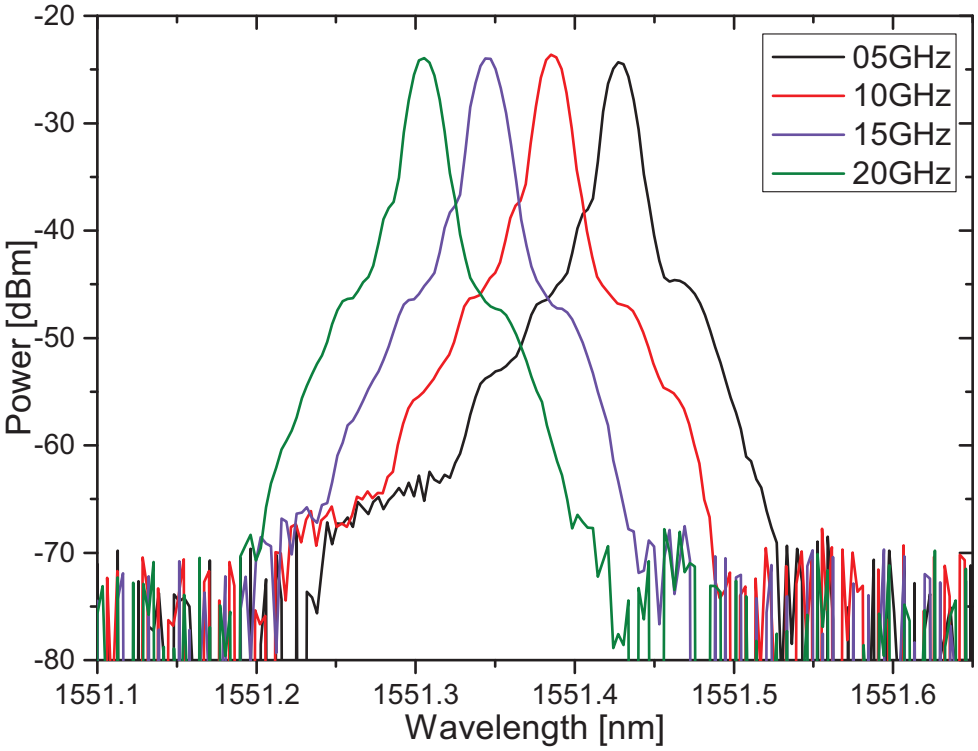

Figure 4.14: Tuning of the discriminated line by different modulation frequencies.

4.9. The adaption value will be provided to the RFG to set the adaption frequency offset for the IM. For example, if the repetition rate is increased then the adaption frequency offset will decrease and vice versa. Therefore, the resultant sideband (single line) frequency will be adapted depending on the repetition rate alteration.

Fig. 4.15 shows the heterodyne beat note between the adapted spectral line with an other extracted line out of the frequency comb. The 10 dB power difference between Fig. 4.13 and Fig. 4.9 is due to the power loss within the IM and TOF.

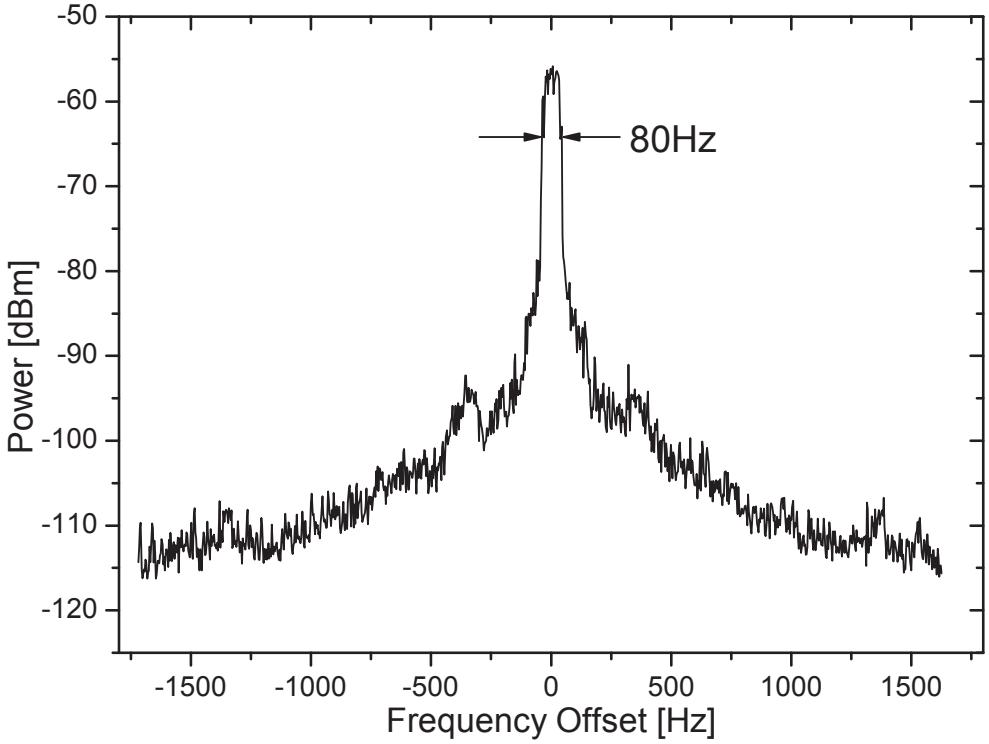

Figure 4.15: Frequency shift of the heterodyned stabilized laser line and other spectral comb line at a PD over 5 hours.

The beating frequency was centered at 24.63937142 GHz, i.e. there were 246 lines between the two mixed lines at the PD, and the drift was about 80 Hz over 5 hours. Consequently, the residual single line drift can be found by dividing the overall frequency drift over the number of lines in between, i.e. 246. Thus, the resultant residual spectral line drift was ± 160 mHz.

4.6 Summary

The experimental setup is based on a stable, easy to operate, small footprint, light-weight and cost-effective MLFL as well as standard optical communications equipments. A highly stable, widely tuneable and extremely narrow single line laser was proposed and experimentally demonstrated. The precise stability of the extracted spectral line had been achieved via measuring the repetition rate drift of the MLFL and an adaptation of the modulation frequency offset. Hence, the residual spectral line drift was ± 160 mHz. However, the utilized stabilization technique was limited down to 100 mHz registration value by the accuracy and the read out time of the FC. Therefore, during the stabilization process if faster repetition rate changes out of the MLL take place, then it cannot be captured. Thus, by a direct generation of the modulation frequency depend-

ing on the directly measured repetition rate out of the MLFL with an analog circuit, that residual frequency drift could be largely reduced within the limits of the electrical components [96]. Additionally, changing in the absolute frequency of the extracted line could take place as well due to the whole laser drift. Nevertheless, in [97] several well known methods for femtosecond laser stabilization were reported.

The tuneability concept was proved via modulation frequency offset by randomly choosing values limited by the modulator and the TOF. However, the discriminated single line laser can be easily tuned over the whole C-band via coarse and fine tuning, as well as a tuneability over S-and L-bands could be achieved via non-linear comb broadening. A linewidth of 1 kHz was measured as well as 47 dB SNR was achieved at a 4 GHz resolution OSA.

The high quality optical frequency comb out of the MLFL has wide application fields like: synthesis of ultra-purity optical and RF frequencies, metrology and precision spectroscopy. The optical frequency comb out of the Toptica FemtoFErb 1560 femto-second laser was utilized to extract a high quality single spectral line. The PPA-SBS non-linear effect was utilized as a sharp optical filter and amplifier to discriminate a high quality single spectral line out of the optical frequency comb. The principle of operation of the PPA-SBS non-linear effect was explained. Additionally, several linewidth measurement techniques were presented with their advantages and disadvantages. The delayed Self-Heterodyne was utilized to measure the linewidth of the extracted spectral line.

The implementation of the experimental setup for the single spectral line extraction, linewidth measurement, tuneability and stabilization were presented in detail. Among thousands of spectral frequency comb lines only one line was discriminated via the PPA-SBS non-linear effect. The linewidth measurement of 1 kHz was achieved by the delayed Self-Heterodyne technique. The fine tuneability with optical SNR of 47 dB was done by the modulation, whereas the coarse tuning could easily be achieved by selecting another spectral line out of the frequency comb via PPA-SBS and therefore pump wavelength tuning would be necessary. The residual stabilization of $\pm$ 160 mHz for the extracted laser line was achieved by measuring the repetition rate out of the MLFL electrically and adapting it via computer software and modulation frequency.

The high quality and wide tuneability of the generated single line laser, shows high potential for many applications in the field of optical communications with spectral efficient modulation formats and for ultra-high resolution spectroscopy.

Chapter 5

High Quality Millimeter Wave Generation

5.1 Introduction

The millimetre length electromagnetic waves were first investigated within the 1890s by pioneering Indian scientist Jagadish Chandra Bose. These waves travel just through line-of-sight and are blocked via building walls and attenuated by foliage as well [98]. In principle, the millimeter (30 - 300 GHz), i.e. (1 cm - 1 mm) and sub-millimeter or THz band (0.3 - 3 THz) of the electromagnetic spectrum has great potential for various scientific and engineering applications like photonic analog-to-digital converters [99], local oscillators for fountain clocks [100], high performance antennas and radars, high speed wireless communications, and high-resolution signal analysis. In wireless communications for instance, the frequency bands above 300 GHz are unused and offer large bandwidths for transmissions up to the TBits/s range [101]. Additionally, the wide band provides a valuable support for video distribution and high speed data [102].

Usually, electrical oscillators are used for the generation of electrical waves in the MHz and GHz range, frequencies up to 100 GHz are actually possible. These frequencies can be transferred into higher frequency ranges via electronic up conversions, the millimeter and sub-millimeter range, for instance. Unfortunately, the electronic upconversion generates a phase noise which scales quadratically with the harmonic frequency order due to the non-linear mixing processes [103]. Thus, millimeter wave generation with low phase noise is challenging via electronic methods.

A more convenient approach for the millimeter wave generation is the heterodyning and optoelectronic conversion of two optical waves in an appropriate non-linear element such as a non-linear crystal or a PD. For example, optical heterodyning of two independent laser sources is the simplest way to generate mm-waves with wide frequency tuneability. In [104] for example, a beat note of about 3.3 MHz linewidth was reported

by heterodyning a DFB and external cavity laser diodes. The beat note had a frequency range of 3 - 11 GHz and a stability of higher than 1 MHz. However, a phase locked loop is required in order to reduce the phase noise of the generated mm-wave, which leads to a complex and expensive method. Nevertheless, the two optical waves need to be correlated in order to achieve high quality millimeter waves with low phase noise.

In principle, the two optical waves are automatically correlated, if they are generated by the same source, e.g. a dual mode structured DFB laser diode. However, the tuneability of these devices is very limited since the limitation of the laser diode current tuning and therefore the limited wavelength tuning. In [105] for instance, the tuneability of this technique was limited to 320 GHz. Additionally, the stability of the generated millimeter wave depends on the temperature controller of the DFB laser diodes. A frequency stabilization technique is reported in [106], an optical delay line was utilized as a frequency reference instead of a millimeter wave oscillator. That method was limited to a deviation of 12.3 MHz sub-carrier in a 40 GHz band using commercial DFB laser diodes. Additionally, the multi frequency generation via external modulation of a narrow linewidth laser can be utilized. In [107] for example, the filtering of two modes from a multi-frequency optical source was reported. By the separation with an arrayed waveguide grating and subsequent heterodyning of such a source, a phase noise of -75 dBc/Hz at an offset of 100 Hz from the carrier and a linewidth of 300 Hz could be achieved [107].

Nowadays, sources that provide a numerous amount of phase locked frequencies are frequency combs. Especially, the combs generated by a mode locked fiber femtosecond laser (MLFL) gives a high potential to generate millimeter and sub-millimeter waves with extraordinary quality. Via optical filtering of two modes out of the MLFL comb spectrum, frequencies up to the THz range (or up to the photodiode bandwidth) can be generated. A phase noise of -105 dBc/Hz at an offset of 10 kHz from the carrier and a linewidth of 300 Hz has been presented for frequencies up to 110 GHz [108]. Additionally, the stability of the optically produced millimeter wave is important for many applications like a local oscillator, as carrier for communications or as an RF signal.

In most cases the optical filters and fiber couplers are connected with optical fibers, and the generated mm-wave show phase fluctuations, as well as, the phase noise at low frequencies becomes relatively high because the optical path length difference between the filter and coupler changes due to temperature fluctuations and, as a result, the phase difference between the two modes changes. Additionally, the temperature changes of the laser cavity lead to changes in the repetition rate of the MLFL, which in turn leads to a broadening or shrinking of the comb and therefore to a frequency drift of the generated mm-wave. Thus, many efforts had been demonstrated to stabilize the repetition rate change of the MLFL such as stretching the fibers by a piezoelectric actuator, refractive index changing and pump power control of the gain fiber [109, 110, 111], respectively. However, a technologically challenging laser cavity interaction is needed in these cases. Therefore, in this chapter a simple technique will be presented and experimentally demonstrated for the generation and stabilization of a millimeter wave. The millimeter wave was generated by the extraction of two spectral lines out of the MLFL frequency comb

and both were mixed at a proper PD. The stabilization was achieved by the stabilization of the MLFL repetition rate via two approaches: analog and software, without an interaction with the laser cavity, and therefore the generated millimeter wave was stabilized as well. Thus, one of the optical waves is externally modulated and adapted at the inverse of the repetition rate drift. An analog and software approach for the generation of the modulation signal are presented and compared.

This chapter is organized as follows: the description of mm-wave generation from the mixing of two optical waves as well as the phase noise are presented. An elegant method to generate and stabilize a high quality mm-wave with low phase noise via extracting two spectral lines out of a frequency comb is explained. Then the experimental setup and results are presented.

5.2 Millimeter-Wave Generation by Mixing Two Optical Waves

Currently, the mixing and optoelectronic conversion of two optical waves at a proper PD is a widely used method for the generation of mm-waves. Fig. 5.1 illustrates the mixing of two different optical frequencies at a non-linear element (PD), the gray arrows are referring to the frequency drifting.

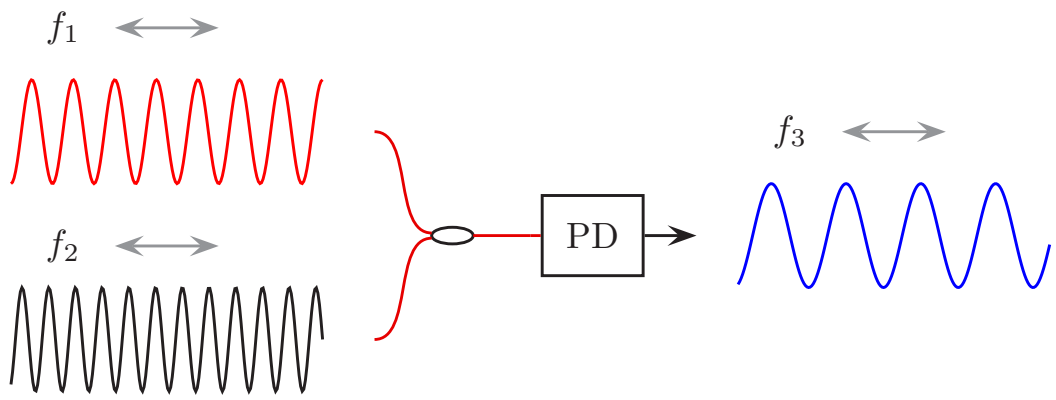

Figure 5.1: Schematic diagram for mm-wave generation by difference frequency generation. The two optical fields are heterodyned at a photo diode (PD).

Referring to Fig. 5.1, the electrical fields of the two optical input waves (f_1, f_2) can be written as [90]:

$$E_1(t) = |E_1(t)| \cos(\omega_1 t) \tag{5.1a}$$
$$E_2(t) = |E_2(t)| \cos(\omega_2 t + \phi) \tag{5.1b}$$

where ϕ is the phase of the second optical field. In principle, the phase is related to the laser phase noise as well as the frequency modulation. The detected power at the PD can be written as follows:

$$P(t) = |E_T(t)|^2 \tag{5.2}$$

where $E_T(t) = E_1(t) + E_2(t)$ is the total electric field at the PD. Let's assume that $E_1(t)$ and $E_2(t)$ are the local oscillator $E_{LO}(t)$ and signal $E_S(t)$ electric fields, respectively. In principle, the PD will detect only the total power $P(t)$, not the optical fields themselves. Thus, one can get the two fields interference at the PD. These two waves will be converted from the optical domain to the electrical domain. The resultant photo-current from the overlapped two optical fields will be [90]:

$$\begin{aligned} I(t) = \frac{E_S^2}{2}(1+\cos(2\omega_S t + 2\phi)) + \frac{E_{LO}^2}{2}(1+\cos(2\omega_{LO} t)) \\ + E_S E_{LO}[\cos((\omega_S+\omega_{LO})t+\phi) + \cos((\omega_S-\omega_{LO})t+\phi)] = \\ \underbrace{\frac{E_S^2+E_{LO}^2}{2}}_{constant\ component} + \\ \underbrace{\frac{E_S^2}{2}\cos(2\omega_S t+2\phi) + \frac{E_{LO}^2}{2}\cos(2\omega_{LO}t) + E_S E_{LO}\cos((\omega_S+\omega_{LO})t+\phi)}_{high\ frequency\ component} \\ + \underbrace{E_S E_{LO}\cos((\omega_S-\omega_{LO})t+\phi)}_{beat\ component} \end{aligned} \tag{5.3}$$

$$R = \frac{\eta q}{h\nu} \tag{5.4}$$

where ω_S and ω_{LO} are the signal and local oscillator frequencies, respectively, R [A/W] is the photo diode responsivity, η ($0 < \eta \leq 1$) is the PD quantum efficiency, which is a measure of the incident photons to electrical charge conversion efficiency, q is the electronic charge (1.6021×10^{-19} C) and $h\nu$ is the photon energy. However, the main disadvantages of this method is the limited bandwidth of the PD, thus frequency difference between the local oscillator and the signal and therefore the resultant electrical wave frequency should be within the PD bandwidth. The first term in Eq. 5.3 is referring to the direct intensity detection (constant component) of $E_{LO}(t)$ and $E_S(t)$, the second term is the high frequency component. However, the third term is the heterodyne term which is the important mixing term in Eq. 5.3. Additionally, the optical field itself will be not detected since at the PD the power will be detected not the field. Due to the PD bandwidth, only the difference frequency product (mm-wave term) will be detected

while both, the first and the second terms are filtered out.

One of the main factors that the mm-waves and therefore oscillators quality can be described by is the phase noise (PN) which is expressed in units of dBc/Hz [112]. The PN is the frequency domain representation of rapid, short-term, random fluctuations in the phase of a wave spectrum, resulting from the time domain instabilities (jitter). In other words, PN defines the noise power relative to the carrier contained in a 1 Hz bandwidth centered at a certain offset from the carrier [113]. A certain carrier for instance, may have a PN of -90 dBc/Hz at an offset of 10 kHz. However, at 100 kHz the PN may be equal to -100 dBc/Hz. In [114] for instance, a mm-wave of -79 dBc/Hz at 10 kHz carrier offset PN was reported. The mm-wave of frequency 10-100 GHz was generated by a combination of an optical frequency comb generator, an optical injection-locking filter, and a unitraveling-carrier PD. However, for N5181A keysight-agilent radio frequency generator, the reported PN was -121 dBc/Hz for a 1 GHz frequency and 20 kHz offset [115].

In principle, local oscillators noise in transmitters is amplified via the subsequent amplifier stages. Thus, it will be fed to the antenna with the desired signal. As consequence, the desired signal will be surrounded by a strap of noise that comes from the local oscillator phase noise. Hence, the noise will spread over several kHz and cover nearby lower power signals.

5.3 Millimeter-Wave Generation and Stabilization

The basic principle of the generation and stabilization of high quality millimeter waves is shown in the block diagram of Fig. 5.2 (a).

The frequency comb is generated by a MLFL (Toptica FemtoFErb 1560) which has a bandwidth of more than 12.4 THz and contains equidistant spectral lines with a repetition rate of 100 MHz as described in the previous chapter. The generation principle of the millimeter wave is based on heterodyning two spectral lines out of the MLFL. The generated signal frequency is determined by the frequency difference between these lines. In order to select two lines out of the frequency comb, two narrow band optical filters are required, as illustrated in Fig. 5.2 (b). Thus, the non-linear effect of polarization pulling assisted stimulated Brillouin scattering (PPA-SBS) is utilized as a filter and amplifier [83, 85, 24]. As explained in the previous chapter, the SBS bandwidth is with 10-30 MHz which is lower than the frequency difference between any two neighboring modes of the MLFL. Therefore, any two optical waves can be separated clearly. However, the bandwidth of PPA-SBS can be reduced down to 3 MHz if required [94, 93, 69].

In principle, the MLFL thermal changes lead to a repetition rate drift, therefore the generated frequencies will be changed over time. However, the drift value could be increased as much as the frequency difference between the selected spectral lines increased

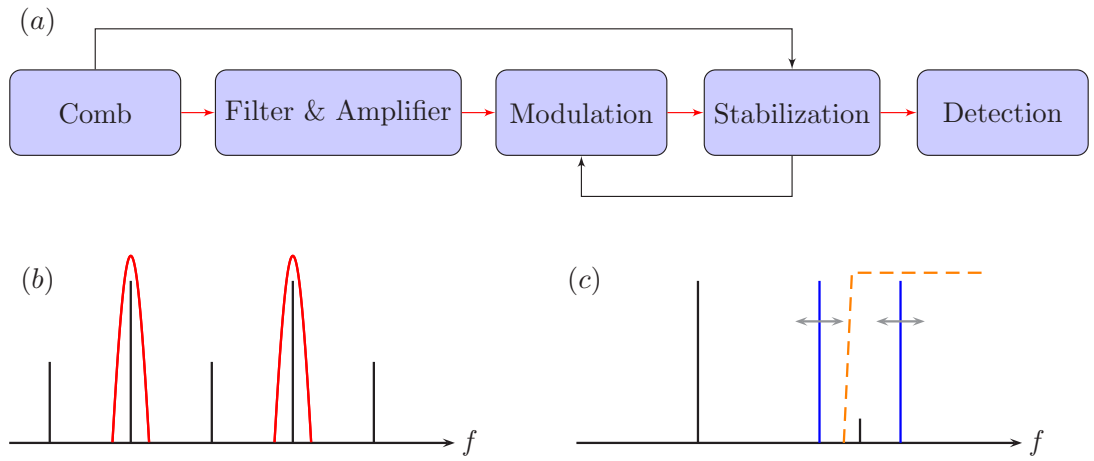

Figure 5.2: (a) block diagram for the generation and stabilization of millimeter waves, red: optical, black: electrical connections. (b) extraction and amplification of comb lines. (c) modulation and filtering for the stabilization.

i.e. more number of lines in between. Additionally, the mm-wave fine tuning is very important for several applications especially for radar. Therefore, for the stabilization and fine tuning of the generated millimeter waves, one of the extracted lines will be modulated. A tuneable optical filter (TOF) is used to filter one of the modulated sidebands in order to avoid unwanted mixing products, which is illustrated as a dashed orange line in Fig. 5.2 (c). Finally, this sideband is then mixed with the unmodulated line at a proper PD and the stabilized mm-wave is generated. The down converted electrical wave will be detected with an electrical spectrum analyzer (ESA). The detection block in Fig. 5.2 consists of a high bandwidth photo diode as non-linear element for the mixing and the ESA for the detection. The frequency for the modulation during the stabilization can be generated through various methods, e.g. with a radio frequency generator (RFG) controlled via software or by a voltage controlled oscillator controlled via an analog circuit, e.g. a phase locked loop.

5.3.1 Software Approach

The operating principle of the software stabilization is shown in Fig. 5.3. Basically, all the operations and calculations are carried out within a LabView program which controls a RFG that delivers the modulation frequency for the stabilization to the modulator.

First, the instantaneous repetition rate f_{rep} is read out of the electrical port of the MLFL through a frequency counter FC with a mHz resolution and maximum detection frequency of 150 MHz. Within the software it is assumed that the ideal repetition rate of the MLFL is 100 MHz. Subsequently, f_{rep} is compared with the ideal repetition rate and the line drifting Δf is calculated. In order to adapt Δf to the frequency of the desired

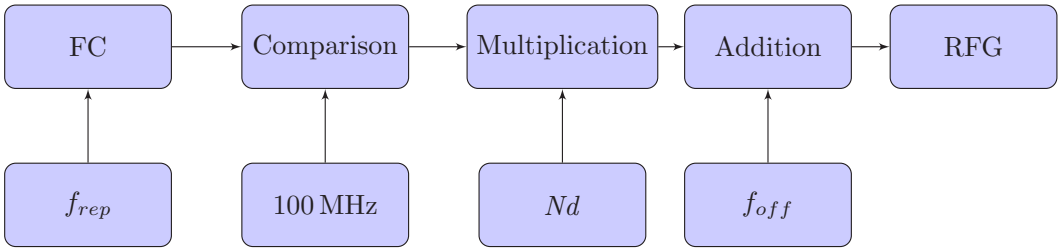

Figure 5.3: Block diagram for the software stabilization process.

mm-wave it will be multiplied with the number of lines Nd between the two selected ones.

If two extracted lines have a frequency difference of 20 GHz for instance, then Nd will be 199. The multiplication ($\Delta f * Nd$) leads to the adaption frequency for the stabilization. Afterward, an additional offset frequency f_{off} for the modulation is added in order to ensure appropriate alignment within the bandwidth of the TOF and fine tuning for the produced wave. Therefore, f_{off} has here a range of 5 - 20 GHz depending on the modulator and the TOF bandwidth. Finally, the software controls a RFG which provides the frequency to the modulator for the stabilization. In general, the modulation frequency can be calculated through $f_{mod} = (\Delta f * Nd) + f_{off}$.

The values of the theoretically assumed repetition rate and Nd should be defined initially within the software. Thus, the software will continuously adapt the modulation frequency and control the RFG. This guarantees that the frequency difference between the filtered sideband and the unmodulated line will be fixed at the PD.

5.3.2 Analog Circuit Approach

The analog circuit approach is based on a phase locked loop (PLL) and a voltage controlled oscillator (VCO) as shown in Fig. 5.4. In order to ensure a proper operation the multiples of the repetition rate are filtered electrically to obtain a single input frequency. The repetition rate is down converted with an electrical reference and a mixer in order to fit the input range of the PLL. The summation of the reference frequency and the input value of the PLL lead again to the ideal repetition rate (100 MHz) of the MLFL. Therefore, the reference frequency is here 70 MHz. This results in an intermediate frequency (IF) of (30 MHz $\pm$ Δf).

After the down conversion the signal is amplified to provide sufficient power for the PLL. Within the PLL the input frequency is passed through a phase detector which basically compares the input frequency with the feedback frequency. The phase detector provides an output error voltage which is passed on to a loop filter. The filter removes the high frequency noise and produces a steady DC level. The DC level is then passed on to a VCO. The output frequency of the VCO is directly proportional to the input signal. The output frequency of the VCO is about 12 GHz. Within the feedback path

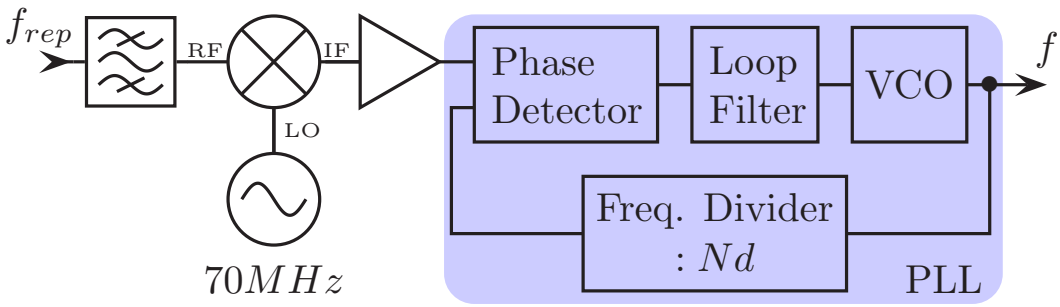

Figure 5.4: Operating principle of the analog circuit.

the output frequency of the VCO is divided by the number of lines *Nd*. Therefore, the feedback frequency fits again the input range.

Both, the input frequency and feedback frequency are compared and adjusted through feedback loops until the output frequency equals the input frequency. Thus, changes of the repetition rate are directly translated to a change of the VCO output frequency, which drives the modulator for the stabilization. Again, this leads to a very stable mm-wave after the down conversion of the two optical waves. To provide sufficient power for the modulator, the VCO output signal is amplified. Since the output range of the PLL is around 12 GHz there is no additional offset frequency necessary. The unwanted sideband of the modulation can be filtered out easily with the TOF.

5.4 Experimental Setup and Results

The experimental setup is shown in Fig. 5.5 [25]. As explained in the previous section, for the extraction of two lines out of the MLFL frequency comb, the non-linear effect of PPA-SBS is used [116] as illustrated in Fig. 5.5 (dashed box).

The frequency comb will be pre-filtered by a 10 GHz bandwidth wave shaper WS. The state of polarization (SOP) of the pre-filtered spectral lines (treated as a signal for the SBS process) will be controlled via a PC. The signal will be launched to the 20 km SSMF via port 2 of C1, while the two pump waves from LD1 and LD2 will be launched to the other end of the SSMF via port 2 of C2 and their SOP will be controlled via two polarization controllers PC.

In principle, in order to lock the two laser diodes LD1 and LD2 to the desired two spectral comb lines through the SBS process, an electrical dip search (DS) module, i.e minimum value detection was utilized [117]. Within SBS process and as explained in chapter two, the pump power will be transferred to the amplified signal. Therefore, a narrow band and fast PD1 was used to detect the pump power out of the SSMF via port 3 of C1. Thus, the DS module will trace the maximum pump power depletion (signal

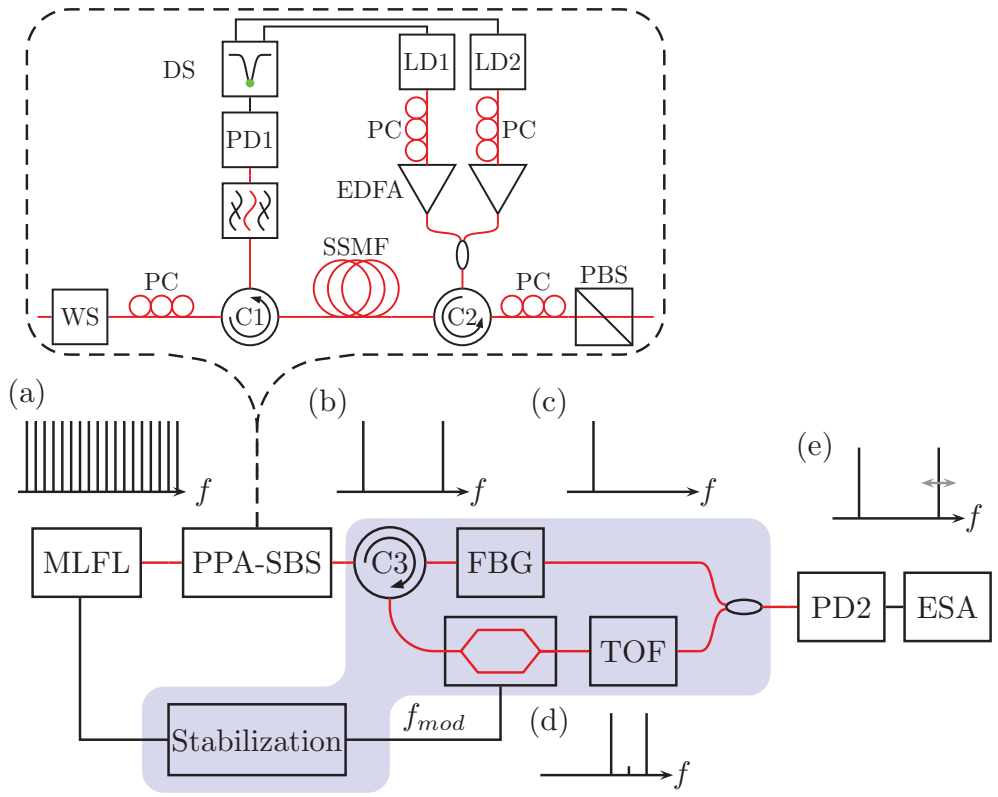

Figure 5.5: Experimental setup for the generation and stabilization of mm-waves with extraordinary quality. red, black lines: optical, electrical connections. MLFL: mode locked fiber laser, WS: wave shaper, PC: polarization controller, PD: photo diode, DS: dip search, C: circulator, SSMF: standard single mode fiber, LD: laser diode, EDFS: Erbium doped fiber amplifier, PBS: polarization beam splitter, PPA-SBS: polarization pulling assisted-SBS, FBG: fiber Bragg grating, TOF: tuneable optical filter, ESA: electrical spectrum analyzer and f_{mod}: frequency modulation. The dashed box shows the PPA-SBS in detail and the colored layer the additional components for the stabilization.

amplification) and provide the adapted signal (error signal) to automatically adjust the laser current of LD1 and LD2 via the current controller of the laser diodes. Therefore, the two pump wavelengths will change according to the regulation signal out of the DS module.

During the PPA-SBS process the state of polarization (SOP) of the amplified signal is drawn towards the SOP of the counter propagating pump wave. The unaffected signal components can be separated from the desired ones with the help of a polarization filter like a polarization beam splitter. Therefore, the polarizations need to be aligned carefully. The result of PPA-SBS are two single mode locked lines out of the frequency comb.
As long as the bandwidth of the PPA-SBS is lower than the repetition rate of the MLFL, any line can be extracted depending on the bandwidth of the polarizer. The pump waves

are locked to the desired comb lines by a minimum value regulation of the according pump depletion. Thereby, wavelength shifting of the pump laser diodes is produced by a current control feedback.

At the beginning, the extracted lines are directly coupled out of the PBS, mixed into a broadband PD and measured via the ESA. In this case unstabilized mm-waves are generated at 38.68940773 GHz, i.e the number of lines in between were 386 spectral lines. The drift of the generated signal is measured over 10 minutes, as can be seen in Fig. 5.6 (red curve). A frequency drift of 1300 Hz is shown, i.e. the repetition rate of the MLFL is changed with $\pm$ 1.68 Hz over that time interval, while a short term measurement (black) shows the 1 Hz linewidth of the mm-wave.

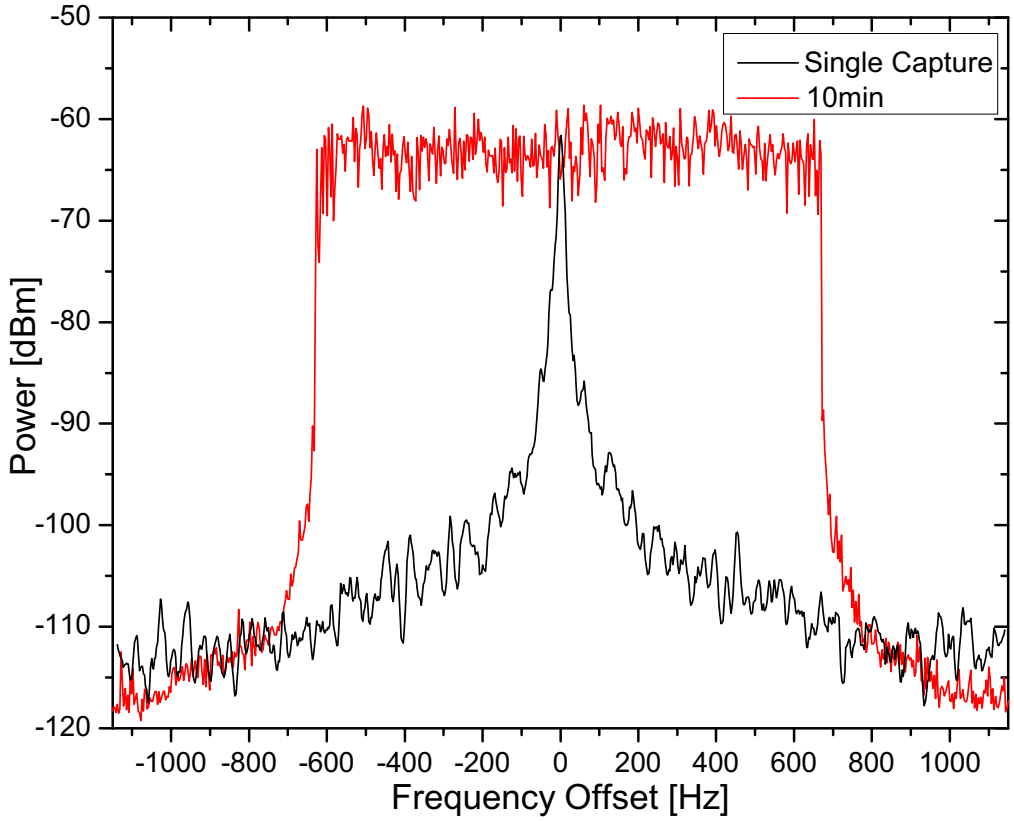

Figure 5.6: Frequency drift of the non-stabilized mm-wave over 10 minutes of 1300 Hz (red) and a short time mm-wave measurement with a 1 Hz linewidth (black). Both frequencies are normalized to the line center.

The main idea behind the stabilization (software and analog circuit) is to modulate one of the extracted lines with an adapted RF signal. Therefore, the extracted lines are coupled into a fiber Bragg grating (FBG) via the circulator (C3). The transmitted line out of the FBG will be coupled directly to the broadband PD2 in the detection part. The reflected line, coupled out via the circulator, will be modulated with an intensity

modulator which is driven in the carrier suppressed regime. As already mentioned, the modulation signal for the stabilization is generated with a software approach and with an analog circuit. After the modulation, one of the sidebands needs to be selected. Therefore, the signal is filtered by another optical bandpass filter (TOF). The filtered sideband and the unmodulated line of the frequency comb are combined with a 3 dB coupler and will be mixed in a broadband PD. The produced beat note, i.e. the stabilized millimeter wave, will be measured via the ESA.

Fig. 5.7 shows the long term stability, i.e. the frequency drift of the generated millimeter waves in both approaches, software (red) and analog circuit (black), limited by 1 Hz resolution bandwidth of an ESA.

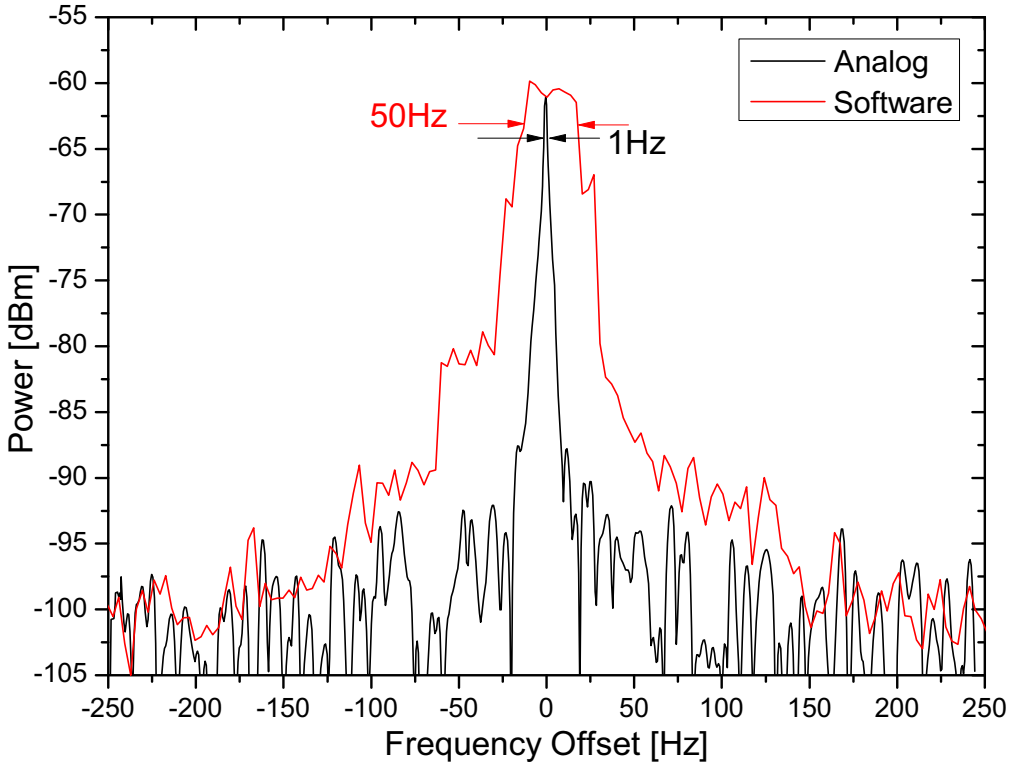

Figure 5.7: Frequency drift of the stabilized mm-wave over more than 40 minutes with the software (red) and the PLL (black).

The frequency drift within the software method over more than 40 minutes was 50 Hz. While the frequency drift for the analog circuit method was 1 Hz. Comparing to the unstabilized wave, the repetition rate and consequently the frequency drift is compensated. Therefore, the residual repetition rate drift of the MLFL is minimized to ±1.3 mHz for the circuit approach and ±6.4 mHz for the software solution, respectively.

Fig. 5.8 [25, 118] shows the phase noise of the generated millimeter wave for both methods, software (red) and analog circuit (black). The phase noise of the stabilized millimeter wave for the software approach was -134 dBc/Hz and for the analog circuit -58 dBc/Hz, both were measured at 10 kHz frequency offset.

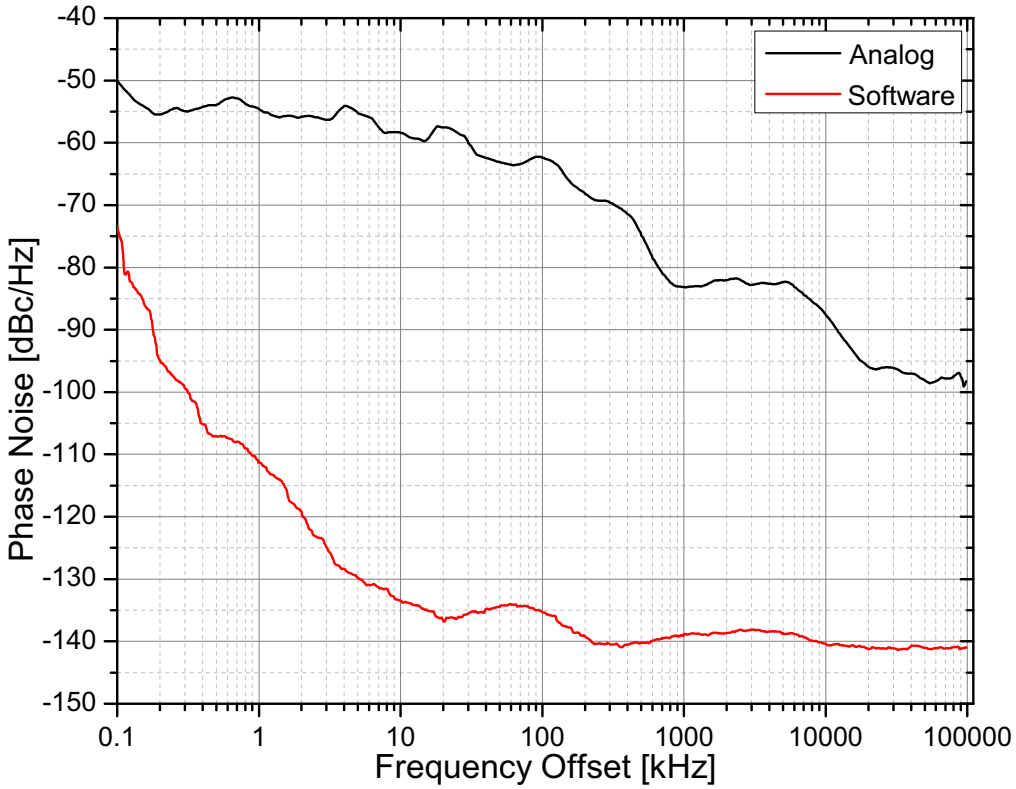

Figure 5.8: Phase noise measurement of the stabilized mm-wave with the analog circuit (black) and the software (red). The inset shows the stabilized mm-wave with analog and software: black and red, respectively.

5.5 Discussion and Concluding Remarks

The generation of the millimeter waves is demonstrated via heterodyning two spectral lines of a frequency comb in a proper photo mixer. The stabilization is achieved via externally modulating one of the lines, without an interaction in the laser cavity. Two approaches based on software and an analog circuit are investigated. A highly stable millimeter wave is produced via the software approach with a frequency drift of 50 Hz and a very low phase noise of -134 dBc/Hz. The mismatch for the stability and the phase noise results were due to the reading time as well as minimum resolution for the frequency counter and the internal noise of the electronic circuit, respectively. In principle, due to

the electronic limitation of the VCO, the phase noise of the analog circuit was higher which is transferred to the modulation. While the long term stability was 1 Hz. At any rate, this optical generation method provides high potential regarding the phase noise and stability in a comparison with electrical signal generation methods, especially for higher frequencies.

The two proposed mm-wave stabilization methods have their own benefits. However, the software stabilization technique for instance, had shown a much lower phase noise achieved by the high quality RFG. Additionally, lower stability had been got due to the limited resolution of the frequency counter and the slow read out rate, and therefore limited update rate of the software-based control loop had been took place. Additionally, the software-stabilization technique is very useful for communication systems, since its low phase noise. However, the 50 kHz drift range is insufficient, thus frequency stabilization by means of carrier recovery and synchronization mechanisms could be additionally utilized, by which they are inherent part of the receiver and demodulator.

In principle, both: software and analog circuit approaches could be improved to get rid of the low resolution of the frequency counter and the high phase noise of the VCO as well as the limited input and output range of the PLL and therefore the tuneability range. Hence, a high precision digital frequency counter or a higher quality VCO could be utilized. Additionally, the filtering of the mixing products is highly recommended to get proper operations, since spurious frequencies could take place. The FC, software processing and controlling could be combined at a micro controller or integrating with a field programmable gate array (FPGA) to get rid of the timing challenges and therefore the degradation of this method.

5.6 Summary

Highly quality millimeter-waves provide a great potential for several applications within scientific research, telecommunications, security screening and medicine. Therefore, a novel stabilization technique for the generation of mm-waves has been proposed and experimentally proofed.

A basic theory about two optical wave mixing at a non-linear element such as a photo diode to generate a proper RF signal was explained. Two spectral lines out of a high quality frequency comb produced by a femtosecond fiber laser were interfered to generate the millimeter-wave. One of the extracted lines was modulated to stabilize the millimeter-wave, and therefore any modulation information could be added to the modulated mode. Thus, the repetition rate drift could be overcame. Additionally, choosing variable wavelength laser modes from the MLFL permits flexible and tunable RF signals generation.

Two mm-wave stabilization approaches: software and analog were experimentally demonstrated that can produce high quality mm-waves. Within the software approach

for instance, a RF signal at a frequency of 38.6 GHz with a linewidth $<$ 1Hz and a phase noise of -134 dBc/Hz at a 10 kHz offset from the carrier was achieved. However, the stability was 50 Hz for about 40 min. The same linewidth was achieved within the analog circuit approach, whereas the stability was 1 Hz for the same time period and the phase noise was -58 dBc/Hz.

Chapter 6

Conclusions and Outlook

Conclusions

The aim of this thesis was to investigate the stimulated Brillouin scattering effect in silicon-on-insulator waveguides, as well as the experimental implementation of two of its applications had been presented. The SBS effect within SOI waveguides was studied through the derivation of the photo-elastic tensors and the Maxwells stress tensor which were used to simulate the opto-mechanical forces (electrostriction and radiation, respectively) inside the SOI waveguides. Four types of forces were presented and the overlap integrations had been taken into account with the elastic Eigen-modes to achieve the SBS gain profile. Each, electrostriction and radiation forces, have bulk and boundary contributions to the elastic Eigen-modes and therefore to the SBS gain profile. Two types of SOI waveguides were investigated: strip and rip, each with two cases: air and silica cladding. Both forward and backward SBS had been investigated for both waveguide kinds and cases. The simulations have revealed that many elastic Eigen modes contributed to a novel and high magnitude SBS gain. Additionally, it was found that only the symmetric SOI waveguide oscillations could contribute to the forward and backward SBS gain via the constructive interference between the optical forces.
Compared to the maximum SBS gain in SSMF which was about 2×10^{-11}m/W [7], the SBS gain in SOI waveguides is several orders of magnitude higher than in SSMF since the combination of the optical forces could contribute for both BSBS and FSBS. The SBS non-linearity in the SOI waveguide of about 100 μm length is equivalent to the SBS non-linearity in about 1 km length of the SSMF. Among the investigated SOI waveguide types and cases, the rib air cladding type had accomplished a significant BSBS peak gain value of 1.32×10^{4} $(\mathrm{m}\times\mathrm{W})^{-1}$. Therefore, within SOI waveguides new degrees of freedom can be created. The two-photon absorption was taken into account, showing a threshold of 30 mW for the investigated waveguides [53]. According to the presented calculations in table 3.1, a pump power as low as 50 mW can generate an SBS gain and omit the TPA effect. Thus, according to Eq. 3.24 for 50 mW pump power the power inside the

SOI waveguide is 26 mW.

The first proposed and experimentally demonstrated SBS application was the extraction and stabilization of a high quality single line out of the frequency comb of a fs-fiber laser. The frequency comb was containing thousands of equidistant and very narrow linewidth spectral lines. In order to extract one specific line out of the comb, it was pre-filtered by a wave shaper of 10 GHz bandwidth and subsequently processed by SBS. Due to its narrow bandwidth of about 10 MHz and the polarization pulling attributes, it enables the amplification of one single line and simultaneous suppression of unwanted signal components. Compared to the traditional optical filters and because of the 100 MHz frequency difference between any neighboring spectral lines, only the PPA-SBS non-linear effect can be used for such application. The PPA-SBS filter could be easily tuned by changing the pump wavelength and therefore coarse tuning could be achieved. In order to compensate the repetition rate drift and achieve fine tuning of the laser down to 1 mHz, the extracted line was processed by external modulation. The results for the software based stabilization show a FWHM linewidth of 1 kHz with a residual drift of $\pm$ 160 mHz. In comparison to a single longitudinal mode laser using spectral overlapping of two uniform fiber Bragg gratings with a linewidth of 5 MHz and a stability of 62.2 MHz [67], the achieved results show an increase in quality by three orders of magnitude and much higher regarding the stability.

The second proposed and experimentally demonstrated SBS application was the generation and stabilization of high quality millimeter waves. Thereby, two spectral lines were extracted by utilizing two independent PPA-SBS non-liner optical filters. In addition, two different techniques were used to stabilize the generated millimeter waves. The two filtered spectral lines were mixed at a proper photo diode and as a result of the opto-electric conversion, a millimeter wave was generated which was centered at the frequency difference between the two mixed spectral lines.
Compared to the typically used electrical oscillators for the electrical wave generation, optically generated millimeter waves can reach easily superior quality. A short term measurement of the generated wave had revealed a linewidth of 1 Hz. However, a long term measurement had shown a drift of 1.3 kHz due to the repetition rate drift. In order to overcome these impairment the generated wave was stabilized by a software and hardware approach. Through the software approach, a phase noise of -134 dBc/Hz at 10 kHz frequency offset and a stability of 50 Hz over several hours were achieved. Whereas, a phase noise of -58 dBc/Hz and a stability of 1 Hz could be accomplished with the electrical circuit. The low phase noise of the first approach was resulting from the used high quality radio frequency generator, while the high stability of the second method was resulting from the high speed reading and high resolution of the electrical circuit. The low stability of the first approach came from the reading time and resolution of the used frequency counter, while the high phase noise of the second approach came from the high electrical noise of the voltage controlled oscillator. Each technique has its own advantages for specific applications such as communication systems and medicine.

The center frequency of the achieved milli-meter wave was about 39 GHz, limited by the photo diode bandwidth. However, higher frequencies up to the THz-range could be

achieved easily by utilizing a photo diode with a larger bandwidth and selecting lines out of the comb with a larger frequency difference via different wavelength pumps for the PPA-SBS non-linear filters. Therefore, the method shows a high coarse tuning range of several tens of THz. Additionally, fine tuning is enabled by the earlier mentioned modulation of one extracted line.

Outlook

For the simulations there are different improvement suggestions for the future, that will be summarized below. The simulated waveguide types and cases could be experimentally demonstrated according to the proposed setup in Fig. 3.26, as well. Whereas, during the experiments for the SBS applications there were different problems. Therefore, suggested solutions and recommendations for the future will be mentioned.
The stimulated Brillouin scattering peak gain profile could be radically enhanced by using a suspended SOI waveguide instead of the silica substrate. Therefore, this will give more degree of freedom to the oscillated SOI and will increase the resultant oscillation displacements due to the optical forces. Hence, the over all SBS gain will increase according to Eq. 3.11. In addition, the multi gain frequency contributions are very attractive for multi-frequency signal amplification via the SBS non-linear effect. Therefore, the signal that need to be amplified could be tuned and the appropriate SBS amplification frequency chosen. Additionally, if the SOI is cooled to a specific low temperature a giant increase in the SBS gain could take place. Since the phonon losses will be reduced at low temperatures, the gain could be enhanced 10-100 times [18]. In order to reduce the two-photon absorption non-linear effect and therefore allow more useful pump power to increase the SBS gain, there are three main suggestions. First: using a pulsed pump power laser, and therefore provide high power in a short time. Second: increase the waveguide length to increase the interaction length. Third: sweeping out the free carriers from the optical mode using a transverse p-n junction structure.

For the first stimulated Brillouin scattering optical sharp filter application, a software technique (dip search) was used to detect the amplified spectral line and lock the pump wavelength for the SBS process via adapting the laser current controller. This technique suffered from the measuring delay time, as well as the frequency comb and the pump laser diode had fast drifts where the algorithm lost the locking state. An electrical digital circuit could be utilized in the future to achieve the locking task. Hence, the instantaneous electrical processing for the amplified spectral line detection and therefore the very fast reaction and adapting the pump wavelength will reduce the time delay to a minimum. Additionally, for the fine tuning and stabilization of the extracted spectral line the tuneable optical filter bandwidth was limited as well as there was about 20 dB power loss. In order to get rid of the these limitations, a single sideband modulation or an acousto optic modulator can be utilized. Thus, the tunable optical filter could be omitted. Hence, the fine tuneability could be increased or decreased depending on the single sideband scheme that will be used. Additionally, the software technique that was used to achieve the stabilization could be changed with the electronic digital circuit that

was used with the stabilization of the milli-meter wave or a frequency counter with a very high resolution and fast data acquisition time could be used. Therefore, a drift of 1 Hz could be achieved over several hours.

For the second stimulated Brillouin scattering optical sharp filter application, the same technique that is mentioned above could be utilized to enhance the locking task. For the software stabilization approach, as mentioned earlier, a high quality frequency counter can be used to get higher stabilization for the repetition rate drift. Additionally, for the stabilization one can combine both the software and the electric circuit approaches in one high quality electronic circuit to achieve both the low phase noise and the high milli-meter stabilization. For the future, a high quality electronic circuit with lower electrical noise components could be applied to get rid of the high frequency noise that had been impaired the experiment.

Generally, in the near future the applications of the stimulated Brillouin scattering will show a great attraction. Recently, there has been shown a great interest in SBS applications based on SOI, investigating the role of the spatial evolution of the acoustic field in SBS effect in short high-gain structures (SOI), for instance [120]. Additionally, investigations and demonstrations like: chalcogenide glass waveguide [119, 120, 121], tunable narrow band microwave photonic filter achieved by SBS based silicon nanowire [122] and realization of the SBS based tunable microwave photonic notch filter in a photonic chip [123], show a great attraction towards the integration of the SBS system on a chip. Finally, the investigated SBS effect in the proposed SOI structures and cases should be experimentally demonstrated and proved, as well as the applications based on SBS should be integrated within the SOI technology.

References

[1] R. W. Boyd "Nonlinear Optics," Elsevier Inc., 2008.

[2] G. P. Agrawal "Fiber-Optic Communication Systems," John Wiley and Sons, Inc., 2002.

[3] R. S. Krishnan "On the Depolarisation of Tyndall Scattering in Colloids," Proceedings of the Indian Academy of Sciences - Section A, Vol. 1, No. 10 , pp 717-722, 2000.

[4] B. E. A. Saleh, and M. C. Teich "Fundamentals of Photonics," John Wiley and Sons, Inc., 1991.

[5] J. C. Stover "Optical Scattering: Measurement and Analysis," Spie Press Book, 1995.

[6] I. Kaminow, and T. Li "Optical Fiber Telecommunications IV-A: Components," Elsevier Science, 2002.

[7] T. Schneider "Nonlinear optics in Telecommunications," Springer, 2004.

[8] R. H. Stolen, E. P. Ippen, and A. R. Tynes "Raman Oscillation in Glass Optical Waveguide," Appl. Phys. Lett., Vol. 20, No. 2, pp. 62-64, 1972.

[9] A. Ishimaru "Wave Propagation and Scattering in Random Media," Academic Press, 1978.

[10] L. Brillouin "Wave Propagation and Group Velocity," Academic Press, 1960.

[11] W. Kaiser, and M. Maier "Stimulated Rayleigh, Brillouin and Raman spectroscopy," *in Laser Handbook*, Eds.. F. T. Arecchi and E. O. Schulz, Vol 2, pp. 1077-1150, 1972.

[12] P. Yu, and M. Cardona "Fundamentals of Semiconductors: Physics and Materials Properties," Springer Science and Business Media, 2010.

[13] R. D. Mountain "Spectral Distribution of Scattered Light in a Simple Fluid," Rev. Mod. Phys., Vol. 38, No. 1, pp. 205-214, 1966.

[14] F. Forghieri, R.W. Tkack, and A. R. Chraplyvy "Fiber Nonlinearities and Their Impact on Transmission Systems," Academic Press, 1997.

[15] R. G. Smith "Optical power handling capacity of low loss optical fibers as determined by stimulated Raman and Brillouin scattering," Appl. Opt., Vol. 11, No. 11, pp. 2489-2494, 1972.

[16] H. Al-Taiy, and T. Schneider "Drastically SBS Gain Enhancement in Silicon-on-Insulator based Nano-Waveguides," Photonic Networks 14, ITG Symposium Proceedings, Vol. 241, pp. 182-188, 2013.

[17] J. Leuthold, C. Koos, and W. Freude "Nonlinear Silicon Photonics," Nat. Photon., Vol. 4, No. 8, pp. 535-544, 2010.

[18] P. T. Rakich, C. Reinke, R. Camacho, P. Davids, and Z. Wang "Giant Enhancement of Stimulated Brillouin Scattering in the Subwavelength Limit," Phys. Rev. X 2, Vol. 2, No. 1, pp. 11008-11023, 2012.

[19] G. K. Celler and, S. Cristoloveanu "Frontiers of silicon-on-insulator," Appl. Phys., Vol. 93, No. 9, pp. 4955-4978, 2003.

[20] K. Hotate, and H. Zuyuan "Synthesis of Optical-Coherence Function and Its Applications in Distributed and Multiplexed Optical Sensing," J. Lightw. Technol., Vol. 24, No. 7, pp. 2541-2557, 2006.

[21] K. Shimizu, T. Horiguchi, Y. Koyamada, and T. Kurashima "Coherent Self-Heterodyne Brillouin OTDR for Measurement of Brillouin Frequency Shift Distribution in Optical Fibers," J. Lightw. Tech., Vol. 12, No. 5, pp. 730-736, 1994.

[22] T. Horiguchi, T. Kurashima, and M. Tateda "A Technique to Measure Distributed Strain in Optical Fiber," IEEE Phot. Tech. Lett., Vol. 2, No. 5, pp. 352-354, 1990.

[23] L. Wang, B. Zhou, C. Shu, and S. He "Stimulated Brillouin Scattering Slow-Light-Based Fiber-Optic Temperature Sensor," Opt. Lett. Vol, 36, No.3, pp. 427-429, 2011.

[24] H. Al-Taiy, N. Wenzel, S. Preußler, J. Klinger, and T. Schneider "Ultra-Narrow Linewidth, Stable and Tunable Laser Source for Optical Communication Systems and Spectroscopy," Opt. Lett., Vol. 39, No. 20, pp. 5826-5829, 2014.

[25] H. Al-Taiy, S. Preußler, S. Bruckner, J Schoebel, and T. Schneider "Generation of Highly Stable Millimeter Waves With Low Phase Noise and Narrow Linewidth," IEEE Phot. Tech. Lett., Vol. 27, No. 15, pp. 1613-1616, 2015.

[26] A. Wise, M. Tur and, A. Zadok "Sharp Tunable Optical Filters Based on the Polarization Attributes of Stimulated Brillouin Scattering," Opt. Express, Vol. 19, No. 22, pp. 21945-21955, 2011.

[27] E. L. Feinberg "The forefather (about Leonid Isaakovich Mandelstam)," Physics-Uspekhi, Vol. 45, No. 1, pp. 81-100, 2002.

[28] L. Brillouin "Diffusion de la Lumière et des Rayonnes X par un Corps Transparent Homogène; Influence de L'agitation Thermique," Ann. phys. (Paris), Vol. 17, pp. 88-122, 1922.

[29] W. William "Absorption of Electromagnetic Radiation," AccessScience, McGraw-Hill, 2013.

[30] J. C. Maxwell "A Dynamical Theory of the Electromagnetic Field," Phil. Trans. R. Soc. Lond., Vol. 155, pp. 459-512, 1865.

[31] K. Zhang, and D. Li "Electromagnetic Theory for Microwaves and Optoelectronics," Springer, 2008.

[32] Wave Propagation Standards Committee of the Antennas and Propagation Society, "IEEE Standard Definitions of Terms for Radio Wave Propagation," IEEE Std. 211-1997 USA, pp. 1-39, 1998.

[33] Y. R. Shen "The Principles of Nonlinear Optics," John Wiley and Sons, 1984.

[34] K. A. Tsokos "Physics for the IB Diploma Full Colour," Cambridge University Press, 2010.

[35] A. Yariv "Quantum Electronics," John Wiley and Sons, 1989.

[36] J. F. Nye "Physical Properties of Crystals: Their Representation by Tensors and Matrices," Oxford University Press, 1985.

[37] J. M. Ide "The Velocity of Sound in Rocks and Glasses as a Function of Temperature," The Journal of Geology, Vol. 45, No. 7, pp. 689-716, 1937.

[38] M. J. Damzen "Stimulated Brillouin Scattering Fundamentals and Applications," IOP Publishing, 2003.

[39] M. Niklès, L. Thévenaz, and P. A. Robert "Brillouin Gain Spectrum Characterization in Single-Mode Optical Fibers," Jour. of Light. Tech., Vol. 15, No. 10, pp. 1842-1851, 1997.

[40] A. Zheltikov, A. L'Huillier, and F. Krausz "Springer Handbook of Lasers and Optics," Springer Berlin Heidelberg, 2012.

[41] S. Preußler, K. Jamshidi, A. Wiatrek, R. Henker, CA. Bunge, and T. Schneider "Quasi-Light-Storage Based on Time-Frequency Coherence," Opt. Exp., Vol. 17, No. 18, pp. 15790-15798, 2009.

[42] A. Coillet, R. Henriet, K. P. Huy, M. Jacquot, L. Furfaro, I. Balakireva, L. Larger, and Y. K. Chembo "Microwave Photonics Systems Based on Whispering-gallery-mode Resonators," Jour. Vis. Exp. Vol. 78, No. pp 50423, 2013.

[43] A. Marshall, and S. Natarajan "SOI Design: Analog, Memory and Digital Techniques," Springer, 2002.

[44] J.-P. Colinge "Silicon-on-Insulator Technology: Materials to VLSI," Springer, 2004.

[45] N. W. Ashcroft, and N. D. Mermin "Solid State Physics," Harcourt: New York, 1976.

[46] A. Feldman "Relations Between Electrostriction and The Stress-Optical Effect," Phys. Rev. B 11, No. 12, pp. 5112-5114, 1975.

[47] W. Qiu, P. T. Rakich, H. Shin, H. Dong, M. Soljačić, and, Z. Wang "Stimulated Brillouin Scattering in Nanoscale Silicon Step-Index Waveguides: a General Framework of Selection Rules and Calculating SBS Gain," Opt. Exp., Vol. 21, No. 25, pp. 31402-31419, 2013.

[48] A. J. Moses "Refractive Index of Optical Materials in The Infrared Region," Hughes Aircraft Co., Culver City, California, DS-166, 1970.

[49] D. Royer, and E. Dieulesaint "Elastic Waves in Solids 1: Free and Guided Propagation," Springer, 1996.

[50] C. Koos, L. Jacome, C. Poulton, J. Leuthold, and W. Freude "Nonlinear Silicon-on-Insulator Waveguides for All-Optical Signal Processing," Opt. Exp, Vol. 15, No. 10, pp. 5976-5990, 2005.

[51] V. Raghunathan, D. Dimitropoulos, R. Claps, and B. Jalali "Raman Induced Wavelength Conversion in Scaled Silicon Waveguides," IEICE Electronics Exp., Vol. 1, No. 11, pp. 298-304, 2004.

[52] R. Claps, D. Dimitropoulos, V. Raghunathan, Y. Han, and B. Jalali "Observation of Stimulated Raman Amplification in Silicon Waveguides," Opt. Exp., Vol. 11, No. 15, pp. 1731-1739, 2003.

[53] S. Mahdi "Raman Effect in Silicon-On-Insulator Nanowire Waveguides," Mensch and Buch, 2013.

[54] COMSOL AB, COMSOL 4.3b: Structural Mechanics Module User's Guide, COMSOL AB, 2013.

[55] S. A. Chandorkar, R.N. Candler, A. Duwel, R. Melamud, M. Agarwal, K. E. Goodson, and T. Kenny "Multimode Thermo Elastic Dissipation," Jour. Appl. Phys., Vol 105, No. 4, pp. 043505-043518, 2009.

[56] W. Qiu, P. Rakich, M. Soljacic, and Z. Wang "Stimulated Brillouin Scattering in Slow Light Waveguides," arXiv 1210.0738, 2012.

[57] L. S. Hounsome, R. Jones, M. J. Shaw, and P. R. Briddon "Photoelastic Constants in Diamond and Silicon," Phys. Status Solidi (A), Vol. 203, No. 12, pp. 3088-3093, 2006.

[58] K. H. Panofsky, and M. Phillips "Classical Electricity and Magnetism," Addison Wesley, 1962.

[59] H. Shin, W, Qiu, R. Jarecki, J. A. Cox, R. H. Olsson, A. Starbuck, Z. Wang, and P. T. Rakich "Tailorable Stimulated Brillouin Scattering in Nanoscale Silicon Waveguides," Nat. Commun., Vol 4, No. 1944, pp. 1-10, 2013.

[60] E. Ip, and J. M. Kahn "Feedforward Carrier Recovery for Coherent Optical Communications," Jour. of Lightwave Technol., Vol. 25, No. 9, pp. 2675-2692, 2007.

[61] H. Al-Taiy, N. Wenzel, S. Preußler, J. Klinger, and T. Schneider "Ultra-Narrow Line-width, Stable and Widely Tuneable Laser Source for Coherent Optical Communication Systems," (ECOC), European Conference, DOI: 10.13140/2.1.3913.3765, 2014.

[62] A. Cygan, D. Lisak, P. Morzyński, M. Bober, M. Zawada, E. Pazderski, and R. C. lo "Cavity Mode-Width Spectroscopy with Widely Tunable Ultra Narrow Laser," Opt. Express, Vol. 21, No. 24, pp. 29744-29754, 2013.

[63] M. Nakazawa, T. Hirooka, M. Yoshida, and K. Kasai "Ultrafast Coherent Optical Transmission," IEEE Jour. of Selected Topics in Quantum Electronics, Vol. 18, No. 1, pp. 363-366, 2012.

[64] T. Wang, G. Wellbrock, and O. Ishida "Next Generation Optical Transport Beyond 100G," IEEE Comm. Mag., Vol. 50, No. 2, pp. s10-s11, 2012.

[65] R. Todt, T. Jacke, R. Meyer, J. Adler, R. Laroy, G. Morthier, and M.-C. Amann "Sampled Grating Tunable Twinguide Laser Diodes with Over 40-nm Electronic Tuning Range," IEEE Phot. Technol. Lett., Vol. 17, No. 12, pp. 2514-2516, 2005.

[66] D. Pan, C. Ke, S. Fu, Y. Liu, D. Liu, and A. E. Willner "All-Optical Spectral Linewidth Reduction of Lasers for Coherent Optical Communication," Opt. Lett., Vol. 38, No. 24, pp. 5220-5223, 2013.

[67] L. Rodrguez-Cobo, M. A. Quintela, S. Rota-Rodrigo, M. Lpez-Amo, and J. M. Lpez-Higuera "Single- Longitudinal Mode Laser Structure Based on a Very Narrow Filtering Technique," Opt. Express, Vol. 21, No. 8, pp. 10289-10294, 2013.

[68] F. Aflatouni, and H. Hashemi "Light Source Independent Linewidth Reduction of Lasers," Optical Fiber Communication Conference OSA Technical Digest (Optical Society of America), doi:10.1364/OFC.2012.OW1G.6, 2012.

[69] S. Preußler, and T. Schneider "Bandwidth reduction in a multi-stage Brillouin system," Opt. Lett., Vol. 37, No. 19, pp. 4122-4124, 2012.

[70] J. C. Yong, L. Thvenaz, and B. Kim "Brillouin Fiber Laser Pumped by a DFB Laser Diode," Jour. Lightwave Technol., Vol. 21, No. 2, pp. 546-554, 2003.

[71] T. R. Schibli, I. Hartl, D. C. Yost, M. J. Martin, A. Marcinkevic caronius, M. E. Fermann, and J. Ye "Optical Frequency Comb with Submillihertz Linewidth and more than 10 W Average Power," Nat. Photon., Vol. 2, No. 6, pp. 355-359, 2008.

[72] A. Bartels, C. W. Oates, L. Hollberg, and S. A. Diddams "Stabilization of Femtosecond Laser Frequency Combs with Subhertz Residual Linewidths," Opt. Lett., Vol. 29, No. 10, pp. 1081-1083, 2004.

[73] M. Gagné, S. Loranger, J. Lapointe, and R. Kashyap "Fabrication of High Quality, Ultra-Long Fiber Bragg Gratings: up to 2 Million Periods in Phase," Opt. Express, Vol. 22, No. 1, pp. 387-398, 2014.

[74] M. F. Karim, A. Q. Liu, L. C. Ong, and Y. -X. Guo "Micromachined based narrow band FabryPerot tunable bandpass filter," IET Microw., Antennas and Propag., Vol. 6, No. 5, pp. 562-568, 2012.

[75] J. N. Eckstein, A. I. Ferguson, and T. W. Hänsch "High-Resolution Two-Photon Spectroscopy with Picosecond Light Pulses," Phys. Rev. Lett., Vol. 40, No. 13, pp. 847-850, 1978.

[76] J. Ye and S. T. Cundiff "Femtosecond Optical Frequency Comb: Principle, Operation and Applications," Springer, 2004.

[77] J. Ye, H. Schnatz, and L. W. Hollberg "Optical Frequency Combs: From Frequency Metrology to Optical Phase Control," IEEE J. Sel. Top. Quantum Electron., Vol. 9, No. 4, pp. 1041-1058, 2003.

[78] L. Hollberg, S. Diddams, C. Oates, A. Curtis, and J. Bergquist "Atomic Clocks of The Future: Using The Ultrafast and Ultrastable," International Conference on Ultrafast Phenomena 13, OSA Technical Digest Series, paper MA1, pp. 170-174, 2002.

[79] Y. Bai, D. Ren, W. Zhao, Y. Qu, L. Qian, and Z. Chen "Heterodyne Doppler Velocity Measurement of Moving Targets by Mode-Locked Pulse Laser," Opt. Exp., Vol 20, No. 2, pp. 764-768, 2011.

[80] S. T. Cundiff and A. M. Weiner "Optical Arbitrary Waveform Generation," Nat. Photon., Vol. 4, No. 11, pp. 760-766, 2010.

[81] T. Horiguchi, M. Tateda, M. Shibata, and Y. Azuma "Brillouin Gain Variation due to a Polarization-State Change of the Pump or Stokes Field in Standard Single Mode Fibers," Opt. Lett., Vol. 14, No. 6, pp. 329-331, 1989.

[82] G. N. Ramachandran, and S. Ramaseshan "Crystal Optics, Part A: Polarisation of Light," Springer-Verlag, Vol. XXV/I, pp. 1-54, 1961.

[83] M. O. van Deventer, and A, J. Boot "Polarization Properties of Stimulated Brillouin Scattering in Single-Mode Fibers," Light. Technol, Vol. 12, No. 4, pp. 585-590, 1994.

[84] M. O. van Deventer "Polarization properties of Rayleigh Backscattering in Single-Mode Fibers," Light. Technol., Vol. 11, No. 12, pp. 1985-899, 1993.

[85] A. Zadok, E. Zilka, A. Eyal, L. Thévenaz, and M. Tur "Vector Analysis of Stimulated Brillouin Scattering Amplification in Standard Single-Mode Fibers," Opt. Exp., Vol. 16, No. 26, pp. 21692-21707, 2008.

[86] D. Guyomarc'h, G. Hagel, C. Zumsteg, and M. Knoop "Some Aspects of Simulation and Realization of an Optical Reference Cavity," Phys. Rev. A, Vol. 80, No. 6, pp. 63802-63806, 2009.

[87] J. Subías, C. Heras, J. Pelayo, and F. Villuendas "All in Fiber Optical Frequency Metrology by Selective Brillouin Amplification of Single Peak in an Optical Comb," Opt. Exp., Vol. 17, No. 8, pp. 6753–6758, 2009.

[88] E. Ip, A. P. Lau, D. J. Barros, and J. M. Kahn "Coherent Detection in Optical Fiber Systems," Opt. Exp., Vol. 16, No. 2, pp. 753–791, 2008.

[89] T. Pfau, S. Hoffmann, O. Adamczyk, R. Peveling, V. Herath, M. Porrmann, and R. Noé "Coherent Optical Communication: Towards Realtime Systems at 40 Gbit/s and Beyond," Opt. Exp., Vol. 16, No. 2, pp. 866–872, 2008.

[90] D. Derickson "Fiber Optic Test and Measurement," Prentice Hall PTR, 1998.

[91] H. Tsuchida "Simple Technique for Improving the Resolution of the Delayed Self-Heterodyne Method," Opt. Lett. Vol. 15, No. 11, pp. 640-642, 1990.

[92] J. W. Nicholson, M. F. Yan, P. Wisk, J. Fleming, F. DiMarcello, E. Monberg, A. Yablon, C. Jrgensen, and T. Veng "All-fiber, Octave-Spanning Supercontinuum," Opt. Lett., Vol. 28, No. 8, pp. 643-645, 2003.

[93] S. Preußler, A. Wiatrek, K. Jamshidi, and T. Schneider "Brillouin Scattering Gain Bandwidth Reduction down to 3.4 MHz," Opt. Exp., Vol. 19, No. 9, pp. 8565-8570, 2011.

[94] A. Wiatrek, S. Preußler, K. Jamshidi, and T. Schneider "Frequency Domain Aperture for the Gain Bandwidth Reduction of Stimulated Brillouin Scattering," Opt. Lett., Vol. 37, No. 5, pp. 930-932, 2012.

[95] S. Preußler, A. Wiatrek, K. Jamshidi, and T. Schneider "Ultrahigh Resolution Spectroscopy Based on the Bandwidth Reduction of Stimulated Brillouin Scattering," IEEE Phot. Technol. Lett., Vol. 23, No. 16, pp. 1118-1120, 2011.

[96] H. Al-Taiy, S. Preußler, S. Bruckner, J. Schoebel, and T. Schneider "Generation of Highly Stable Millimeter Waves with Low Phase Noise and Narrow Linewidth," IEEE Phot. Soci. Conf. Reston, Virginia USA, pp. 98-101, 2015.

[97] R. J. Jones, K. Holman, and J. Ye "Femtosecond Laser Stabilization: Time and Frequency Domain Applications," IEEE LEOS Newsletter, Vol. 17, No. 5, pp. 43-44, 2003.

[98] K. C. Huang and W. Zhaocheng "Millimeter Wave Communication Systems," John Wiley and Sons, 2011.

[99] G. C. Valley "Photonic Analog-to-Digital Converters," Opt. Exp., Vol. 15, No. 5, pp. 1955-1982, 2007.

[100] G. Santarelli, C. Audoin, A. Makdissi, P. Laurent, G. J. Dick, and A. Clairon "Frequency Stability Degradation of an Oscillator Slaved to a Periodically Interrogated Atomic Resonator," IEEE Trans. Ultrason. Ferroelectr. Freq. Control, 45, 887, 1998.

[101] T. Schneider, A. Wiatrek, S. Preußler, M. Grigat, and R. Braun "Link Budget Analysis for Terahertz Fixed Wireless Links," IEEE Trans. Terahertz Sci. Technol., Vol. 2, No. 2, pp. 250-256, 2012.

[102] M. Marcus and B. Pattan "Millimeter Wave Propagation; Spectrum Management Implications," Microwave Magazine IEEE, Vol. 6, No. 2, pp. 54-62, 2005.

[103] J. R. Demers, T. M. Goyette, K. B. Ferrio, H. O. Everitt, B. D. Guenther, and F. C. De Lucia "Spectral purity and Sources of Noise in Femtosecond Demodulation Terahertz Sources Driven by Ti : Sapphire mode-locked Lasers," IEEE Jour. Quant. Electron., Vol. 37, No. 4, pp. 595-605, 2001.

[104] T. Uehara, K. Tsuji, K. Hagiwara, and N. Onodera "Optical Beat-Note Frequency Stabilization Between Two Lasers Using a Radio Frequency Interferometer in the Gigahertz Frequency Band," Opt. Eng. Vol. 52, No. 12, pp. 4109-4115, 2014.

[105] N. Kim, J. Shin, E. Sim, C. W. Lee, D-S. Yee, M. Y. Jeon, Y. Jang, and K. H. Park "Monolithic Dual-Mode Distributed Feedback Semiconductor Laser for Tunable Continuous-wave Terahertz Generation," Opt. Exp., Vol. 17, No. 16, pp. 13851-13859, 2009.

[106] Y. Doi, S. Fukushima, T. Ohno, and K. Yoshino "Frequency Stabilization of Millimeter-Wave Subcarrier Using Laser Heterodyne Source and Optical Delay Line" Phot. Tech. Lett. Vol. 13, No. 9, pp. 1002-1004, Sep. 2001.

[107] A. Hirata, H. Togo, N. Shimizu, H. Takahashi, K. Okamoto, and T. Nagatsuma "Low-Phase Noise Photonic Millimeter-Wave Generator Using an AWG Integrated with a 3-dB Combiner," IEICE Trans. Electron. E88-C, pp. 1458-1464, 2005.

[108] S. Preußler, N. Wenzel, R. -P. Braun, N. Owschimikow, C. Vogel, A. Deninger, A. Zadok, U. Woggon, and T. Schneider "Generation of Ultranarrow, Stable and Tunable Millimeter- and Terahertz- Waves with Very Low Phase Noise," Opt. Exp., Vol. 21, No. 20, pp. 23950-23962, 2013.

[109] J. Rauschenberger, T. M. Fortier, D. J. Jones, J. Ye, and S. T. Cundiff "Control of the Frequency Comb from a Mode-Locked Erbium-Doped Fiber Laser," Opt. Exp., Vol. 10, No. 24, pp. 1404-1410, 2002.

[110] S. Rieger, T. Hellwig, T. Walbaum, and C. Fallnich "Optical Repetition Rate Stabilization of a Mode-Locked All-Fiber Laser," Opt. Exp., Vol. 21, No. 3, pp. 4889-4895, 2013.

[111] N. Haverkamp, H. Hundertmark, C. Fallnich, and H. R. Telle "Frequency Stabilization of Mode-Locked Erbium Fiber Lasers Using Pump Power Control," Appl. Phys. B, Vol. 78, No. 3-4, pp. 321-324, 2004.

[112] T. H. Lee and A. Hajimiri "Oscillator Phase Noise: A Tutorial," IEEE Jour. of Solid-State Circuits, Vol. 35, No. 3, pp. 326-336, 2000.

[113] A. Demir, A. Mehrotra, and J. Roychowdhury "Phase Noise in Oscillators: a Unifying Theory and Numerical Methods for Characterization," IEEE Trans. on Circuits and Systems I: Fundamental Theory and Applications, Vol. 47, No. 5, pp. 655-674, 2000.

[114] S. Fukushima, C. F. C. Silva, Y. Muramoto, and A. J. Seeds "Optoelectronic Millimeter-Wave Synthesis Using an Optical Frequency Comb Generator, Optically Injection Locked Lasers, and a Unitraveling-Carrier Photodiode," Jour. of Light. Tech., Vol. 21, No. 12, pp. 3043-3051, 2003.

[115] N5181A Keysight-Agilent Radio Frequency Generator Data Sheet.

[116] S. Preußler, H. Al-Taiy, and T. Schneider "Optical Spectrum Analysis with kHz Resolution Based on Polarization Pulling and Local Oscillator Assisted Brillouin Scattering," ECOC European Conference on, Valencia, pp. 1-3, 2015.

[117] E. D. Black "An Introduction to Pound-Drever-Hall Laser Frequency Stabilization," Am. J. Phys., Vol. 69, No. 1, pp. 79-87, 2001.

[118] S. Preußler, H. Al-Taiy, and T. Schneider "Generation and Stabilization of THz-Waves with Extraordinary Low Line Width and Phase Noise," CLEO San Jose, CA, pp. 1-2, 2015.

[119] S. R. Mirnaziry, C. Wolff, M. J. Steel, B. J. Eggleton, and C. G. Poulton "Stimulated Brillouin Scattering in Silicon/Chalcogenide Slot Waveguides," Opt. Exp., Vol. 24, No. 5, pp. 4786-4800 , 2016.

[120] C. Wolff, M. J. Steel, B. J. Eggleton, and C. G. Poulton "Acoustic Build-up in on-Chip Stimulated Brillouin Scattering," Scientific Reports, Vol. 5, SP. 13656, 2015.

[121] B. J. Eggleton, C. G. Poulton, and R. Pant "Inducing and Harnessing Stimulated Brillouin Scattering in Photonic Integrated Circuits," Adv. in Opt. and Phot., Vol. 5, No. 4, pp. 536-587, 2013.

[122] A. C. Bedoya, B. Morrison, M. Pagani, D. Marpaung, and B. J. Eggleton "Tunable Narrowband Microwave Photonic Filter Created by Stimulated Brillouin Scattering from a Silicon Nanowire," Opt. Lett., Vol. 40, No. 17, pp. 4154-4157, 2015.

[123] B. Morrisona, D. Marpaunga, R. Panta, E. Lia, D. Y. Choib, S. Maddenb, B. L. Daviesb, and B. J. Eggletona "Tunable Microwave Photonic Notch Filter Using on-Chip Stimulated Brillouin Scattering," Opt. Comm., Vol. 313, pp. 85-89, 2014.

List of Publications

1. **H. Al-Taiy** and T. Schneider "Utilization of Polarization Pulling Assisted Stimulated Brillouin Scattering for Frequency Comb Applications," EMN Beijing Meeting, Invited Talk, 2016.

2. **H. Al-Taiy**, S. Preußler, S. Bruckner, J Schoebel and T. Schneider "Generation of Highly Stable Millimeter Waves With Low Phase Noise and Narrow Linewidth", IEEE Phot. Tech. Lett., Vol. 27, No. 15, pp. 1613-1616, 2015.

3. **H. Al-Taiy**, S. Preußler, S. Bruckner, J. Schoebel, and T. Schneider "Generation of Highly Stable Millimeter Waves with Low Phase Noise and Narrow Linewidth," IEEE Phot. Soci. Conf. Reston, Virginia USA, pp. 98-101, 2015.

4. S. Preußler, **H. Al-Taiy**, and T. Schneider "Generation and Stabilization of THz-Waves with Extraordinary Low Line Width and Phase Noise," CLEO San Jose, CA, pp. 1-2, 2015.

5. S. Preußler, **H. Al-Taiy**, and T Schneider "Optical Spectrum Analysis with kHz Resolution Based on Polarization Pulling and Local Oscillator Assisted Brillouin Scattering," Optical Communication (ECOC), European Conference, Valencia, DOI: 10.1109 / 3.1.7341758, 2015.

6. **H. Al-Taiy** S. Preußler, and T. Schneider "Extra-Narrow Linewidth, Stable and Widely Tunable Extracted Single Laser Line," DPG conference in Heidelberg, Quantum Optics and Photonics, Division Fachverband Quantenoptik und Photonik (Q), No. Q 67/2015, pp. 75-75, 2015.

7. **H. Al-Taiy**, N. Wenzel, S. Preußler, J. Klinger and T. Schneider "Ultra-Narrow Line-Width, Stable and Widely Tuneable Laser Source for Coherent Optical Communication Systems", (ECOC), European Conference, DOI: 10.13140/2.1.3913.3765, 2014.

8. **H. Al-Taiy**, N. Wenzel, S. Preußler, J. Klinger and T. Schneider "Ultra-Narrow Linewidth, Stable and Tunable Laser Source for Optical Communication Systems and Spectroscopy", Opt. Lett., Vol. 39, No. 20, pp. 5826-5829, 2014.

9. **H. Al-Taiy** and T. Schneider "Drastically SBS Gain Enhancement in Silicon-on-Insulator based Nano-Waveguides", Photonic Networks 14, ITG Symposium Proceedings, Vol. 241, pp. 182-188, 2013.

10. **H. Al-Taiy** "Proposed Photonic Integrated Circuit For Photonic Networks," IEEE Eng. and Tech. Jour., Vol. 28, No. 8, pp. 1-14, 2010.

11. **H. Al-Taiy** and R. S. Fyath "Analysis and Simulation of All-Optical Router for TDM-Based Optical Networks Using: NOLM," IEEE Eng. and Tech. Jour., Vol. 27, No. 8, pp. 1-13, 2008.

Index